Naval Research Laboratory
Washington, DC 20375-5320

NRL/MR/5650--03-8679

High-Performance Photonic Analog-to-Digital Converter and Low-Noise Mode-Locked Fiber Lasers

MARC CURRIE

Photonics Technology Branch
Optical Sciences Division

May 26, 2003

REPORT DOCUMENTATION PAGE

Form Approved
OMB No. 0704-0188

1. REPORT DATE *(DD-MM-YYYY)* May 26, 2003	**2. REPORT TYPE** Final report	**3. DATES COVERED** *(From - To)*

4. TITLE AND SUBTITLE High-Performance Photonic Analog-to-Digital Converter and Low-Noise Mode-Locked Fiber Lasers	**5a. CONTRACT NUMBER** **5b. GRANT NUMBER** **5c. PROGRAM ELEMENT NUMBER**
6. AUTHOR(S) Marc Currie	**5d. PROJECT NUMBER** **5e. TASK NUMBER** **5f. WORK UNIT NUMBER**
7. PERFORMING ORGANIZATION NAME(S) AND ADDRESS(ES) Naval Research Laboratory 4555 Overlook Avenue, SW Washington, DC 20375-5320	**8. PERFORMING ORGANIZATION REPORT NUMBER** NRL/MR/5650--03-8679
9. SPONSORING / MONITORING AGENCY NAME(S) AND ADDRESS(ES) Defense Advanced Research Projects Agency 3701 North Fairfax Drive Arlington, VA 22203-1714	**10. SPONSOR / MONITOR'S ACRONYM(S)** **11. SPONSOR / MONITOR'S REPORT NUMBER(S)**

12. DISTRIBUTION / AVAILABILITY STATEMENT

Approved for public release; distribution is unlimited.

13. SUPPLEMENTARY NOTES

DARPA Technical Point-of-Contact: Dr. James Murphy

14. ABSTRACT

This project demonstrates three photonic analog-digital converters (ADCs) for high-speed, real-time digitization of microwave signals. The methods consist of a highly parallel photonic ADC, a time-division multiplexed system based on electro-optical Sagnac interferometry, and an all-optical quantizer based upon distributed phase modulation. The core of many photonic ADC designs relies upon a low-noise, actively mode-locked fiber laser that has been developed at NRL. Photonic sampling of microwave signals is investigated especially concerning development of a low-noise optical clock. Optimization and system post-processing is simulated and compared with experimental data. Finally, the low-noise optical clock was used in a four-way collaborative research effort where NRL excited and characterized high-speed, high-current photoconductive switches.

15. SUBJECT TERMS

Analog-to-digital converter; Optical clocks; Mode-locked fiber laser

16. SECURITY CLASSIFICATION OF:			**17. LIMITATION OF ABSTRACT**	**18. NUMBER OF PAGES**	**19a. NAME OF RESPONSIBLE PERSON** Marc Currie
a. REPORT Unclassified	**b. ABSTRACT** Unclassified	**c. THIS PAGE** Unclassified	UL	86	**19b. TELEPHONE NUMBER** *(include area code)* (202) 404-4201

Standard Form 298 (Rev. 8-98)
Prescribed by ANSI Std. Z39.18

DARPA PACT Final Report

TABLE OF CONTENTS

I. Technical Objective
  a. Highly-Parallel, Photonic Analog-Digital Converters
    i. System Performance
    ii. Low Noise Optical Clock
    iii. Optimization and post-processing
  b. High-Energy Testing of Optoelectronic Switches
  c. Optical Quantization via Distributed Phase Modulation
  d. Electro-optic Sagnac interferometer based TDM ADC
II. Importance of Photonic ADCs
III. Technical Approach
IV. Technical Accomplishments
  a. Low-noise Laser development
  b. Photonic ADC
  c. Peer Reviewed Publications
V. Low Noise optical clock
  a. Sigma laser
  b. Multi-wavelength Sigma Laser
  c. Characterization of laser pulses via FROG
VI. Northrop-Grumman optoelectronic switch characterization
VII. Highly parallel photonic analog-digital converter
  a. Clock independent design
  b. 10-GSPS, 8-channel, 7-bit converter
  c. 2.5-GSPS, 2-channel, 5-bit converter
  d. 30-GSPS, 3-channel, ~2-bit converter
VIII. Optimization and post-processing
  a. Digital Linearization
  b. Feed-Forward Noise Eater: Suppression of Supermode Oscillations
  c. Non-uniform Optical sampling of microwave signals
IX. Optical Quantization via Distributed Phase Modulation
X. 100-GSPS TDM ADC via Electro-optic Sagnac interferometry

DARPA Photonic A/D Converter Technology (PACT) Program

Naval Research Laboratory (NRL) Team

Photonic A/D Converter Technology:

Marc Currie
Nicholas Condon
Thomas Clark
Jin Kang
Michael Frankel
Ron Esman

Optical Clock Development:

Marc Currie
Janet Lou
Fredrik Fatemi
Thomas Clark
Tom Carruthers
Irl Duling

A. Highly-Parallel, Photonic Analog-Digital Converters

i. System Performance

This project demonstrates highly-parallel, photonic analog-digital converters (ADCs) for high-speed sampling and digitization of microwave signals. The method consists of an electro-optic front-end for the photonic sampling of a microwave signal and demultiplexing of this signal, and an electronic back-end for signal digitization and processing. The synchronization of the photonic and electronic subsystems and the precise sampling of the signal are key issues. The core of the entire photonic ADC design relies upon a low-noise, actively mode-locked fiber laser that has been developed at NRL.

NRL has designed and built multiple photonic ADCs using clock rate independent designs in the photonic subsystem achieving three systems. The first system constructed was an eight channel, 10-gigasample-per-second (GSPS) photonic ADC with a measured performance of ~5 effective number of bits (ENOB) resolution (with an ultimate laser noise limit of 7 ENOB) for digitizing a 1.2 GHz input. To optimize this system, a second two-channel system was designed and built and demonstrated digitization of a 0.9-GHz signal with 5 ENOB using a 2.5-GSPS photonic ADC. Finally, upon realizing the future photonic ADCs would be based upon even faster electronic ADCs running at 10-GSPS, a third system was constructed by synchronizing our photonic subsystem with LeCroy Corporation's 10-GSPS electronic converters. This allowed us to realize a 30-GSPS system. When digitizing an 11.4-GHz microwave signal we realized 29.25-dB spur-free dynamic range commensurate with greater than 4.5 ENOB, the limit of the electronic ADC.

ii. Low Noise Optical Clock

The success of these goals is due to our progress in building low-noise optical clocks. The sigma laser is an actively mode-locked single-polarization erbium fiber laser modulated at frequencies from 1-20 GHz that produces ~1-ps pulses. The observed degree of pulse shortening agrees with the predictions of recently developed soliton laser models. The rms amplitude and timing jitter are less than 0.1% and 10 fs, respectively over a 100-Hz to 1-MHz integration range.

The pulses have been compressed using dispersion decreasing fiber (DDF) and self phase modulation to <200-fs generating optical bandwidths of > 9 nm at -3 dB, and 25 nm at -10 dB. Spectral slicing techniques were implemented taking the single laser pulse and generating multiple optical pulses each with distinct wavelengths. Noise processes arising from this temporal and spectral modification were studied.

Following the successes of the sigma laser, a multi-wavelength sigma laser was created providing simultaneous output of four distinct wavelengths at a 10-GHz repetition rate. The laser was capable of producing < 10-ps pulses over a 22-nm optical bandwidth, with demonstration of a variable repetition rate from 1-10 GHz. This removes the need for the temporal and spectral processes in DDF and spectral slicing, thereby improving the system performance while reducing the system complexity.

Manuscript approved 18 April 2003

iii. Optimization and post-processing

System optimization and signal post-processing studies improved the overall system design. Digital algorithms were created to linearize the output signal, allowing optical modulation depths as large as 83% with 27-dB third-order distortion suppression, thereby decreasing design requirements optical power and photodiode performance. In addition, feed-forward optical noise eater systems were created to reduce amplitude fluctuations in the optical pulse train and successfully reduced amplitude noise by >15 dB. Finally, investigation into reducing interleaving spurs was performed by utilizing non-uniform optical sampling of microwave signals. This post-processing method is capable of correcting for established time errors between channels in the ADC. This optimization and post-processing of data reduces errors and maximizes the dynamic range of photonic ADC systems.

B. High-Energy Testing of Optoelectronic Switches

As part of accomplishing the overall objective, NRL participated in a four-way collaborative research effort (CRE) whose members included: Northrop Grumman, Rockwell, the University of Maryland, and the Naval Research Laboratory. As part of the CRE, NRL used an actively mode-locked fiber laser and microwave probe station to analyze the optoelectronic switches and microwave circuitry for the Photonic ADC system led by Northrop Grumman.

To meet these goals, the NRL sigma laser was amplified and frequency doubled to achieve 350-pJ pulses at 777 nm from a 1-GHz Sigma laser. The laser was coupled to the University of Maryland's GaAs metal-semiconductor-metal (MSM) photodiode. The measured electrical signal with a 5-Volt applied bias achieved an electrical pulse with a 17-ps rise time, 60-mS peak conductance, and a 5-mS static offset. The switch was integrated into the Northrop Grumman microwave circuit and re-tested. The integrated switch achieved the 1-GHz repetition rate desired for the NRL portion of the project.

C. Optical Quantization via Distributed Phase Modulation

An optical quantizer and photonic ADC scheme was created by utilizing wavelength division multiplexing in conjunction with optical phase modulation. With its simple pipeline processing technique it produces a digital optical output with each bit on a different wavelength if desired (allowing encoding of the output data as well as creating an optical transmitter for this data). Utilizing the optical system to perform the analog processing removes the electronic ADC common as the final stage in current photonic ADC designs. This increases the performance limit of this photonic ADC to essentially that of the phase modulators, affording much higher speed processing with commercially available products.

A high-speed photonic ADC was constructed with a cw laser and demonstrated optical quantization of 25-GHz microwave signals with 2-bit resolution and 10-GHz microwave signals with 3-bits of resolution. The quantized optical output signal is in the form of a non-return to zero (NRZ) optical data pattern. This data can be left in the optical domain or can be converted to the electrical domain by using high bit-rate optical telecommunication methods.

D. 100-GSPS TDM ADC via Electro-optic Sagnac interferometry

A photonic ADC was built which electro-optically samples high frequency electrical signals and utilizes an electro-optic modulator based time-division demultiplexer allowing parallel electronic digitization at speeds accessible to modern day electronics. The time-division demultiplexing technique makes use of a 1:8 serial-parallel converter with electronic-bias free electro-optic Sagnac interferometers, providing highly stable electronic-bias free operation and the potential for minimal user adjustment in a deployed system. The performance of a 100-GSPS photonic ADC achieved individual channel signal-to-noise ratios that support up to 4 ENOB, with better than 5 effective bits of resolution demonstrated for a lower loss system.

II. Importance of Photonic ADCs

In order to extract information from the microwave and radio frequency (RF) carriers used in current Navy Radar and Electronic Support Measures (ESM) systems, several stages of mixing and filtering provide the downconversion of the signal frequency for digitization by conventional low speed analog-to-digital converters (ADCs). The multi-stage mixing and filtering process can be expensive, limit reliability and instantaneous bandwidth, and increase system size and weight. In addition, each stage introduces RF signal distortion and increases electro-magnetic interference susceptibility.

A high speed, high dynamic range ADC permitting the direct digitization of the RF signals would eliminate the undesirable multiple stages of mixing and filtering while enabling new functionality. The fiber optic remoting inherent in the photonic ADC proposed here would also reduce the outboard antenna components to only the electro-optic modulator. This would reduce the weight and size of each transmit/receiver (TR) module and eliminate the need for bulky microwave and RF cables to each module. The remaining processing and control could be done in an inboard central location away from the TR modules.

Other advantages of this photonic ADC are readily apparent including: wide instantaneous bandwidths (DC – 80 GHz), low antenna front-end prime power, scalability, and the potential for advanced digital processing of signals.

III. Technical Approach

The photonic ADC architecture is based on discrete time domain to wavelength domain mapping utilizing commercially available technology. The proposed system, which was experimentally demonstrated in FY99, is shown in Figure 1. Spectrally broad pulses from a mode-locked laser are sliced by a wavelength division multiplexer (WDM) into *N* wavelength discrete channels. Connected to each channel are a fiber stretcher (FS), variable attenuator (AT), fiber delay loop (DL) and Faraday mirror (FM). The Faraday mirror provides polarization compensation for the non-polarization maintaining components of each channel as well as a second pass through the WDM. The length of each channel's propagation loop is chosen to discretely fill the interpulse period of the original pulse train. The fiber stretcher provides temporal fine-tuning. The variable attenuators allow the compensation of the input pulse spectrum to provide equal optical power in each channel. After amplification, a $LiNbO_3$ electro-optic modulator amplitude modulates the pulse train with the signal to be digitized. After modulation, a second WDM is used to demultiplex the time- and wavelength-interleaved pulse train. The demultiplexed pulse trains are demodulated by photodetectors and digitized in parallel using electronic ADCs. The digitization of each channel occurs at a rate which is N times slower than the photonic ADC sampling rate, thus significantly reducing the requirements on the bandwidth of the back-end electronic components. Subsequent processing of the digitized signals and knowledge of the wavelength-time mapping allows the reconstruction of the original RF signal.

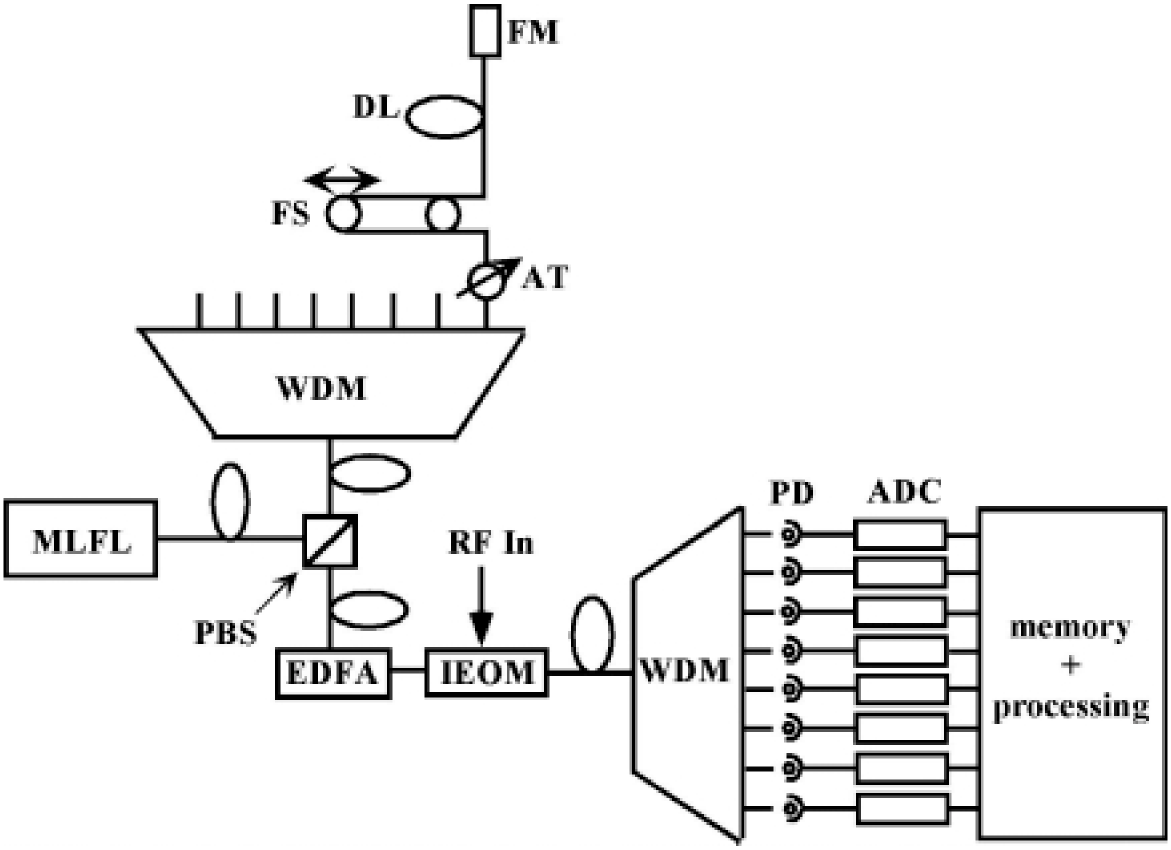

Figure 1—Photonic ADC architecture based on discrete wavelength-time mapping

This system has several potential advantages over conventional all-electronic ADCs.

1. **Fundamental Limit:** The fundamental limitation on the bandwidth, Δf_{ADC}, of the described ADC system is due to RF modulation induced spectral broadening causing cross-talk between adjacent channels and/or loss of modulation information after the demultiplexing channel passband. The system sampling rate for a WDM with N channels and a laser with repetition rate R_{laser} is given by $f_s = R_{laser} N$. Assuming Nyquist sampling, $f_s = 2 \cdot \Delta f_{ADC}$, the constraint on the number of WDM channels and the demultiplexing passband, $\delta\lambda_{ch}$, can be shown to be

$$\left(\frac{\delta\lambda_{ch}}{N}\right)_{WDM} > \frac{\lambda_0^2 R_{laser}}{c},$$

where c is the speed of light in vacuum and λ_0 is the laser wavelength. An additional constraint on the number of WDM channels results from the laser bandwidth where $\Delta\lambda_{laser} > N\delta\lambda_{ch}$. Current commercially available dense WDM technology (200 GHz channel spacing, and up to 32 channels with 1 nm passband) would allow a 1.5μm laser with 50-nm bandwidth and 4 GHz repetition rate to operate with a sampling rate of over 120 GSPS. These numbers indicate the great potential for the method and show that the current WDM and laser technology are not the limiting factors for the bandwidth of such an ADC system.

2. **Inherent remoting:** Only the electro-optic modulator needs to be in the vicinity of the RF source. This allows TR modules to be compact and light. The other components of the ADC can be conveniently placed in a central location with only an appropriate length of optical fiber between them.

3. **Bandwidth:** The achievable bandwidth and dynamic range capability of the system may eliminate the need for downconverting and filtering stages to reduce the carrier frequency of the RF signal. This would simplify the system design and decrease the total system cost.

4. **Parallel:** The parallel nature of the back-end digitization portion of the system allows parallel processing of the signals by reducing the sampling rate requirement of each channel. This allows the use of low speed, high dynamic range electronic ADCs to digitize the RF signal at high speed, high dynamic range with currently available electronic technology.

5. **Passive:** The electro-optic modulator is a passive device allowing a completely passive receive aperture with negligible IR signature.

The critical issues for the realization of the proposed system are as follows:

1. **Pulse jitter:** The laser pulse timing jitter limits the overall dynamic range of the ADC by introducing a sampled time uncertainty into the measurement. The worst case number of bits for Nyquist sampling can be calculated from

$$N = -\log_2(\pi f \delta\tau_j)$$

where f and $\delta\tau_j$ are the maximum input frequency and timing jitter respectively. For a timing jitter of <10 fs and an input frequency of 10 GHz, the effective number of bits is calculated to be $N > 11$.

2. **Amplitude jitter:** Noise in the laser pulse sampling the signal will limit the maximum resolution of the system by introducing amplitude uncertainty into the measurement. The uncertainty in the laser pulse energy after sampling, δE, will limit the ADC system resolution by

$$N \le \log_2\left(\frac{E}{\delta E}\right)$$

where *E* is the maximum transmitted laser pulse energy. For an amplitude noise level of 0.1%, the effective number of bits is limited to N ~10 bits.

3. **Sampling rate:** The actual sampling rate of the ADC for real-time digitization is dependent on the laser repetition rate and the number of channels available on the WDM as $f_s = R_{laser} N_{WDM}$. The laser repetition rate should be limited to the speed of the electronic ADC available, currently ~1 GSPS with ~ 8 bit resolution. The optimum WDM device would have a passband just large enough to discriminate against the RF spectral spreading crossover between two channels as described above. The optimum passband can be calculated from

$$\delta\lambda_{pass} = \sqrt{\frac{\lambda_0^2}{c}\frac{\Delta\lambda}{T}}.$$

The optimum allowed parallelization of the back-end digitization would then have $\Delta\lambda/\delta\lambda_{pass}$ channels. For a commercially available laser source operating with a repetition rate of 1 GHz and a bandwidth of 50 nm, the optimum passband is $\delta\lambda_{pass}$~0.6 nm. A back-end parallel digitization system consisting of 83 channels would then allow the maximum sampling frequency obtainable with this laser.

4. **Electro-optic modulator:** The front-end bandwidth of the ADC system is limited by the bandwidth of the modulator. Current commercially available modulators have bandwidths of up to 40 GHz. The system sensitivity is also dependent on the modulator via the switching voltage.

IV. Technical Accomplishments

Low-noise Laser development

- Created a mode-locked fiber laser (MLFL): ~1 ps pulses at 1-20 GHz repetition rate.
- Demonstrated <10 fs timing jitter of short pulse (~1ps) high repetition rate (> 10 GHz) mode-locked optical pulse train (integrated over 100 Hz - 1 MHz bandwidth).
- Measured timing jitter of 1-GHz optical clock at 1550 nm at <70-fs timing jitter (100 Hz-1 MHz bandwidth).
- Generated >350-pJ pulses at 777 nm from 1-GHz Sigma laser for NG/UMD PCS triggering.
- Constructed a Frequency Resolved Optical Gating (FROG) system for characterization of femtosecond optical pulses.
- Built a multi-wavelength Sigma laser operating at a 1 GHz repetition rate with <100-fs timing jitter, <10-ps-wide pulses, and 22-nm tunability.
- Demonstrated a 10-GHz, multi-wavelength Sigma laser simultaneously generating 4 discrete wavelengths in the C-band.

Photonic ADC

- Demonstrated a highly parallel (8 channel) time/wavelength interleaved photonic sampler architecture with modulator-limited bandwidth of 18 GHz.
- Demonstrated an 8-channel, 10-GSPS WDM photonic ADC.
- Completed 2-channel back-end for demonstration of real-time Nyquist frequency digitization at up to 2.5 GSPS.
- Built and tested fully functional real-time two-channel WDM photonic A-D system with < -50 dB interleaving error.
- Demonstrated a time-wavelength interleaved photonic sampler architecture in the form of a real-time multi-channel WDM system with < -50 dB interleaving error operating at
    - 2.5 GSPS, >5-bit @ 900 MHz, 2-channel photonic ADC
    - 30-GSPS, 2-bit @ 11.4 GHz, 3-channel photonic ADC with 29.25-dB SFDR
- Reduced laser amplitude noise by >15 dB with an electro-optic modulator-based noise-eater.
- Implemented a novel digital linearization technique to increase the available modulation depth to >80% with 50-dB SFDR and showed >27-dB distortion suppression
- Demonstrated an ultra-high-speed photonic ADC: 100-GSPS, 5-bit SIAM TDM system
- Implemented an Optical Quantizer operating with 2-bits of resolution at 20 GSPS, utilizing WDM to enable wavelength-encoded digital optical outputs in parallel data streams.
- Demonstrated 50 GSPS, 2-bit and 20-GSPS, 3-bit optical quantizer limited by electro-optic modulator and detection electronics. Optical quantization of 25-GHz microwave signals with 2-bit resolution and 10-GHz microwave signals with 3-bits of resolution was achieved with a single cw laser source.

Peer Reviewed Publications

Journal Publications: 16
Conference Presentations: 11
US Patents: 4

1) Currie, M., *Optical Quantization of Microwave Signals via Distributed Phase Modulation.* submitted to Journal of Selected Topics in Quantum Electronics, 2003.
2) Lou, J.W., T.F. Carruthers, and M. Currie, *4 x 10 GHz Mode-Locked Multiple-Wavelength Fiber Laser.* submitted to IEEE Photonics Technology Letters, 2003.
3) Lou, J.W., T.F. Carruthers, and M. Currie, *Mode-locked multiple-wavelength erbium-doped fiber laser in a sigma configuration.* IEEE Photonics Technology Letters, 2002. **14**(3): p. 281-3.
4) Fatemi, F.K., *Analysis of nonadiabatically compressed pulses from dispersion-decreasing fiber.* Optics Letters, 2002. **27**(18): p. 1637-9.
5) Lou, J.W., et al. *Multiple-wavelength mode-locked erbium-doped fiber sigma laser*. in *Cleo 2001*. Baltimore MD USA: Opt. Soc. America.
6) Currie, M. *High-speed, photonic analog-to-digital conversion using phase modulation*. in *Cleo 2001*. Baltimore MD USA: Opt. Soc. America.
7) Clark, T.R., M. Currie, and P.J. Matthews, *Digitally linearized wide-band photonic link.* Journal of Lightwave Technology, 2001. **19**(2): p. 172-9.
8) Clark, T.R., Jr. and M.L. Dennis, *Toward a 100-Gsample/s photonic A-D converter.* IEEE Photonics

Technology Letters, 2001. **13**(3): p. 236-8.

9) Horowitz, M., et al., *Pulse dropout in harmonically mode-locked fiber lasers.* IEEE Photonics Technology Letters, 2000. **12**(3): p. 266-8.

10) Horowitz, M., et al., *Theoretical and experimental study of harmonically modelocked fiber lasers for optical communication systems.* Journal of Lightwave Technology, 2000. **18**(11): p. 1565-74.

11) Duling, I.N., III, R.P. Moeller, and T.R. Clark. *Active filtering of the amplitude noise of a mode-locked fiber laser*. in *Conference on Lasers and Electro Optics (CLEO 2000)*. 2000. San Francisco CA USA: Opt. Soc. America.

12) Currie, M., T.R. Clark, and P.J. Matthews, *Photonic analog-to-digital conversion by distributed phase modulation.* IEEE Photonics Technology Letters, 2000. **12**(12): p. 1689-91.

13) Clark, T.R., M. Currie, and P.J. Matthews. *Wide-band analog-digital photonic link with third-order linearization*. in *2000 IEEE MTT-S International Microwave Symposium*. 2000. Boston, MA: IEEE.

14) Carruthers, T.F., et al., *Dispersion management in a harmonically mode-locked fiber soliton laser.* Optics Letters, 2000. **25**(3): p. 153-5.

15) Kang, J.U. and R.D. Esman, *Demonstration of time interweaved photonic four-channel WDM sampler for hybrid analogue-digital converter.* Electronics Letters, 1999. **35**(1): p. 60-1.

16) Horowitz, M., et al. *Dispersion management in an actively modelocked fiber laser with Kerr nonlinearity*. in *Conference on Lasers and Electro-Optics*. 1999. Baltimore MD USA: Opt. Soc. America.

17) Clark, T.R., J.U. Kang, and R.D. Esman. *Time- and wavelength-interweaved photonic sampler for analog-to-digital conversion*. in *Conference on Lasers and Electro-Optics.* 1999. Baltimore MD USA: Opt. Soc. America.

18) Clark, T.R., P.J. Matthews, and M. Currie. *Real-time photonic analog-digital converter based on discrete wavelength-time mapping*. in *International Topical Meeting on Microwave Photonics*. 1999. Australia: IEEE.

19) Clark, T.R., J.U. Kang, and R.D. Esman, *Performance of a time- and wavelength-interleaved photonic sampler for analog-digital conversion.* IEEE Photonics Technology Letters, 1999. **11**(9): p. 1168-70.

20) Clark, T.R., et al. *Sub-10 femtosecond timing jitter of a 10-GHz harmonically mode-locked fiber laser.* in *OFC/IOOC'99*. 1999. San Diego, CA, USA: IEEE.

21) Clark, T.R., et al., *Phase noise measurements of ultrastable 10 GHz harmonically modelocked fibre laser.* Electronics Letters, 1999. **35**(9): p. 720-1.

22) Carruthers, T.F., et al. *Enhanced stability of a dispersion-managed, harmonically mode-locked fiber laser*. in *Conference on Lasers and Electro-Optics*. 1999. Baltimore MD USA: Opt. Soc. America.

23) Carruthers, T.F., et al. *A dispersion-managed, harmonically mode-locked fiber soliton laser*. in *LEOS'99*. 1999. San Francisco, CA, USA: IEEE.

24) Kang, J.U., M.Y. Frankel, and R.D. Esman. *Characterization of a hybrid photonic analog-digital converter based on WDM technique*. in *LEOS'98*. 1998. Orlando FL USA: IEEE.

25) Kang, J.U., M.Y. Frankel, and R.D. Esman, *Highly parallel pulsed optoelectronic analog-digital converter.* IEEE Photonics Technology Letters, 1998. **10**(11): p. 1626-8.

26) Frankel, M.Y., J.U. Kang, and R.D. Esman, *High-performance photonic analogue-digital converter.* Electronics Letters, 1997. **33**(25): p. 2096-7.

27) Carruthers, T.F. and I.N. Duling, III, *10-GHz, 1.3-ps erbium fiber laser employing soliton pulse shortening.* Optics Letters, 1996. **21**(23): p. 1927-9.

US Patents:

1) 6,100,831 - Frankel, M. “Optoelectronic Analog-to-digital converter using wavelength division multiplexing,” 2000.
2) 6,404,366 – Currie, M., Clark, T., Matthews,P.,”Photonic Analog-to-digital converter utilizing wavelength division multiplexing and distributed phase modulation,” 2002.
3) Currie, M., “Hybrid photonic analog-to-digital converter using superconducting electronics,” US Patent applied for Jan. 2003.
4) Lou, J., Clark, T.R., Currie, M., Carruthers, T.F., “Multiple wavelength pulsed source,” US Patent applied for Sept. 2002.

V. Low-Noise Optical Clocks

A. The Sigma Laser

Critically important to a high-speed photonic ADC is a stable, low-noise optical clock. The clock's role in the system is in sampling the high-speed microwave signal with extreme precision. This requires a clock with minimal timing jitter and a short duration.

Such a source is found in the high-repetition-rate optical sources for ≥100 Gbit/s fiber communications whose pulse durations are ≤ 2 ps, with no pulse dropouts, and low phase and amplitude noise. Passively mode-locked Er fiber lasers easily produce the picosecond-duration pulses needed for multigigabit communication systems, but such lasers are prone to pulse dropouts, multiple pulsing, and erratic timing when more than one pulse circulates in their cavities [1,2]. Actively mode-locked lasers produce pulses with excellent phase stability and without dropouts [3], but pulse durations are significantly longer than those of passively mode-locked lasers [4], especially when etalons are added to stabilize the supermode order [5]. Hybrid active and passive mode-locking can produce subpicosecond pulses with little phase noise, but the pulse train can be prone to pulse dropouts; in addition, passive mode-locking mechanisms are generally inefficient, and the lasers cannot be operated at high repetition rates [6]. Modulated optical sources, generally followed by an Er fiber amplifier and compressed in a length of fiber [7,8] can produce picosecond pulses with no dropouts, but pulse durations are generally longer than a few picoseconds and the output is still prone to environmentally-induced phase noise originating in the fiber.

Martinez *et al*. [9] and Haus and Silberberg [10] predicted that self-phase modulation (SPM) and group velocity dispersion (GVD) could shorten pulses in a mode-locked laser. Kafka et al. [11] demonstrated soliton pulse shortening in an actively mode-locked Er fiber laser by adding fiber to the laser cavity and observing a dramatic decrease in the output pulse duration.

Recent theoretical and experimental work [12,13] has shown that the degree of soliton pulse shortening that can be attained depends on the ratio of the cavity's GVD to its gain dispersion. The experimental systems analyzed in these works were femtosecond, high-peak-power, MHz repetition rate solid state lasers; we demonstrate here that the same principles can act in low-power picosecond fiber lasers operating at much higher repetition rates.

We have developed an actively mode-locked Er fiber laser that utilizes intracavity soliton formation to produce a completely filled pulse train with a pulse duration of 1.3 ps at repetition rates in excess of 10 GHz—well below the Kuizenga-Siegman limit of ~5 ps for this laser. Allowing the pulses to evolve within the laser cavity has several benefits over extracavity soliton pulse evolution: the pulse energies circulating within the laser are significantly higher than those coupled out, so soliton evolution is easily attained in a relatively short cavity; the average cavity dispersion can be controlled, so that the pulse duration and energy of a propagating soliton can be tailored to the desired repetition rate and available optical amplifier power; and the cavity length can be actively controlled to eliminate environmental contributions to the phase noise. The laser is driven by an external oscillator, allowing it to be synchronized to a master clock in an optical fiber communications system. Its components are polarization-maintaining (PM) or are birefringence-compensated, making the laser insensitive to environmentally-induced birefringence variations.

The laser, sketched in Figure 1, is fabricated in a sigma configuration, in which a PM loop is connected to a non-PM branch with a polarizing beamsplitter. A 45° Faraday rotator and mirror, called a Faraday mirror, compensates birefringence variations in the non-PM branch [14,15]. This configuration allows the use in a single-polarization laser of fiber types that may be scarce or nonexistent as PM fiber. A Mach-Zehnder modulator, driven by a 10-GHz sine wave, harmonically mode locks the laser; ~9960 pulses circulate in the 192-m effective cavity length.

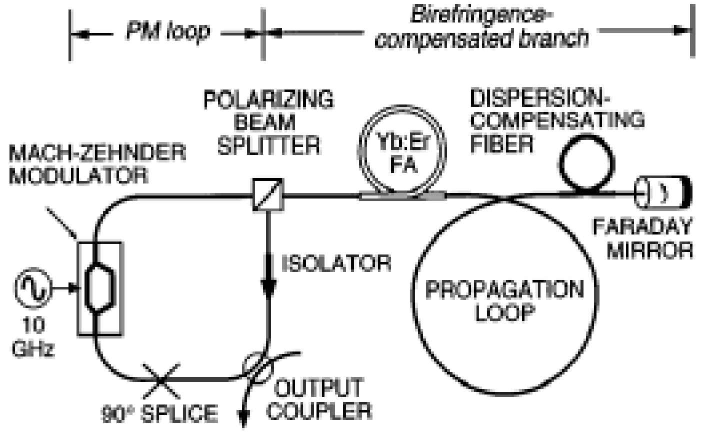

Fig. 1—Sketch of the actively mode-locked soliton laser. The Yb:Er fiber amplifier (Yb:Er FA) has a saturated output power of 200 mW. The propagation loop, consisting mainly of dispersion-shifted fiber, is 90 m in length.

The non-PM branch contains ~10 m of Yb:Er-doped gain fiber, pumped by diode-pumped Nd solid-state lasers, which has a saturated output power of ~23 dBm at 1565 nm. Also in this branch are 14.9 m of dispersion-compensating fiber, which reduces the average anomalous dispersion <D> of the laser cavity to 2.0 ps/(nm·km), and the cavity length stabilization element described below, which contains 60 m of dispersion-shifted fiber. Linearly-polarized light exits the laser through a 20% output coupler in the PM loop.

Proper operation depends critically upon the laser's maintaining an optimum length with respect to its operating frequency. A length-stabilizing feedback system uses the phase of the output pulses relative to the clock oscillator signal to generate an error signal [16]; the relative phase (with an appropriate offset) is measured with two limiting microwave amplifiers and a phase detector. The error signal is fed to an integrator with a 10-ms integrating time constant. Its output is amplified and drives a piezoelectric transducer cylinder, around which is wound the dispersion-shifted fiber. The fiber coil can change the effective cavity length by 0.9 cm, and the feedback system is capable of maintaining the cavity length within the necessary ~2-μm precision.

The autocorrelation function and optical spectrum of the pulses are shown in Fig. 2. At higher autocorrelation intensities the data fit a Gaussian more closely than a sech^2 autocorrelation function. The tail clearly possesses the exponential nature of a sech^2 pulse, however, as is shown in the semilogarithmic plot of the autocorrelation function in Fig. 3. The pulses show no sign of a background or pedestal. The autocorrelation full width at half-maximum (fwhm) is 1.9 ps, yielding a Gaussian pulse duration of 1.35 ps (or 1.25 ps assuming a

sech^2 profile). The optical output power of 8.3 mW corresponds to a pulse energy of 4.1 pJ inside the laser cavity, somewhat higher than expected for a 1.3-ps soliton.

The optical spectrum has a fwhm of 3.76 nm, yielding a time-bandwidth product of 0.62, 41% above the transform limit of 0.44 for a Gaussian pulse. Since a pulse evolves during its circuit through the laser, a different extraction point than the one used might yield better pulse parameters. However, soliton-like pulses with Gaussian intensity profiles are commonly seen in periodic systems containing fibers of differing dispersion [17]; such systems can also contain stable high-energy pulses with high time-bandwidth products [18].

Because the laser contains no passive mode-locking mechanism, we do not expect to see dropouts in its output pulse stream. We have measured the pulse dropout ratio to be less than 10^{-12} by driving the laser at 10 GHz and searching its output for missing pulses with a bit error-rate tester. Upper bounds of 0.16 ps and 1.1% to the time and amplitude jitter, respectively, in the pulse train were calculated by measuring and integrating the RF phase noise out to 200 kHz from the modulation frequency [19,20].

Recent experiments have convinced us that the non-PM branch plays an important role in ensuring a filled pulse train. Nonlinearly propagating light in the non-PM branch generally undergoes an intensity-dependent polarization rotation; but the rotated component is rejected from the cavity by the polarizing beamsplitter. The consequent intensity-dependent loss encourages the production of a completely filled pulse train [21].

According to the soliton model of Kärtner et al. [13], the factor R by which pulse durations are reduced below the Kuizenga-Siegman active mode-locking limit is given by

$$R \le R_{\max} \approx 1.37 \sqrt[4]{\frac{\beta_2 l}{g/\Omega_g^2}} \qquad (1)$$

where $\beta_2 = \lambda^2 \langle D \rangle / (2\pi c)$ is the GVD, l is the laser's effective cavity length, g is its steady-state gain and Ω_g is its gain bandwidth. For our laser the maximum expected reduction is $R_{max} \approx 4.4$; our estimate of the experimental value of R is 3.7. The approximately linear dependence of pulse duration on average power presented in Fig. 4 suggests that we have not yet attained the maximum degree of soliton pulse shortening; Eq. (1) predicts a minimum pulse duration of ~1.15 ps for a sufficiently high average pulse power.

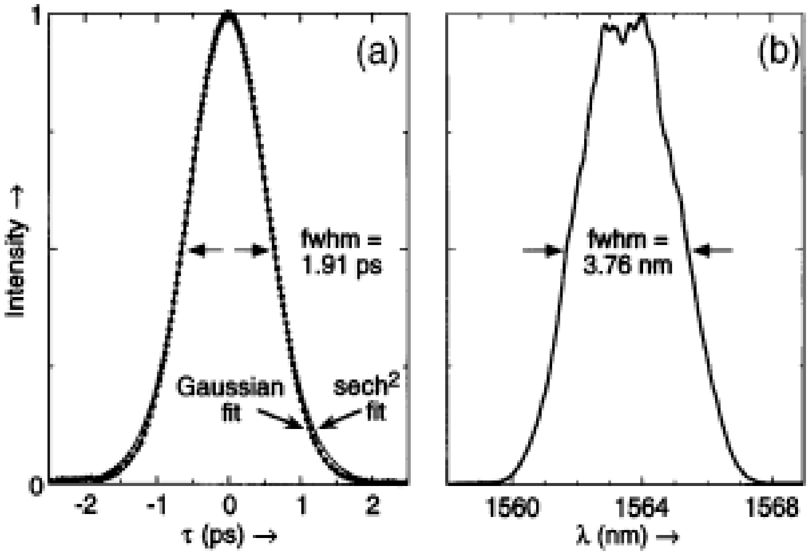

Fig. 2—(a) Time autocorrelation and (b) spectrum of the laser output at an average power of 8.3 mW. In (a), the points represent autocorrelation data; the lines are fits to the data assuming Gaussian or sech^2 pulse profiles.

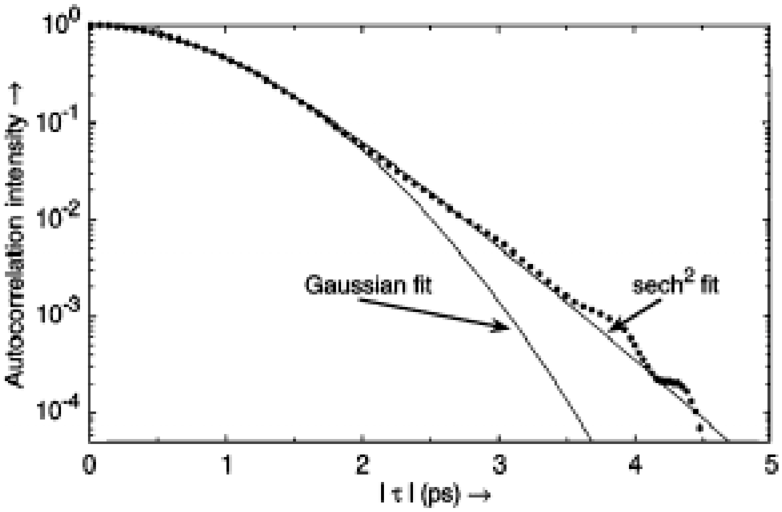

Fig. 3—Semilogarithmic plot of the autocorrelation function data of Fig. 2, indicated by points, and fits to the data assuming Gaussian and sech^2 pulse profiles, indicated by curves.

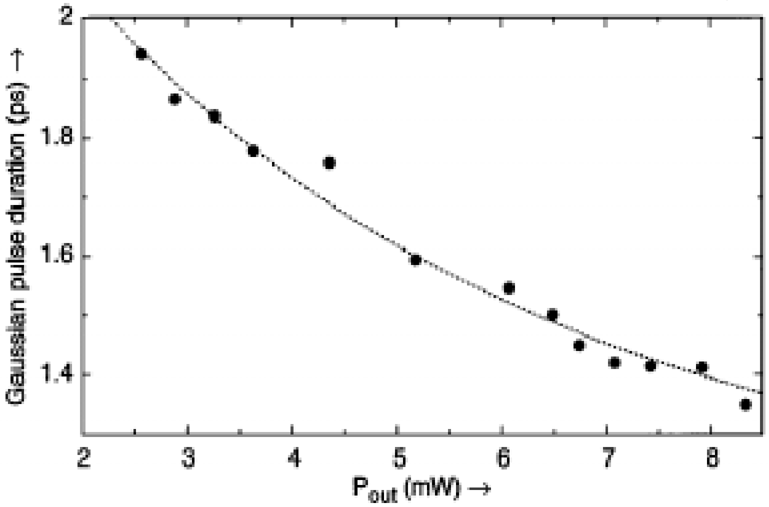

Fig. 4—Output pulse durations as a function of the average power of the output pulses. The dotted line is a phenomenological fit to the data.

As expected in a soliton laser, if the degree of SPM is decreased by reducing the pump power and therefore the average pulse power, the pulses increase in duration. Figure 4 demonstrates that the pulse duration may be varied between 1.35 and 1.9 ps by this means; even in these low-power conditions, the laser produces a completely filled pulse train. We have also reduced the pulse duration to 1.15 ps by increasing <D> to 2.6 ps/(nm·km) by removing 1.4 m of the dispersion-compensating fiber; the cost of the shorter pulses is a higher soliton energy and therefore a lower maximum repetition rate of the laser. We anticipate that the present laser could be mode-locked at frequencies well in excess of 10 GHz if <D> is lowered so that soliton-like pulses with a lower pulse energy can be produced.

We have developed an externally-clocked, environmentally stable single-polarization fiber soliton laser which uses non-PM gain and dispersion-compensating fibers; it is capable of producing 1.35-ps pulses at repetition rates in excess of 10 GHz with low amplitude and phase noise and with a measured pulse dropout ratio less than 10^{-12}. This laser fulfills the requirements needed for a stable, low-noise, optical clock for a photonic ADC system.

REFERENCES

1. C.-J. Chen, P. K. A. Wai, and C. R. Menyuk, Opt. Lett. 19, 198 (1994).
2. D. J. Richardson, R. I. Laming, D. N. Payne, V. J. Matsas, and M. W. Phillips, Electron. Lett. 27, 1451 (1991).
3. H. Takara, S. Kawanishi, M. Saruwatari, and K. Noguchi, Electron. Lett. 22, 2095 (1992).
4. Dirk J. Kuizenga and A. E. Siegman, IEEE J. Quantum Electron., QE-6, 694 (1970).
5. G. T. Harvey and L. F. Mollenauer, Opt. Lett. 18, 107 (1993).
6. Thomas F. Carruthers and Irl N. Duling III, Electron. Lett. 30, 1051 (1994).
7. D. G. Moodie, A. D. Ellis and C. W. Ford, Electron. Lett. 30, 1700 (1994).
8. S. V. Chernikov, J. R. Taylor, *et al.*, in OFC '95, vol. 8, Technical Digest Series (Washington DC, 1995), p. 294.
9. O. E. Martinez, R. L. Fork, and J. P. Gordon, Opt. Lett. 9, 156 (1984).
10. H. A Haus and Y. Silberberg, IEEE J. Quantum Electron. QE-22, 325 (1986).
11. J. D. Kafka, T. M. Baer and D. W. Hall, Opt. Lett. 14, 1269 (1989).
12. D. Kopf, F. X. Kärtner, K. J. Weingarten and U. Keller, Opt. Lett. 24, 2146 (1994).
13. F. X. Kärtner, D. Kopf, and U. Keller, J. Opt. Soc. Am. B 12, 486 (1995).
14. Mario Martinelli, Opt. Commun. 72, 341 (1989).
15. I. N. Duling and R. D. Esman, Electron. Lett. 28, 1126 (1992).
16. X. Shan, D. Cleland, and A. Ellis, Electron. Lett. 28, 182 (1992).
17. H. A. Haus, K. Tamura, L. E. Ne.son, and E. P. Ippen, IEEE J. Quantum Electron. 31, 591 (1995).
18. N. J. Smith, F. M. Knox, N. J. Doran, K. J. Blow and I. Bennion, Electron. Lett. 32, 54 (1996).
19. D. von der Linde, Appl. Phys. B 39, 201 (1986).
20. Ursula Keller, Kathryn D. Li, *et al.*, IEEE J. Quantum Electron. QE-25, 280 (1989).
21. M. Nakazawa, K. Tamura and E. Yoshida, Electron. Lett. 32, 461 (1996).

B. Multiple-Wavelength Sigma Laser

1) Tunable, 2-wavelength Sigma Laser

The simultaneous generation of short pulses at multiple wavelengths is particularly useful for a photonic ADC system. The laser should have tunable wavelengths to allow the user to choose whichever wavelength is needed, or to scan over a range of wavelengths. Synchronized outputs at multiple-wavelengths eliminate the need for synchronization of multiple laser systems. Short pulses of less than 10 ps are needed for GHz repetition rates. And finally, a practical optical source should have timing jitter much less than the bit period. We created a novel configuration for a multiple-wavelength erbium-doped fiber laser based on the sigma configuration [1], which meets the above criteria.

Previously, mode-locked pulse generation at multiple-wavelengths has been studied in various configurations of erbium-doped fiber lasers. The focus has primarily been on variations in the ring cavity design. Schlager, *et al.*, have proposed a method that incorporates 3.4 km of birefringent fiber and a polarizing isolator in the cavity [2]. Other techniques for selecting the wavelength for ring cavity lasers utilize fiber Bragg gratings [3-6], power splitters and bandpass filters [7], and dense-wavelength-division-multiplexers [8]. Passively mode-locked lasers are demonstrated in a figure-eight configuration by Noske, *et al.* [9] and in a linear configuration by Okhotnikov, *et al.* [10]. Pattison, *et al.*, have demonstrated an actively-modelocked linear cavity laser with fiber gratings as the ends of the cavity and a nonlinear optical loop mirror in the middle [11]. A modified sigma configuration laser, which used a circulator followed by cascaded fiber gratings in a second arm [12], is demonstrated by Deparis, *et al.* These lasers produce either broad pulse widths (>10 ps) or wide wavelength separations ($\Delta\lambda$ >15 nm). This limits the ability of the laser to produce high repetition rates and limits the total number of wavelengths that are possible within the gain bandwidth of the amplifying media. Additionally, wide wavelength tuning ranges have not yet been demonstrated.

The setup of the multiple-wavelength laser is shown in Fig. 1. The design is similar to the single-wavelength sigma laser described in Ref. 1, which has been shown to exhibit low amplitude and phase noise [13,14]. A polarization-maintaining loop contains a Mach-Zehnder modulator and an isolator; the loop is connected via a polarizing beamsplitter to a birefringence-compensating branch, which is terminated with Faraday mirrors; the latter elements allow the laser to operate in a single polarization state [1].

The laser is harmonically mode-locked at 960 MHz; the fundamental repetition rate of the laser is 308 kHz. The modulator is driven with ~100-ps duration pulses from a step-recovery diode, which is driven by a 960-MHz synthesizer.

Two-wavelength operation is attained by splitting part of the birefringence-compensating branch into two arms with a 3-dB coupler. Each section contains a 0.8-nm manually-tunable bandpass filter, an adjustable fiber delay line, and a variable attenuator. The delay lines are adjusted to ensure that the different wavelength pulses arrive at the modulator at the same time, and the attenuators balance the net gain for each wavelength. A Faraday mirror completes each arm.

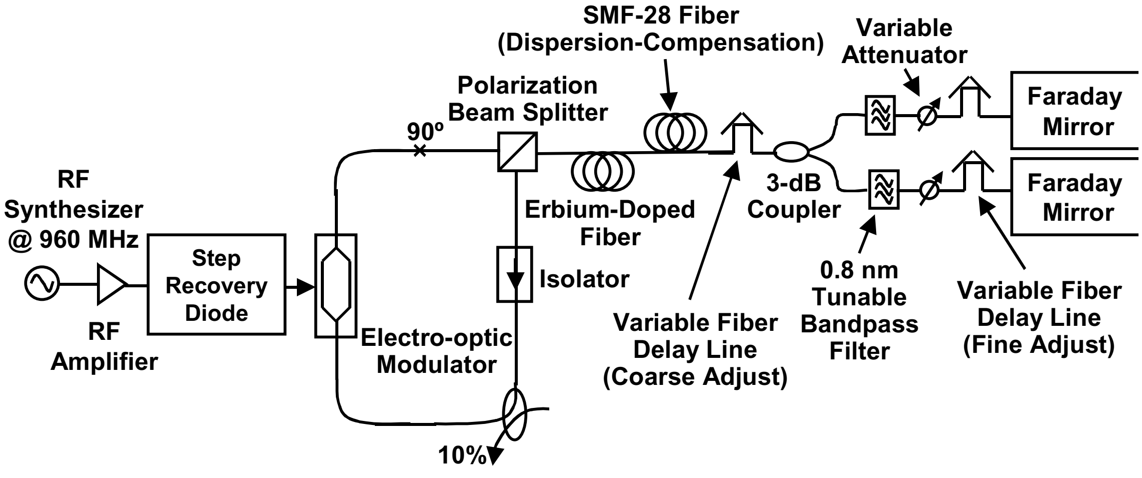

Figure 1—Schematic diagram of multiple-wavelength sigma laser. The different wavelength pulses in the cavity share the same gain medium, but each wavelength passes through a separate bandpass filter, attenuator, fiber delay line, and Faraday mirror.

The saturation power of the ~18-m length erbium-doped fiber, pumped with ~110 mW from a 980-nm laser diode, is approximately 15 mW. The full pump power is always used to ensure enough gain for both wavelengths. Intra-cavity dispersion compensation is provided by approximately 270 m of SMF-28 standard fiber. The net dispersion of the cavity is about 11.6 ps/nm/km. By adding (or taking away) dispersive optical fiber, we can adjust the net dispersion in the cavity and achieve transform-limited pulses over a range of wavelengths.

Variable wavelength separation operation is illustrated in Fig. 2, where one wavelength is fixed at 1538 nm and the other wavelength is tuned continuously from 1541.5 nm to 1562 nm. For any given $\Delta\lambda$, no drift of the peak wavelengths is observed. The maximum tuning range is set by the erbium gain bandwidth. Because of the dispersion in the cavity, it is necessary to tune the cavity length for each wavelength, and therefore the maximum tuning range of the cavity length also determines the maximum $\Delta\lambda$. The required tuning is approximately 2 mm of the double-pass free-space delay stage for every nanometer of wavelength shift, and it can be reduced by reducing the overall cavity dispersion. The minimum $\Delta\lambda$ is fundamentally limited by the homogeneous linewidth of the erbium-doped fiber [15]. Zyskind, *et al.*, measured the

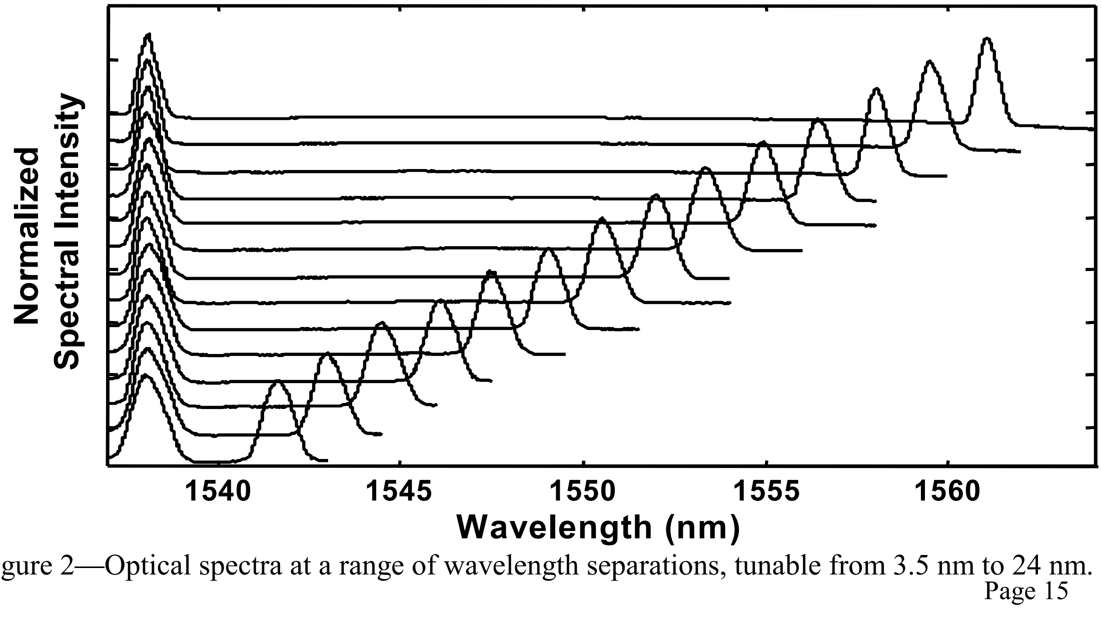

Figure 2—Optical spectra at a range of wavelength separations, tunable from 3.5 nm to 24 nm.

homogeneous linewidth at low temperatures and extrapolated the results to room temperature, determining the linewidth to be ~3 to 4 nm [16]. If the wavelength separation is less than the homogeneous linewidth (~3.5 nm in this case), gain competition between the wavelengths results in noisy operation. That is, while both wavelengths may continue to lase, pulse dropouts are observed, and eventually the lasing action of one wavelength will dominate over the other. We have observed that a $\Delta\lambda$ as small as 3 nm at 1550 nm and 1553 nm operates stably, without any evidence of power fluctuations due to gain competition.

Both wavelengths exit the laser at the same time. The laser has no pulse dropouts, as evidenced by the greater than 70 dB supermode suppression shown in Fig. 3. We show the cross-correlation between the two wavelengths for the case of 3.5-nm separation (Fig. 4(a)) and for 22-nm separation (Fig. 4(b)). The cross-correlation between the 1538-nm pulse and the 1560-nm pulse appears broader because the pulse at 1560 nm experiences higher dispersion in the cavity than the 1541.5 nm pulse and as a result is broader in time. For longer wavelengths (such as 1560 nm), the net dispersion should be lowered to achieve closer to transform-limited pulses.

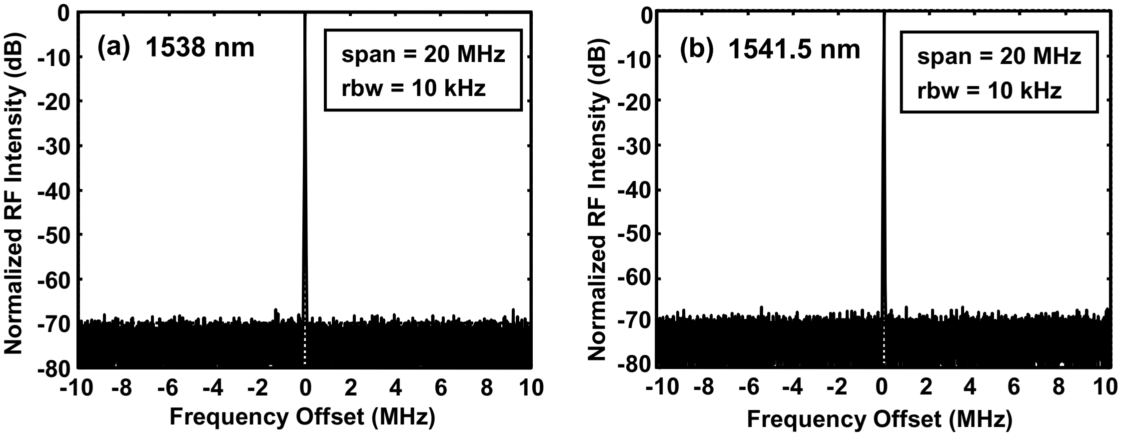

Figure 3—RF spectrum of pulses at (a) 1538 nm and (b) 1541.5 nm. Supermode suppression is greater than 70 dB over a span of 20 MHz with 10 kHz resolution bandwidth.

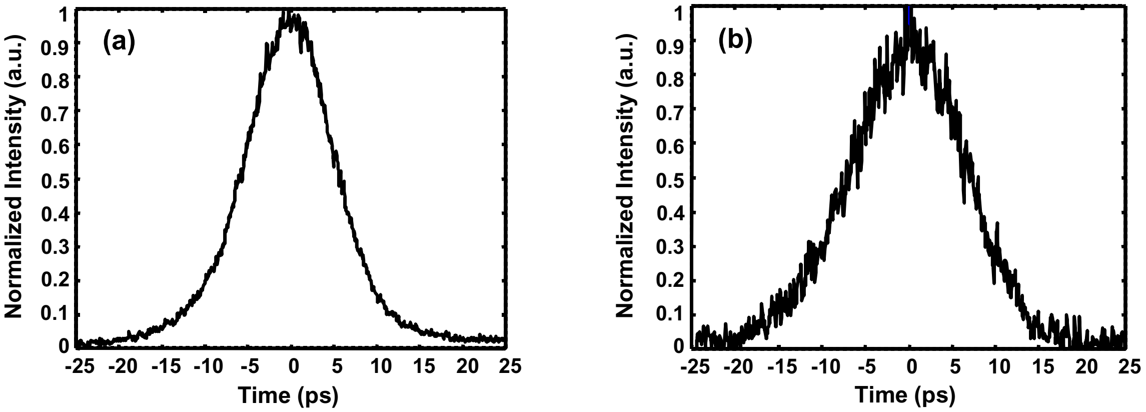

Figure 4—Cross-correlation of pulses at (a) 1538 nm and 1541.5 nm, and (b) 1538 nm and 1560 nm.

As an example, we look at the near transform-limited pulse outputs at 1538 nm and 1541.5 nm. The autocorrelations and spectra for both wavelengths are shown in Fig. 5. The output wavelengths are separated using 0.9-nm bandpass filters. The pulses at 1538 nm and 1541.5 nm both have full-width at half-maximum pulse widths of approximately 6.7 ps, a spectral width of 0.35 nm at 1538 nm and a width of 0.37 nm at 1541.5 nm, and an average power of 0.28 mW in total. The time-bandwidth product is 0.3 and 0.31 for the 1538-nm and 1541.5-nm pulses, respectively. This is consistent with transform-limited hyperbolic-secant pulse shapes.

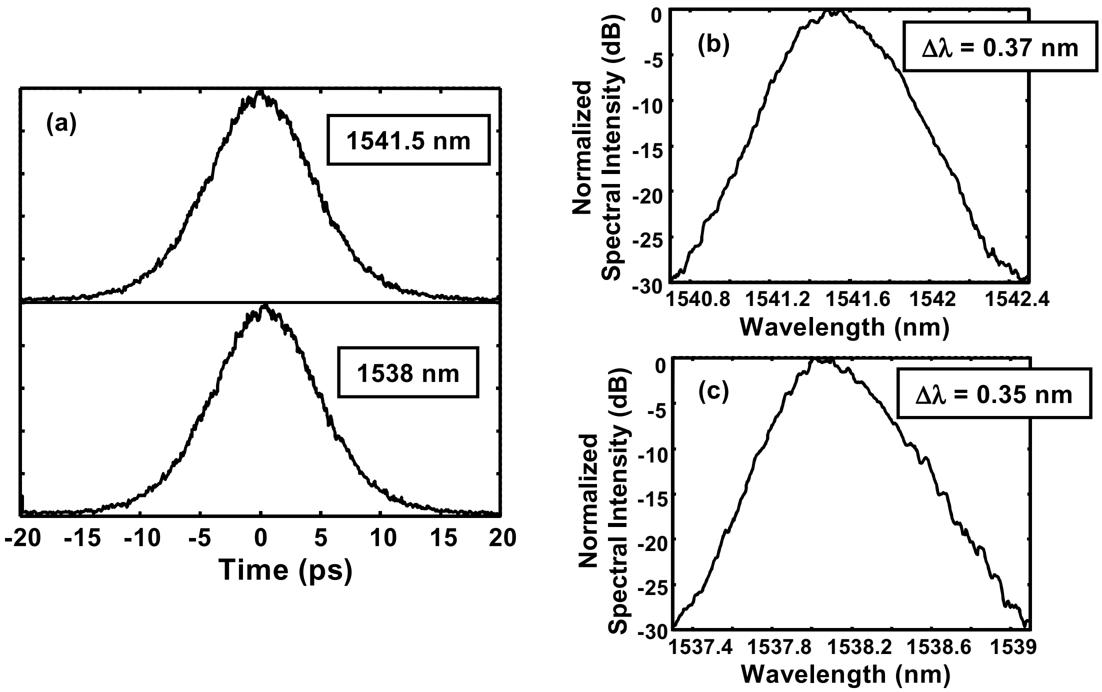

Figure 5—(a) Autocorrelations of pulses at 1538 nm and at 1541.5 nm. Both pulse widths are approximately 6.7 ps. (b) Pulse spectra at 1541.5 nm ($\Delta\lambda = 0.37$ nm). (c) Pulse spectra at 1538 nm ($\Delta\lambda = 0.35$ nm).

We also measured the amplitude and phase noise of this laser; both wavelengths appear to have similar noise characteristics. The measured single-sideband amplitude noise for 1538 nm and 1541.1 nm are shown in Fig. 6(a) (zero-area spurs have been removed). The measured single-sideband phase noise, with the spurs removed, is shown in Fig. 6(b). We have not implemented any laser cavity stabilization scheme as with other sigma cavity lasers [1] and thus, over the time period of the measurement, we see a slow drift that is manifested as low frequency noise. Nevertheless, if we integrate the data from 10 Hz to 1 MHz, we find less than 0.5% amplitude fluctuation and timing jitter less than 800 fs. To remove the effect of the slow drift, which in practice could be removed with active cavity stabilization, we integrate from 1 kHz to 1 MHz and find less than 68 fs timing jitter. The drift of the cavity-length limits the overall stability of the laser. Allowing *only* cavity-length adjustments, dual-wavelength operation can be maintained for at least several hours.

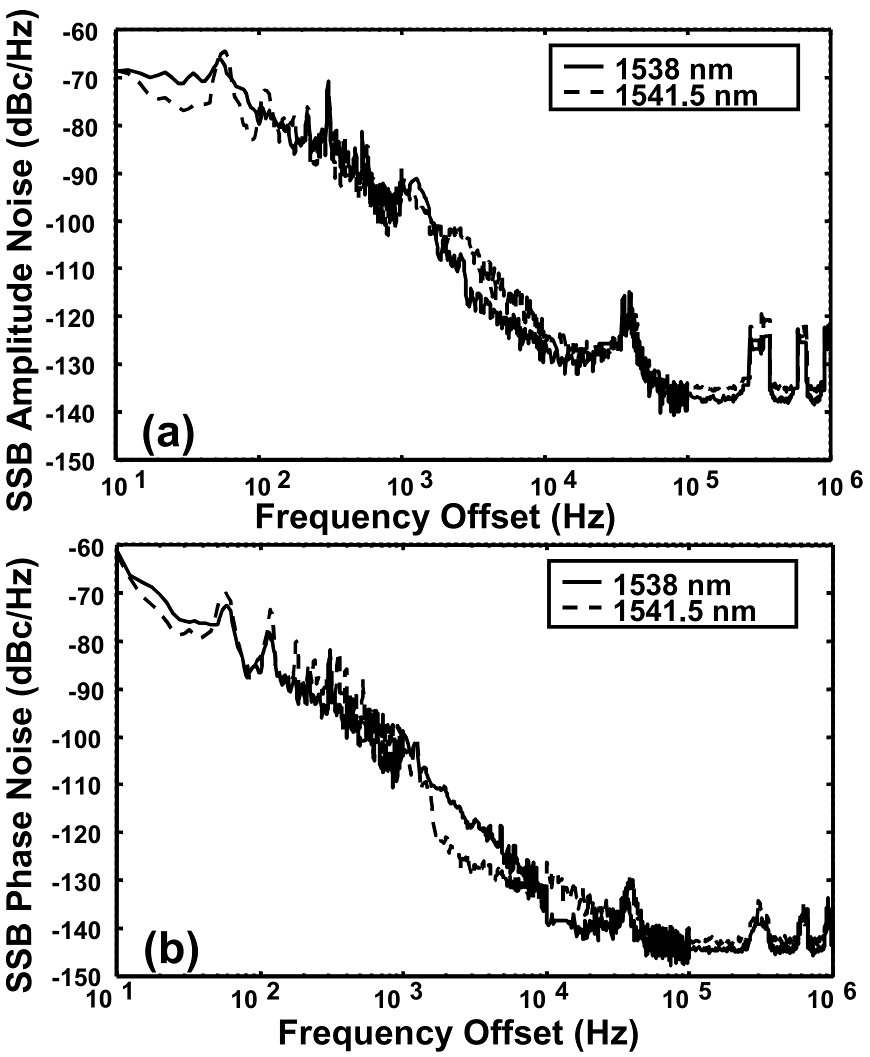

Figure 6—(a) Single-sideband amplitude noise, with zero-area spurs removed, versus frequency offset from the carrier frequency. The amplitude fluctuation is < 0.5% (10 Hz to 1MHz). (b) Single-sideband phase noise, with zero-area spurs removed, versus frequency offset from the carrier frequency. The timing jitter is < 68 fs (1 kHz to 1 MHz).

We have demonstrated a sigma laser capable of simultaneously generating pulses at multiple wavelengths, using the same physical gain fiber. The wavelength separation is tunable from the limit of the homogeneous linewidth to the limit of the erbium gain bandwidth. Two different center wavelengths (1538 nm and 1541.5 nm) are shown to have nearly transform-limited, 6.7-ps, pulses with low noise. The amplitude fluctuation is less than 0.5% (10 Hz to 1 MHz) and the timing jitter is less than 68 fs (1 kHz to 1 MHz). In general, appropriate cavity-dispersion compensation is necessary to achieve transform-limited pulses.

The two-wavelength sigma laser has the same potential for high repetition-rate and low pulse-duration as its single-wavelength counterpart. Extension to higher repetition rate and more wavelengths will require more gain. Additionally, with active stabilization, it can achieve low amplitude and phase noise operation.

2) 4 x 10 GHz Sigma Laser

We have created a 4-wavelength 10-GHz mode-locked erbium-doped fiber laser, with wavelength spacing of 3-5 nm. Nearly transform-limited gaussian pulses are measured and all wavelengths are synchronous.

The setup of the multiple-wavelength laser is shown in Fig. 1. The design is similar to the single-wavelength sigma laser described in Ref. 1. A polarization-maintaining loop contains a Mach-Zehnder modulator and an isolator; the loop is connected via a polarizing beamsplitter to a birefringence-compensating branch, which is terminated with Faraday mirrors; the latter elements allow the laser to operate in a single polarization state [1]. The laser is harmonically mode-locked at 10 GHz; the fundamental repetition rate of the laser is ~900 to 950 kHz. The modulator is driven with the 10-GHz output of an RF synthesizer.

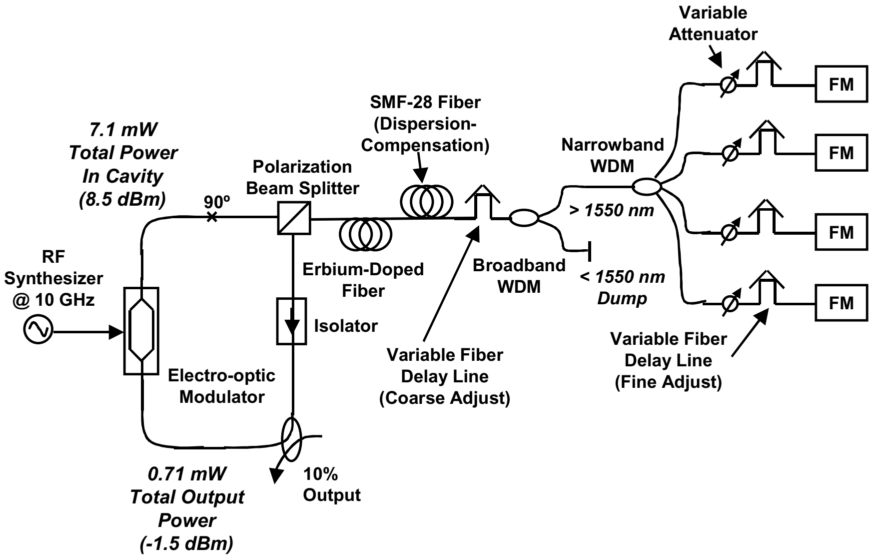

Figure 1—Experimental setup. FM = Faraday Mirror. The four wavelengths are at 1550.7 nm, 1554.25 nm, 1559.5 nm, and 1563.5 nm. The fundamental repetition rate is between 900 and 950 kHz and the average dispersion is approximately 3 ps/nm/km.

Four-wavelength operation is attained by using wavelength-division-multiplexers (WDMs) to split the birefringence-compensating branch. The broadband WDM is used to suppress the gain peak at 1535 nm and thus, only the greater than 1550-nm passband output is used. The second WDM is used to split the optical bandwidth into four arms. The extinction ratio of the second WDM is greater than 40 dB between adjacent channels and the 3-dB channel bandwidth is approximately 2.5 nm. Each WDM channel is followed by an adjustable fiber delay line, a variable attenuator, and a Faraday mirror. The delay lines are adjusted to ensure that the different wavelength pulses arrive at the modulator at the same time, and the attenuators balance the net gain for each wavelength. The erbium-doped fiber is 17.2 m in length and pumped with ~150 mW using a 980-nm laser diode. The total laser output power at 10 GHz is 0.79 mW.

The net dispersion of the cavity is measured to be approximately 3 ps/nm/km. Intra-cavity dispersion compensation is provided by approximately 50 m of SMF-28 standard fiber. We determine the dispersion by first replacing the WDM with a tunable bandpass filter. Then while maintaining the same RF drive frequency, we tune the wavelength and record the corresponding time change in the coarse delay line required to maintain good mode-locking. We also obtain from the detected RF spectrum the fundamental repetition rate of the laser, which gives the total cavity length. Finally, we use a 3-term Sellmeier equation to fit the data to obtain the chromatic dispersion of the cavity. For our cavity, the change from the bandpass filter to the WDM yields negligible changes in the overall cavity dispersion.

We show the autocorrelations for each of the four output wavelengths in Fig. 2 and for all four wavelengths in Fig. 3. The full-width at half-maximum pulse widths are approximately 11-14 ps. The autocorrelation of the total output (4 wavelengths) shows a distinct interference pattern due to the presence of frequency combs with fixed phase relationships. That is, each wavelength contributes to a pulse in time and its combination with one or more other wavelengths contributes to a new pulse, which is the sum of the electric fields that make up the corresponding pulses in time. Because the sum of the electric fields has constructive and destructive interference, as long as the phase relationship between the fields is constant, the new pulse that is the sum of all four wavelengths shows an interference pattern in time.

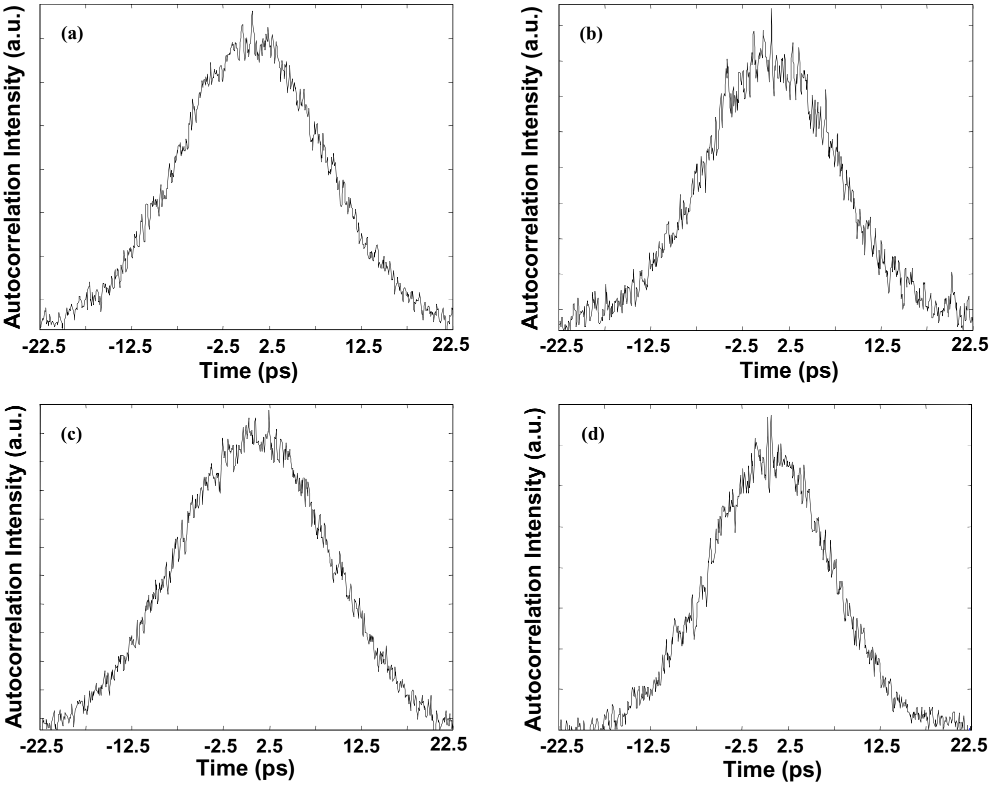

Figure 2—Autocorrelation of each of the 4 wavelengths: (a) 1550.7 nm, (b) 1554.25 nm, (c) 1559.5 nm, and (d) 1563.5 nm.

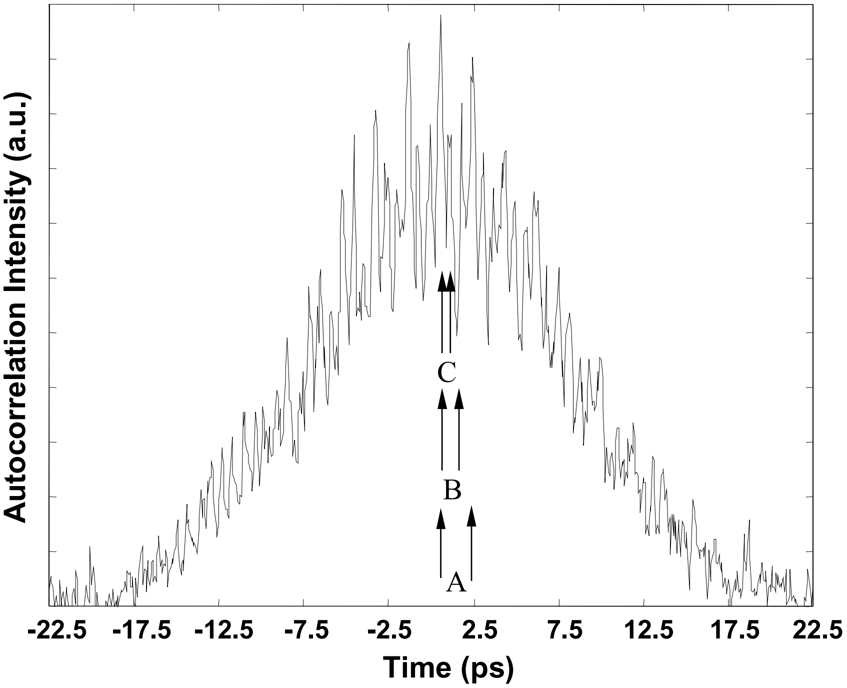

Figure 3—Autocorrelation of all 4 wavelengths simultaneously. Interference patterns due to: A = 1550.7 nm and 1554.25 nm, B = 1550.7 nm and 1559.5 nm, C = 1550.7 nm and 1563.5 nm.

Figure 4 shows the four individual output wavelengths, which are separated using a 0.9-nm bandpass filter, and Fig. 5 shows all four simultaneously lasing wavelengths. The spectral widths of the individual wavelengths are ~0.25 nm. The corresponding time-bandwidth products range from 0.34 to 0.44. This is consistent with near transform-limited hyperbolic-secant and gaussian pulse shapes. Note the 10-GHz modulation in the spectra denoting high supermode suppression and low interpulse timing jitter.

The modes that define each wavelength pulse are not locked to the modes from any other wavelength pulse. Thus, as a result of different carrier-phase envelope offsets, the modes at the edges of each pulse spectrum can occasionally be observed to interfere with the leakage modes of another pulse spectrum. This can lead to pulse instabilities and is suppressed by higher extinction ratio WDM's or by locking the carrier-phase envelope offset using an external phase-locked-loop. When mode-locked, each of the wavelengths has supermode sideband suppression of greater than 60 dB, which indicates that there are no pulse dropouts.

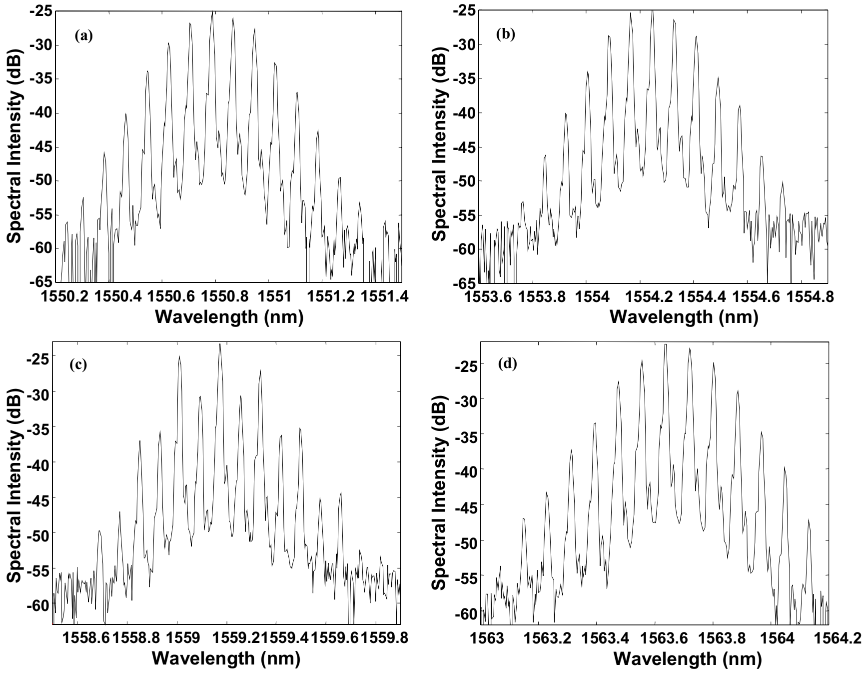

Figure 4—Spectrum of each of the 4 wavelengths: (a) 1550.7 nm, (b) 1554.25 nm, (c) 1559.5 nm, and (d) 1563.5 nm.

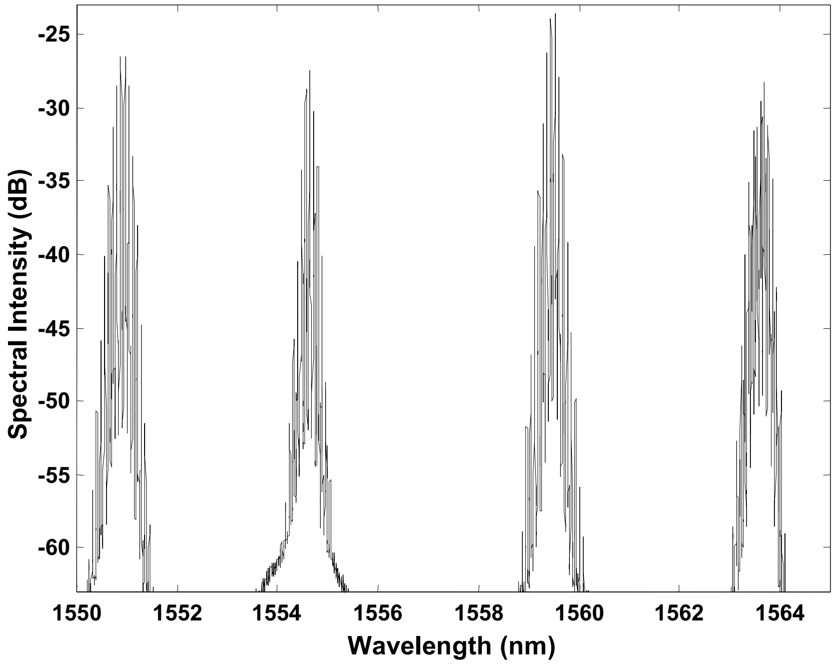

Figure 5—Spectrum of all 4 wavelengths simultaneously.

Using a 40-GHz photodetector, we measure the relative timing between the different wavelengths. Figure 6(a) shows the response of the photodetector to all 4 wavelengths at the laser output, as observed on an oscilloscope. There is only ~15 m of standard fiber between the laser output and the oscilloscope and thus, all the wavelengths are overlapped in time. However, after propagating through 1 km of standard fiber, we observe a time separation of the different wavelength pulses as illustrated in Fig. 6(b) due to the dispersion of the propagation fiber. The wavelengths are separated with time differences consistent with a fiber dispersion of 17.5 ps/nm/km. The variations in the pulse amplitude are due to a combination of different pulse powers and the nonlinear response of the photodetector.

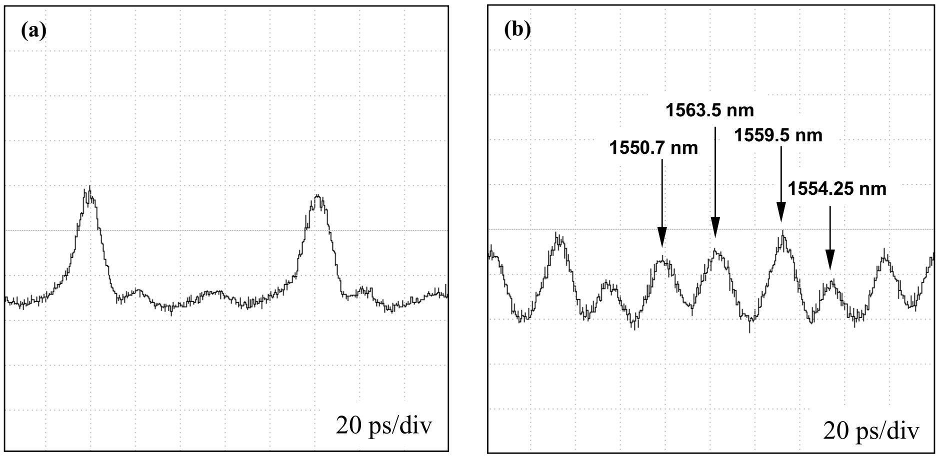

Figure 6—(a) Detected signal of laser output with all 4 wavelengths. (b) Detected signal of 4 wavelengths after propagating 1 km in SMF-28 fiber. Note that the wavelengths are now separated in time due to the dispersion of the SMF-28 fiber.

We have achieved 3 mode locked laser systems culminating with a 10-GHz erbium-doped fiber laser with 4 simultaneous and synchronous pulse outputs at different wavelengths. The pulses are near transform-limited between 11 ps and 14 ps in duration and 0.25-nm spectral width. There are no observable pulse dropouts. The well-defined frequency comb in the optical spectra as well as the high sideband suppression in the RF spectra indicate stable timing of the laser outputs and good supermode suppression. Better extinction ratio between wavelengths will improve the long-term stability of the laser by reducing the crosstalk between the different wavelengths.

REFERENCES

1. T. F. Carruthers and I. N. Duling, III, "10-GHz, 1.3-ps erbium fiber laser employing soliton pulse shortening," *Opt. Lett.*, vol. 21, pp. 1927-1929, Dec. 1996.
2. J. B. Schlager, S. Kawanishi, and M. Saruwatari, "Dual wavelength pulse generation using mode-locked erbium-doped fibre ring laser," *Electron. Lett.*, vol. 27, pp. 2072-2073, Oct. 1991.
3. S. Li and K. T. Chan, "A novel configuration for multiwavelength actively mode-locked fiber lasers using cascaded fiber bragg gratings," *IEEE Photon. Technol. Lett.*, vol. 11, pp. 179-181, Feb. 1999.
4. L. R. Chen, G. E. Town, P.-Y. Cortes, S. LaRochelle, and P. W. E. Smith, "Dual-wavelength actively mode-locked fibre laser with 0.7 nm wavelength spacing," *Electron. Lett.*, vol. 36, pp. 1921-1923, Nov. 2000.
5. G. E. Town, L. Chen, and P. W. E. Smith, "Dual wavelength modelocked fiber laser," *IEEE Photon. Technol. Lett.*, vol. 12, pp. 1459-1461, Nov. 2000.
6. J. Yao, J. Yao, Y. Wang, S. C. Tjin, Y. Zhou, Y. L. Lam, J. Liu, and C. Lu, "Active mode locking of tunable multi-wavelength fiber ring laser," *Opt. Commun.*, vol. 191, pp. 341-345, May 2001.
7. B. Bakhshi and P. A. Andrekson, "Dual-wavelength 10-GHz actively mode-locked erbium fiber laser," *IEEE Photon. Technol. Lett.*, vol. 11, pp. 1387-1389, Nov. 1999.
8. Z. Li, C. Lou, Y. Gao, and K. T. Chan, "A dual-wavelength and dual-repetition-rate actively mode-locked fiber ring laser," *Opt. Commun.*, vol. 185, pp. 381-385, Nov. 2000.
9. D. U. Noske, M. J. Guy, K. Rottwitt, R. Kashyap, and J. R. Taylor, "Dual-wavelength operation of a passively mode-locked "figure-of-eight" ytterbium-erbium fibre soliton laser," *Opt. Commun.*, vol. 108, pp. 297-301, Jun. 1994.
10. O. G. Okhotnikov and M. Guina, "Stable single- and dual-wavelength fiber laser mode locked and spectrum shaped by a Fabry-Perot saturable absorber," *Opt. Lett.*, vol. 25, pp. 1624-1626, Nov. 2000.
11. D. A. Pattison, P. N. Kean, J. W. D. Gray, I. Bennion, and N. J. Doran, "Actively modelocked dual-wavelength fiber laser with ultra-low inter-pulse-stream timing jitter," *IEEE Photon. Technol. Lett.*, vol. 12, pp. 1415-1417, Dec. 1995.
12. O. Deparis, R. Kiyan, E. Salik, D. Starodubov, J. Feinberg, O. Pottiez, P. Mégret, and M. Blondel, "Round-trip time and dispersion optimization in a dual-wavelength actively mode-locked Er-doped fiber laser including nonchirped fiber bragg gratings," *IEEE Photon. Technol. Lett.*, vol. 11, pp. 1238-1240, Oct. 1999.
13. T. R. Clark, T. F. Carruthers, P. J. Matthews, and I. N. Duling III, "Phase noise measurements of ultrastable 10GHz harmonically modelocked fibre laser," *Electron. Lett.*, vol. 35, pp. 720-721, Apr. 1999.
14. W. Ng, R. Stephens, D. Persechini, and K. V. Reddy, "Ultra-low jitter modelocking of Er-fibre laser at 10GHz and its application in photonic sampling for analogue-to-digital conversion," *Electron. Lett.*, vol. 37, pp. 113-115, Jan. 2001.
15. P. C. Becker, N. A. Olsson, and J. R. Simpson, *Erbium-Doped Fiber Amplifiers: Fundamentals and Technology*. New York, NY: Academic Press, 1999.
16. J. L. Zyskind, E. Desurvire, J. W. Sulhoff, and D. J. DiGiovanni, "Determination of homogeneous linewidth by spectral gain hole-burning in an erbium-doped fiber amplifier with GeO_2:SiO_2 core," *IEEE Photon. Technol. Lett.*, vol. 2, pp. 869-871, Dec. 1990.

C. Characterization of laser pulses via FROG

High-quality compression of optical pulses in fibers is important for many applications that rely on ultrashort pulses, including photonic ADC. Common compression techniques include soliton and fiber-grating compression, which can result in very high compression ratios, but generally require high input powers or generate pulses with broad wings unless pedestal suppression techniques are used [1]. Recently, many studies have examined the benefits and pitfalls of using axially-tailored fibers for pulse compression [2,3]. Experimentally, pulse compression has been observed in dispersion-decreasing fibers (DDF) in which the linear dispersion parameter, β_2, typically changes from about -10 ps^2/km to -1 ps^2/km [4]. DDFs need only low optical powers for clean compression, but long lengths of fiber (> 10km) may be required. A fundamental (N=1) soliton with a sech^2(T/T$_0$) intensity profile and peak power P_0 will adiabatically compress temporally in DDF by the ratio $W_{eff} = \beta_{input}/\beta_{output}$, which in practice is limited to about 10-20. These fibers exhibit rich dynamics when taken from the adiabatic limit, however. Pelusi and Liu [5] predicted that compression ratios greater than W_{eff} can be obtained with short sections of DDF for solitons of order N > 1 ($N^2 = \gamma P_0 T_0^2/|\beta_2|$). This would be advantageous for integration in optical communications equipment, which benefit from compact designs. Furthermore, simulations by Clarke *et al.* predicted interesting dynamics for pulses that passed through a zero dispersion point from the anomalous to normal dispersion regime [6], a situation that is experimentally realized by following DDF with normal dispersion fiber.

We present the first study of pulse compression in DDFs using frequency-resolved optical gating (FROG) [7]. These experimental studies use a 100m length of DDF, which is far less than that required for adiabatic compression, defined in Ref. 5 as $(L_d/\beta_2)(d\beta_2/dz) << 1$, where $L_d=T_0^2/|\beta_2|$ is the dispersion length. Dispersion of these nonadiabatically compressed pulses in either the normal or anomalous regime leads to pulse splitting, in excellent agreement with our numerical simulations of the nonlinear Schrodinger equation (NLSE). Even though these pulses can have clean temporal profiles, the spectral profiles may contain detailed structure. The quality of the compressed pulse is often characterized by the amount of energy in the pulse pedestal, defined as $(E_{tot} - E_{sech})/E_{tot}$, where E_{sech} is the energy of a pulse with a sech^2(T/T$_0$) intensity profile of the same peak power. Our results show that even in cases of low pedestal (< 5%), the temporal profile splits into multiple pulses that separate from one another following dispersion. Thus, these nonideal effects from nonadiabatic pulse compression must be considered in applications requiring pulses with high spectral and temporal quality. We have also followed the DDF with high dispersion (HD) fiber (β_2=85 ps^2/km) to observe the pulse splitting behavior predicted [6] for propagation across a zero dispersion point. Our studies also show high compression ratios (≈10) for N > 1 solitons as predicted [5].

Pulses centered at 1550 nm from an erbium-doped fiber laser [8] operating at a 960 MHz repetition rate are injected into 100m of DDF. This laser creates soliton-like pulses with $T_0 \approx 1$ ps. For these studies, we varied the pulse energies from 11 to 18 pJ. All pulses are characterized by a high-resolution multi-shot FROG apparatus employing Type II doubling in a 0.5-mm thick BBO crystal. The doubled light is passed into a 750 mm spectrometer with 0.02-nm resolution and detected by a 16-bit CCD camera. For the most complicated pulses with time-bandwidth products of 15-20, we typically achieve FROG errors of < 0.004 on 512 x 512 FROG traces, and all results are compared with spectra taken from an optical spectrum analyzer as an additional check.

Figure 1 shows a typical pulse from the sigma laser, the compressed pulse resulting from propagation through 100m of DDF (Fig. 1a), and finally, the same pulse after further propagation through 3.0 meters of HD fiber with β_2= 85 ps^2/km (Fig. 1b) or 12 meters of SMF-28 optical fiber with β_2= -18 ps^2/km (Fig. 1c). For the compressed pulse in Fig. 1a, with $T_0 \approx 210$ fs, these lengths correspond to about 5L_d. Propagation in the anomalous regime leads to a heavily modulated temporal profile, while propagation in the normal regime leads to a double humped structure with oscillations in the wings. Figs. 1b and 1c also show the excellent agreement with our numerical simulations, described below. This modulation is rapid enough that the pulse breakup is not seen in autocorrelation.

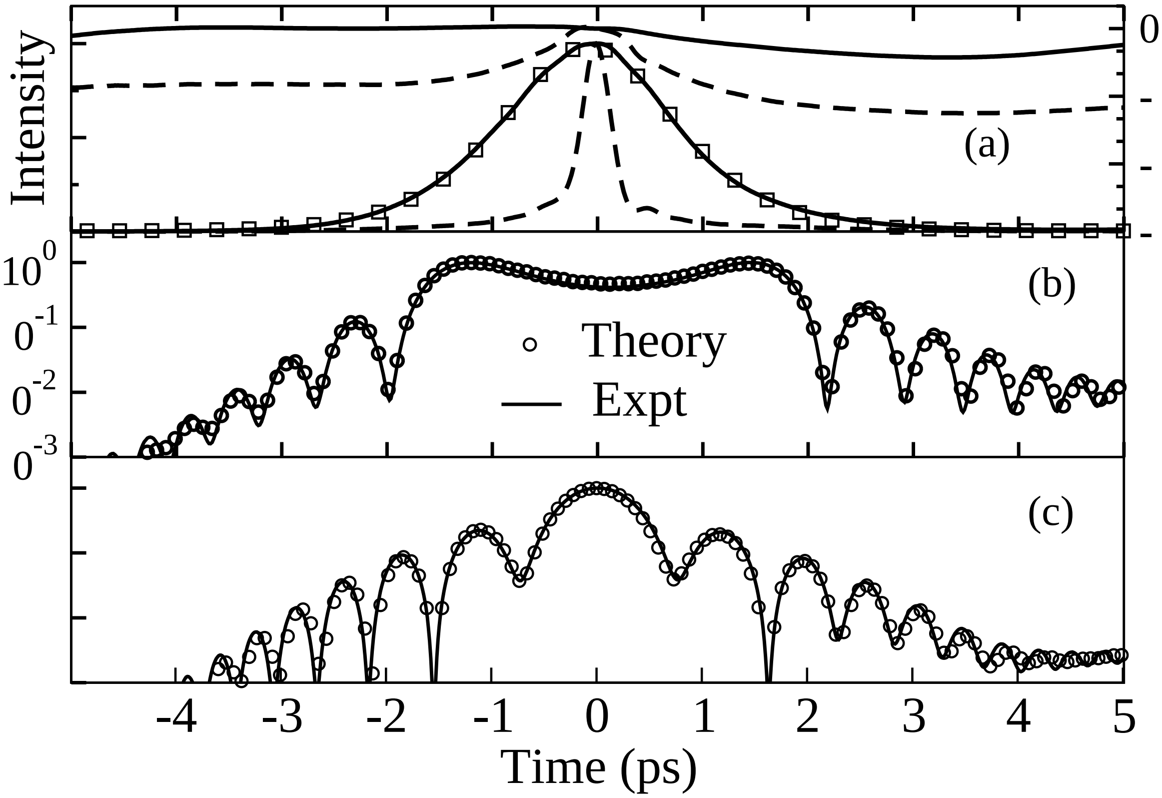

Figure 1—a) Output intensity and phase from sigma laser and from DDF (linear intensity scale). Sech^2(T/T$_0$) fit (squares) yields T_0 = 1.1 ps. Compressed pulse after propagation through b) 3.0m of HD fiber (β_2 = 85 ps^2/km) and c) 12m of SMF-28 fiber (β_2= -18 ps^2/km). The simulations in b) and c) are discussed in the text.

We have also characterized the pulses as a function of incident power to the DDF (Fig 2). As the input pulse energy to the DDF is raised from 11 pJ to 18 pJ, corresponding to soliton orders from N=1.2 to 1.5, the compression ratio increases from 2 to 8 at the expense of lower quality spectra. Although we have observed compression ratios nearing typical W_{eff} (≈10) values in this short length, we have not obtained markedly higher ratios as predicted in Ref. 5, primarily due to higher order effects in our DDF. At the highest powers, the pedestal energy reached 30%, and the spectra completely split into two distinct halves about the central frequency of the input pulse. Additionally, the compressed pulses also have a pronounced nonlinear phase profile. These nonideal effects lead to the pulse breakup and are numerically modeled below.

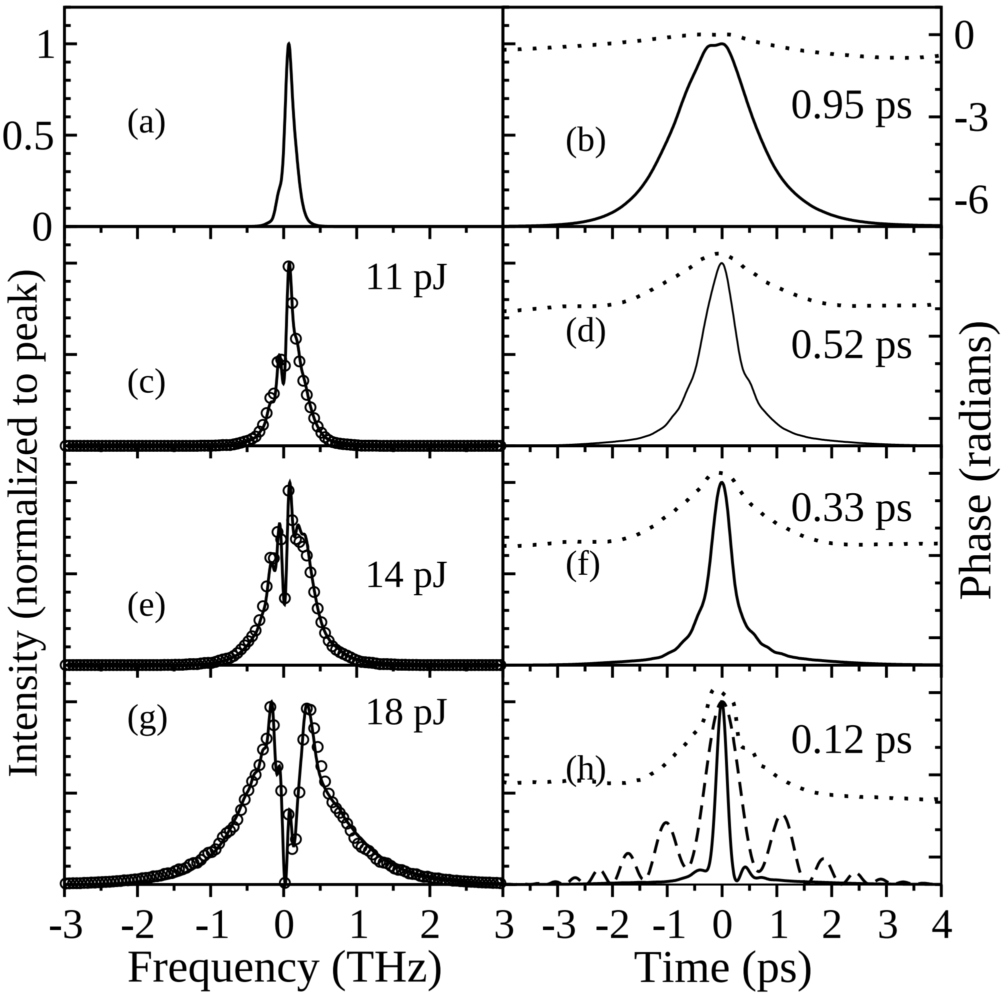

the signal laser pulse (top row), and of the compressed pulse for increasing pulse energies. Extracted values of T_0 from fits to $\mathrm{sech}^2(T/T_0)$ are indicated. (h) also shows the intensity profile of the compressed pulse after propagation through 12m of SMF-28. Results of numerical simulations (circles) shown for the spectra in c), e), and g).

Pulse propagation of an electric field envelope A(t) in DDF is described by the NLSE [1]:

$$\frac{\partial A}{\partial z} + \frac{\alpha}{2} A + \frac{i}{2}\beta_2(z)\frac{\partial^2 A}{\partial T^2} - \frac{1}{6}\beta_3\frac{\partial^3 A}{\partial T^3} = i\gamma|A|^2 A \qquad (1)$$

Here α is the fiber loss, β_3 is the third-order dispersion term, and γ is the nonlinear coefficient resulting in SPM, and we have neglected higher order effects. We have modeled the observed behavior by integrating the NLSE using the split-step Fourier method [1]. As shown in Figs. 1 and 2, the agreement between theory and experiment is very good. Unfortunately, we did not know the exact design parameters of the DDF, but given the input and output powers, our spectra and FROG traces, and assuming a linear taper to the dispersion, we obtained a set of realistic parameters for β_2, β_3, γ, and α that agree with our results quite well (see Fig. 2). These are α = 0.002/m, γ = 1.96/W-km, β_3 = 0.02ps^3/km, $\beta_2(0)$ = -11ps^2/km, and $\beta_2(L)$ = -1ps^2/km. At our highest input soliton order (N=1.6), the simulations actually yield similar compression ratios for $\beta_2(L)$ from 0 to -1.5 ps^2/km, giving a wide range of W_{eff}. Although this would affect the compression ratio for higher input powers than we reached, the only effect of different $\beta_2(L)$ through our power range was in the detailed structure of the spectrum. For the starting pulse of all simulations, we used the characterized output pulse of the sigma laser.

We have also modeled the pulse breakup as a function of propagation distance in normal and anomalous dispersion fibers for an N=1.69 soliton injected into 100m of DDF (neglecting α and β_3, with $\beta_2(0) = -10ps^2/km$ and $\beta_2(L) = -1\ ps^2/km$). Figure 3 shows the output of this pulse from the DDF, and from dispersive fibers of increasing length. The pulse breakup is clearly visible after propagating $5L_d$, and after $10L_d$, the pulses are heavily modulated well into the wings. Ultimately, the temporal profile will stretch to resemble the spectral profile, but for these intermediate lengths where interference effects dominate, this interesting evolution unfolds.

The different propagation behaviors from positive and negative dispersion can be understood by examining the temporal phase profile and spectrum of the nonadiabatically compressed pulse at the output of the DDF. In Fig. 3b, we can see that the $\Delta\omega > 0$ components arrive during the last half of the pulse, while the $\Delta\omega < 0$ arrive during the first half. However, because the $\Delta\omega > 0$ components travel faster than the $\Delta\omega < 0$ in the anomalous regime ($\beta_2 < 0$), the two halves of the frequency spectrum must eventually sweep past each other in time. As the pulse propagates, different frequency components overlap temporally, generating oscillations across the entire profile. In the normal regime, the opposite occurs, and the components arriving near T = 0 begin to move farther apart in time as the pulse propagates. However, in the wings of the pulse where the magnitude of $\Delta\omega$ decreases, the components will overlap temporally as the highest frequency components (maximum of Fig. 3b) ultimately arrive last and the lowest frequency components (minimum of Fig. 3b) arrive first.

This behavior is clearly the result of nonadiabatic pulse compression and suggests that a closer look at the pulse compression with varying degrees of adiabaticity is in order. Fig. 4 shows simulations of ideal soliton pulses passing through varying lengths of DDF, with $\beta_2(0) = -10ps^2/km$ and $\beta_2(L) = -1ps^2/km$ after dispersion in the anomalous regime through 13 L_d. The lengths of DDF range from 1 L_d^{ddf} to 128 L_d^{ddf}, where L_d^{ddf} is the input dispersion length. The adiabaticity criterion, $(L_d/\beta_2)(d\beta_2/dz) << 1$, is met across the entire DDF for Fig. 4a. The peak powers of the pulses have been adjusted for constant compression ratio, and we have neglected α and β_3. Even when the pedestal energy is less than 2%, as in Fig 4b, the spectrum is split and we see temporal ripple following dispersion. The nonadiabatic compression process is clearly dominated by self-phase modulation (SPM): SPM also leads to spectral splitting and broadening, and in constant dispersion fibers imparts a nonlinear temporal phase profile that is proportional to the intensity, similar to those found in Figs. 2 and 3b. The negative dispersion of the DDF flattens the phase profile as the DDF propagation length increases, but cannot compensate for the SPM contribution with short lengths.

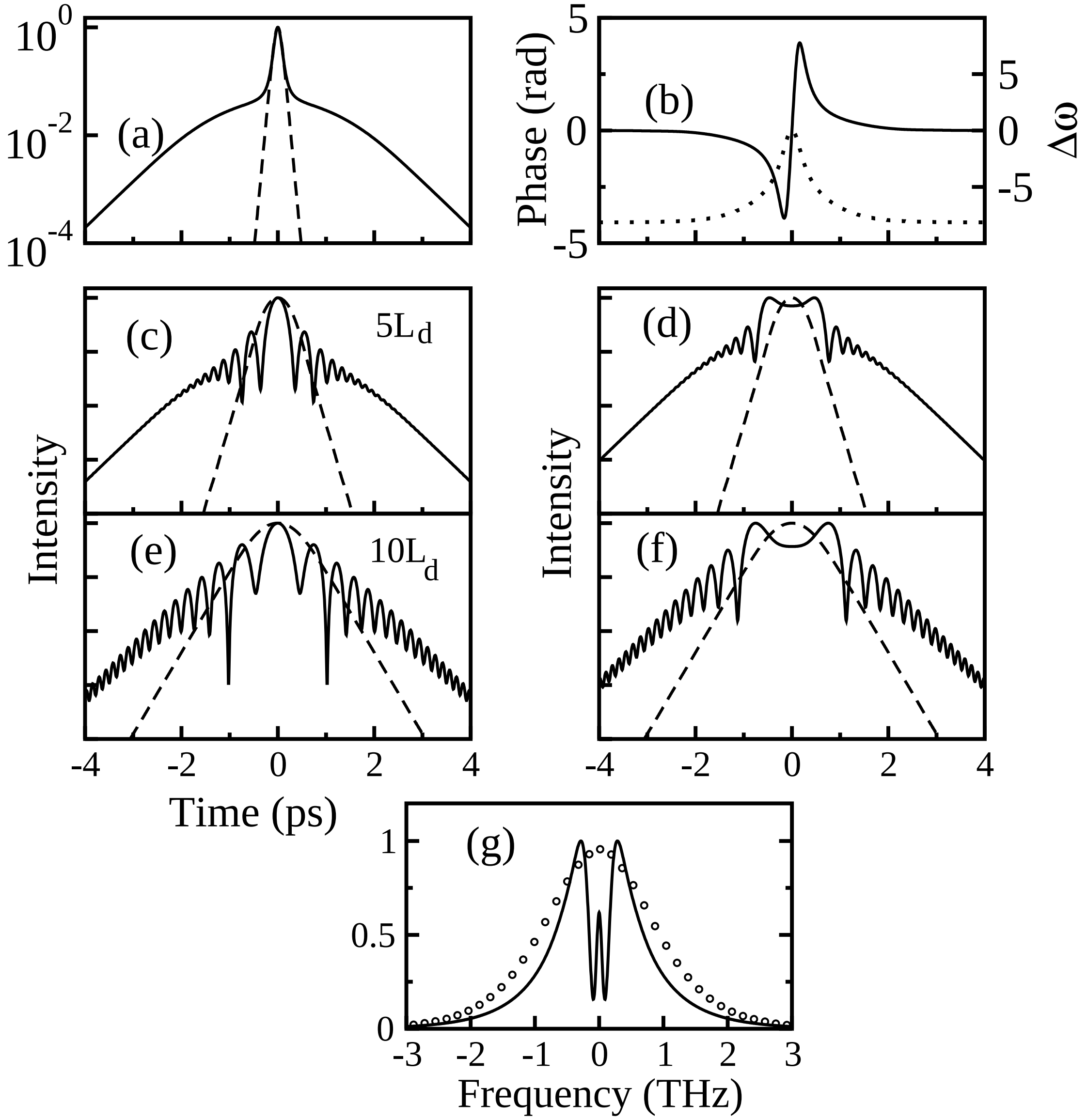

Figure 3—Numerical simulations. a) Intensity (solid line) of an N = 1.69 pulse compressed in 100m of DDF. Intensity of ideal sech^2 pulse (dashed line). b) Phase (dotted line) and frequency shift across the compressed pulse, $\Delta\omega = -d\phi(t)/dt$. Intensity of the compressed pulse after propagation through 5L$_d$ and 10L$_d$ in the c), e) anomalous and d), f) normal regime. The dashed line shows the evolution of the ideal sech^2 pulse. g) Spectrum of the compressed pulse (solid line) and the sech^2 pulse (circles).

We have evaluated experimentally and theoretically some aspects of pulse compression in DDF that need consideration when stepping beyond the adiabatic limits, especially in applications where high spectral and temporal quality need to be preserved. Using FROG, we have also verified experimentally the structures formed when pulses are propagated from the anomalous to normal dispersion regime, and observed an interesting breakup of the compressed pulses. The results also show a high compression ratio nearing typical adiabatic limits. Rapid characterization of fiber-compressed pulses combined with numerical simulations will aid in tailoring the input pulses for the highest quality compression, and complete characterization of pulsed lasers continues to illuminate the interesting dynamics that are hidden behind autocorrelations and spectra.

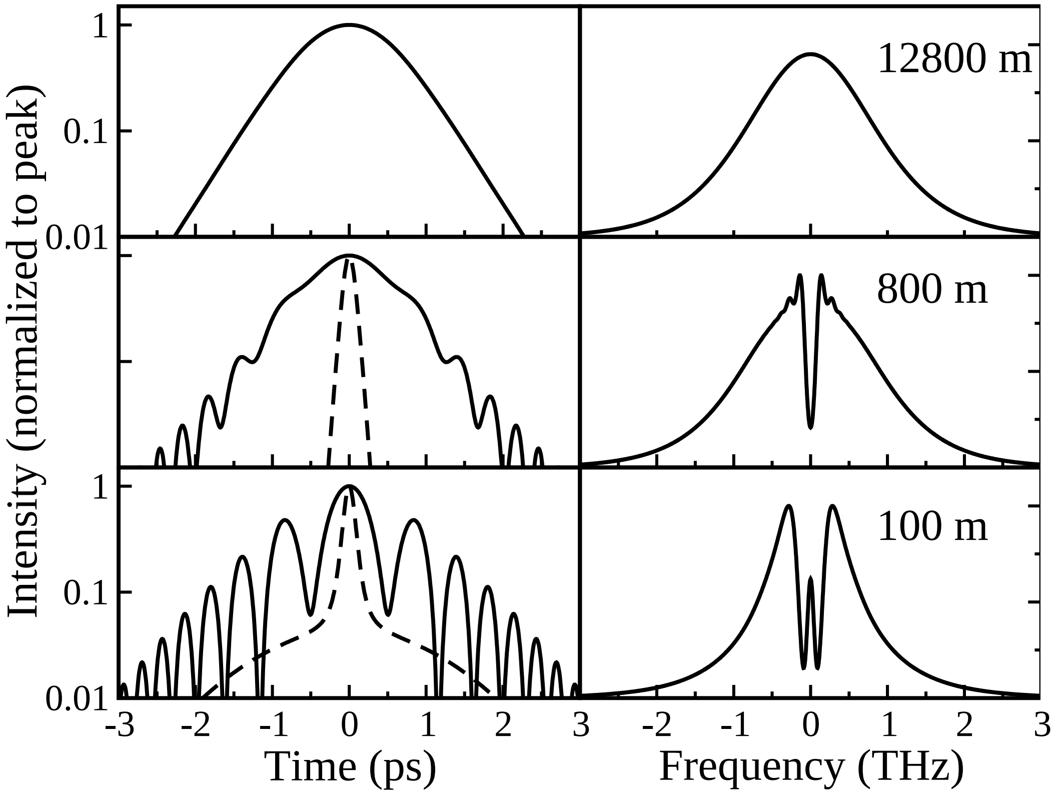

Figure 4—Simulation of compressed pulse propagation through $13L_d$ with compression in different lengths of DDF. L_d^{ddf} is 100 m. Pedestal amounts are a) 0.01%, c) 1.7%, and e) 37%. Right column shows the corresponding spectra (linear scale). Dashed lines in c) and e) are the initial intensity profiles of the compressed pulses.

REFERENCES:

1. G. P. Agrawal, *Nonlinear Fiber Optics* (Academic, San Diego, California, 1995)
2. K.T. Chan and W. H. Cao, Opt. Comm., **184**, 463 (2000)
3. A. Mostofi, H. Hatami-Hanza, and P. L. Chu, IEEE J. Quant. Electron. **33**, 620 (1997)
4. S. V. Chernikov, E. M. Dianov, D. J. Richardson, and D. N. Payne, Opt. Lett. **18**, 476 (1993)
5. M. D. Pelusi and H. F. Liu, IEEE J. Quant. Electron. **33**, 1430 (1997)
6. S. R. Clarke, J. Clutterbuck, R. H. J. Grimshaw, and B. A. Malomed, Phys. Lett. A., **262**, 434 (1999)
7. R. Trebino and D. Kane, J. Opt. Soc. Am. A, **10**, 1101 (1993)
8. T. F. Carruthers and I. N. Duling III, Opt. Lett. **21**, 1927 (1996)

VI. Northrop-Grumman optoelectronic switch characterization

NRL contributed to the program a highly-parallel, photonic ADC as well as participating in a four-way collaborative research effort whose members included: Northrop Grumman, Rockwell, the University of Maryland, and the Naval Research Laboratory. As part of the collaboration, NRL used an actively mode-locked fiber laser and microwave probe station to analyze the optoelectronic switches and microwave circuitry for the Photonic ADC system led by Northrop Grumman.

To meet these goals, the NRL sigma laser received its input from a Northrop Grumman microwave source at 960 MHz. The amplitude and phase noise results are shown below in Fig. 1. Here the amplitude noise is <0.03 % and the timing jitter is <64 fs (over a 100-Hz to 10-MHz integration range) as compared to the Northrop-Grumman source which has <20-fs timing jitter over the same range.

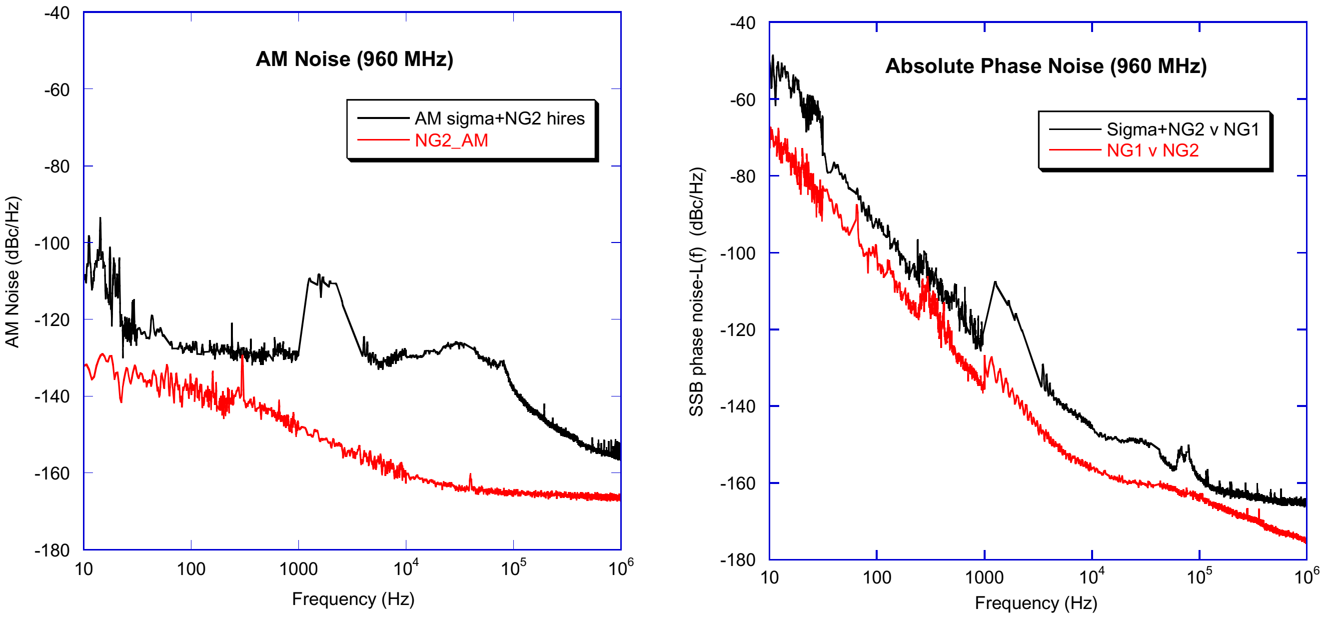

Figure 1—Amplitude and Phase noise plots of the sigma laser driven by a 960-MHz Northrop-Grumman signal source.

The laser output is needed to switch a metal-semiconductor-metal (MSM) GaAs photoconductive switch fabricated by the University of Maryland (UMD). The laser output at ~1550 nm is below the bandgap for GaAs and therefore the material is transparent to this light. The laser output, therefore, was transformed to nominally 780 nm via second harmonic generation to excite the UMD photoconductive switches. Figure 2 shows the process of second harmonic generation for conversion of the sigma laser's output using periodically-poled, lithium niobate (PPLN) with a 19-µm poling period to transform the 1560-nm optical pulse train into 780-nm pulses.

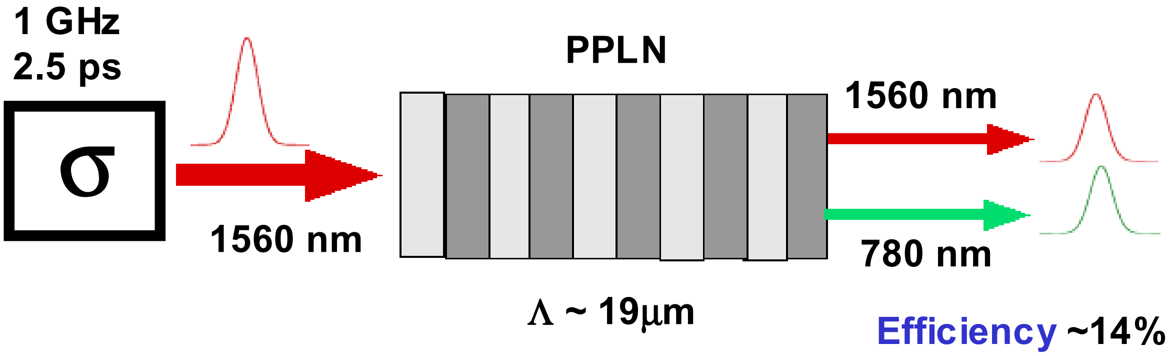

Figure 2—Second harmonic generation of the sigma laser's output using PPLN.

The SHG light was amplified to achieve 350-pJ pulses at 777 nm from the 960-MHz Sigma laser. The laser was coupled to the University of Maryland's GaAs metal-semiconductor-metal (MSM) photodiode through a microscope objective as shown in Figure 3. NRL's optical/microwave circuit probing station characterized the response of the UMD MSM photodetectors. The measured electrical signal response with a 5-Volt applied bias achieved an electrical pulse with a 17-ps rise time, 60-mS peak conductance, and a 5-mS static offset as shown in Figure 4. The switch was integrated into the Northrop Grumman microwave circuit and re-tested. The integrated switch achieved the 960-MHz repetition rate desired for the NRL portion of the project.

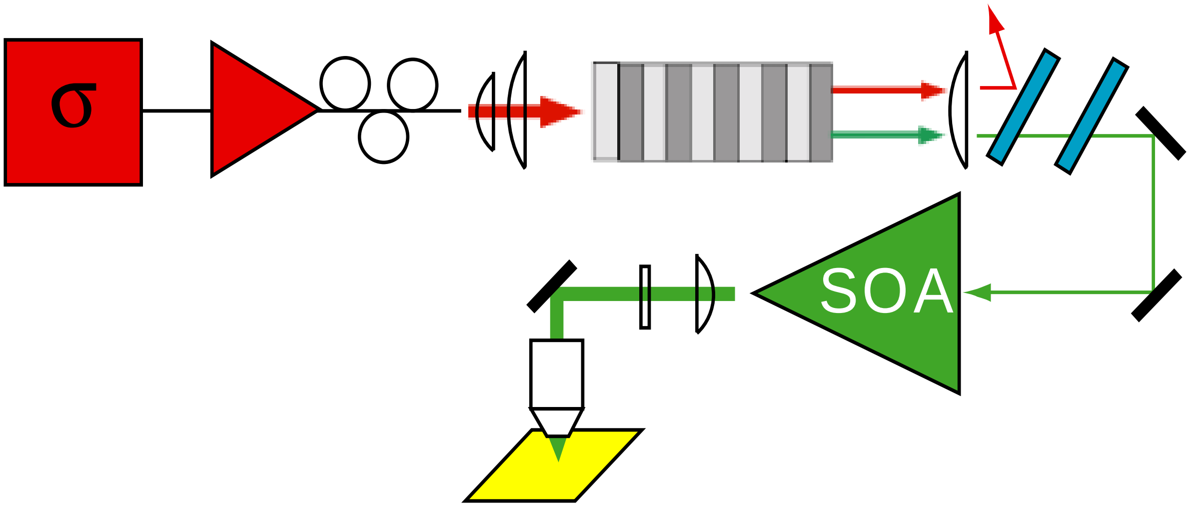

Figure 3—NRL setup for characterizing the UMD MSM photodetectors. The Sigma laser is driven by a Northrop-Grumman RF source, frequency doubled in PPLN to ~780 nm, amplified and focused onto the UMD switch, and analyzed on NRL's optical/microwave circuit probing station.

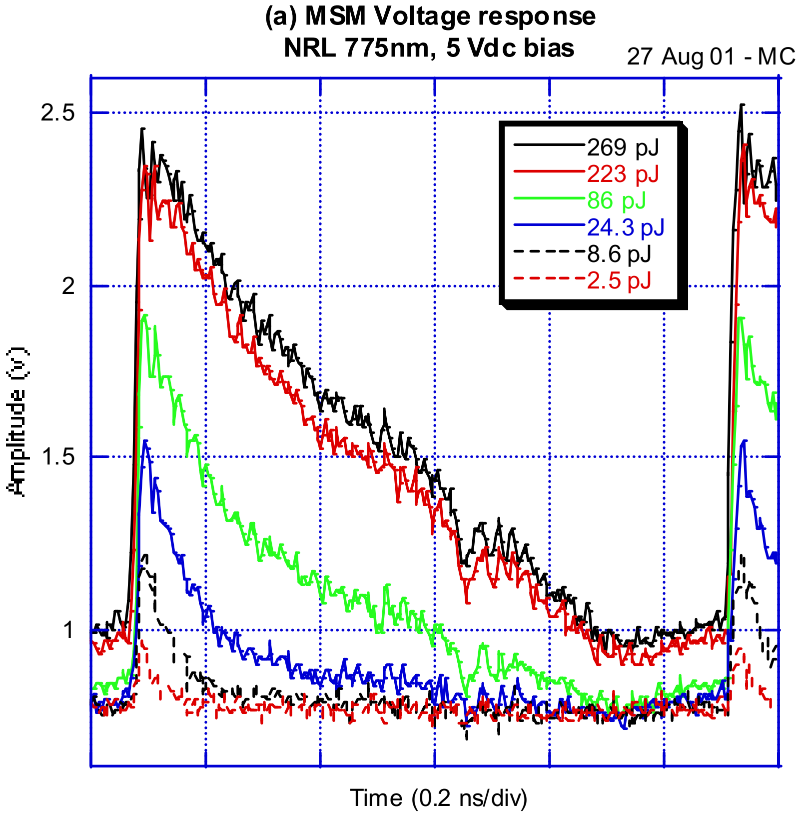

(a) MSM Voltage response
NRL 775nm, 5 Vdc bias

27 Aug 01 - MC

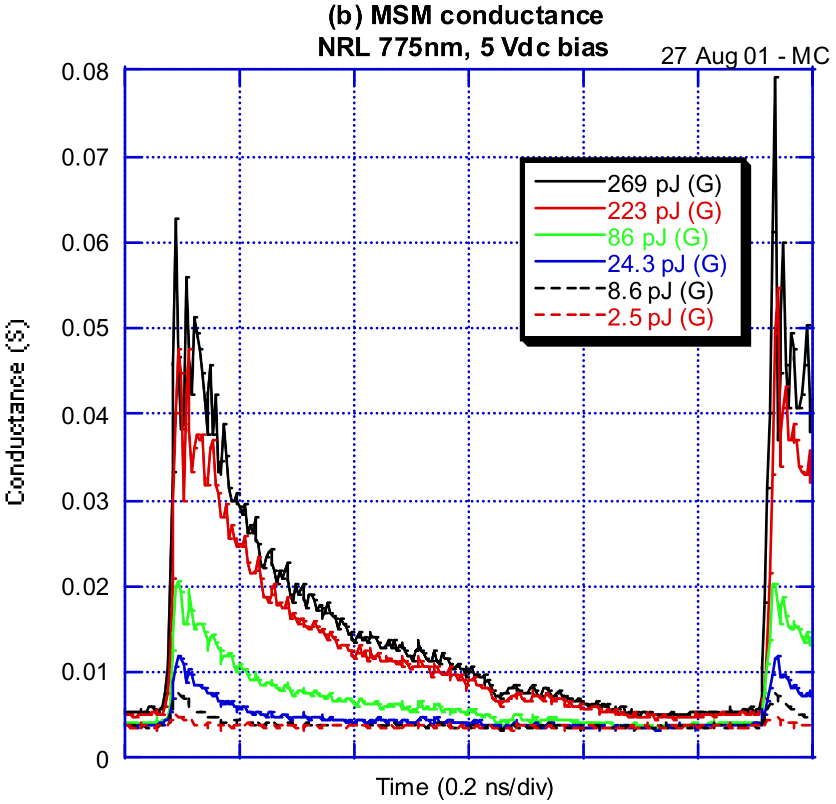

(b) MSM conductance
NRL 775nm, 5 Vdc bias

27 Aug 01 - MC

Figure 4—NRL optical/microwave circuit probing station characterizes the UMD MSM photodetectors (a) voltage response and (b) conductance as a function of pulse energies from the amplified SHG output of the NRL sigma laser.

VII. Highly parallel photonic analog-digital converter

A. Clock independent design

Current photonic technology offers many attractive features including high bandwidth capability (DC–80 GHz), reduced size and weight of components, nearly lossless signal remoting, and reduced front-end components and power requirements on receiver systems. We experimentally demonstrate the performance of a high bandwidth photonic sampler and highly parallel ADC architecture based on discrete time domain to wavelength domain mapping utilizing commercially available technology. This technique utilizes an optical clock for sampling a microwave signal. The optically signal is first multiplexed, the microwave signal is encoded, and then the optical signal is finally demultiplexed. The sampling clock rate of this process is controlled by the laser repetition rate, and is therefore independent of the system concept.

A hybrid optoelectronic ADC architecture with a photonic sampler based on the time interweaving of spectrally distinct pulses is shown in Figure 1. Spectrally broad pulses from a mode-locked laser are sliced by a wavelength division multiplexer (WDM) into N wavelength discrete channels. Connected to each channel is a fiber stretcher (FS), variable attenuator (AT), fiber delay loop (DL) and Faraday mirror (FM). Dispersion shifted fiber is used to reduce the pulse broadening and relative dispersion between the channels. The Faraday mirror provides polarization compensation for the non-polarization maintaining components of each channel system as well as a second pass through the WDM. The length of each channel's propagation loop is chosen to discretely fill the interpulse period of the original pulse train and the fiber stretcher provides temporal fine-tuning. The variable attenuators allow the compensation of the input pulse spectrum to provide equal optical power in each channel. After amplification to the

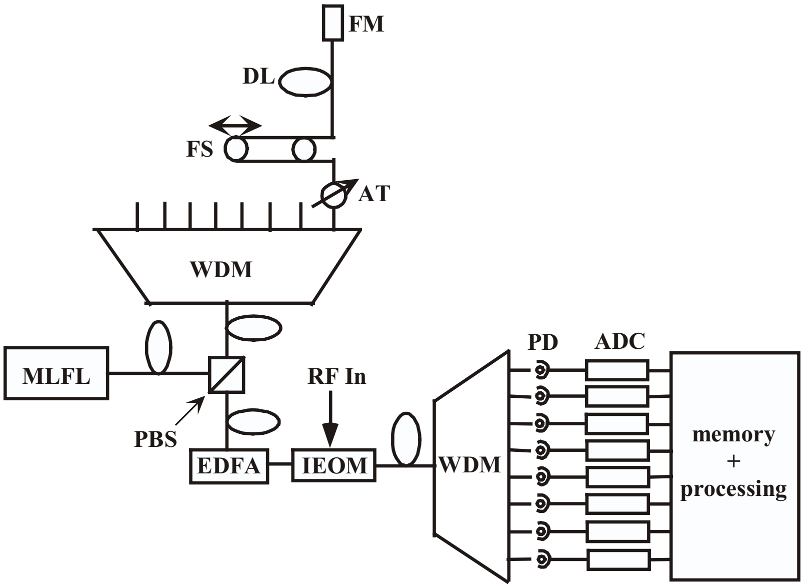

Figure 1—Photonic ADC system.

desired optical power per channel, a $LiNbO_3$ integrated electro-optic modulator amplitude modulates the pulse train with the signal to be digitized. The back-end digitization portion of the system utilizes a second WDM to demultiplex the time- and wavelength-interleaved pulse train for parallel digitization by the use of photodetectors (PD) and electronic ADCs. The digitization of each channel occurs at a rate which is N times slower than the photonic ADC sampling rate, thus significantly reducing the requirements on the bandwidth of the back-end electronic components.

The fundamental limitation on the bandwidth, Δf_{ADC}, of the described ADC system is due to RF modulation induced spectral broadening causing cross-talk between adjacent channels and/or loss of modulation information after the demultiplexing channel passband. The system sampling rate for a WDM with N channels and a laser with repetition rate R_{laser} is given by $f_s = R_{laser} N$. Assuming Nyquist sampling $f_s = 2 \cdot \Delta f_{ADC}$, the constraint on the number of WDM channels and the demultiplexing passband, $\delta\lambda_{ch}$, can be shown to be

$$\left(\frac{\delta\lambda_{ch}}{N} \right)_{WDM} > \frac{\lambda_0^2 R_{laser}}{c} , \tag{1}$$

where c is the speed of light in vacuum and λ_0 is the laser wavelength. An additional constraint on the number of WDM channels results from the laser bandwidth where $\Delta\lambda_{laser} > N\delta\lambda_{ch}$. Current commercially available dense WDM technology (200 GHz channel spacing, and up to 32 channels with 1 nm passband) would allow a 1.5µm laser with 50-nm bandwidth and 4 GHz repetition rate to operate with a sampling rate of over 120 GSPS. These numbers indicate the great potential for the method and show that the current WDM and laser technology are not the limiting factors for the bandwidth of such an ADC system. In practice, the bandwidth of the photonic ADC is limited by the electro-optic modulator technology to ~40 GHz.

There are several advantages to photonic sampling with this method. By forming a distinct pulse for each channel's spectral region, there is no degeneracy in the wavelength-time mapping. This is in contrast to what occurs in the overlapping leading/trailing edges of two temporally adjacent continuously chirped optical pulses. The interpulse period of the mode-locked laser is also easily filled in a compact manner and is adaptable to any laser repetition rate by adjustment of the fiber delay loop lengths providing real-time optical sampling. In addition, amplification of the wavelength-interleaved pulse train and using a matching WDM channel spacing for demultiplexing allows signal sampling with the maximum optical power per channel by not wasting power on spectral regions that will not be used in the digitization.

B. 10-GSPS, 8-channel, 7-bit converter

We constructed an eight-channel optical pulse train sampler and performed preliminary testing of its use in a photonic ADC system. The time- and wavelength-interleaved pulse train was formed by slicing the mode-locked pulses of a stretched pulse fiber laser (τ_p~1 ps, $\Delta\lambda$~50 nm and 40 MHz repetition rate) with an eight channel WDM which had a ~1 nm passband and ~3 nm channel separation. Figure 2(a) shows the spectrum of the sampler output after amplification by a two pass erbium-doped fiber amplifier (EDFA) with the sampler input spectrum overlayed. Note that the variable attenuators of each channel have compensated for the input pulse and amplifier spectral variations. An 18-GHz $LiNbO_3$ electro-optic modulator was used to modulate the sampling pulse train with the RF signals to be digitized. The measured optical power per channel transmitted through the modulator was ~1mW. Both a slow real-time sampler (320 MSPS with infinite aperture time) and a high frequency sampler (10 GSPS with 700 ps aperture time) were constructed and tested. Shown in Fig. 2(b) and (c) are the real-time and high frequency sampler pulse trains constructed by adjusting the fiber delay loops to meet the 3 ns and 100 ps respective pulse separation requirements.

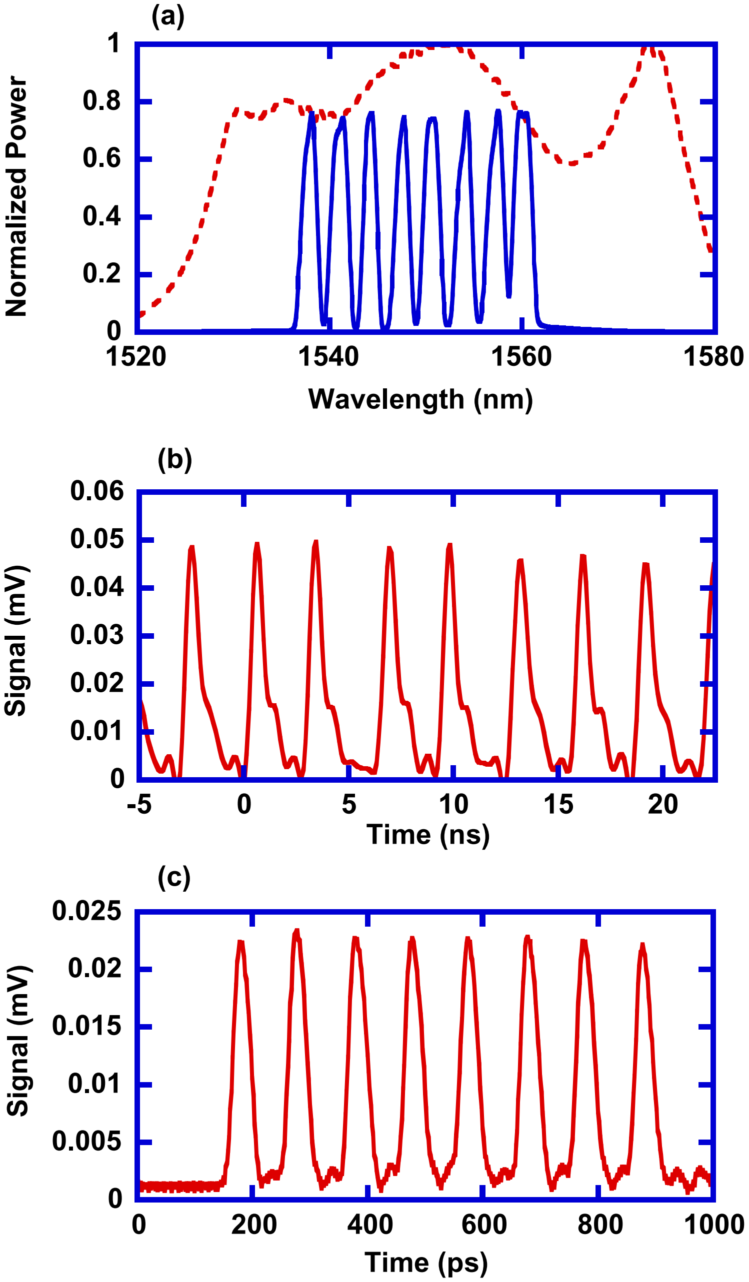

Figure 2—(a) Spectrum of photonic sampler input (dashed line) and eight channel sampler output. Pulse train of sampler with (b) 320 MSPS and (c) 10 GSPS sampling rates.

In order to demonstrate the use of the sampler in an ADC system, equivalent-time digitization of synchronous signals was performed using an optical spectrum analyzer, with its internal scanning grating, photodetector and electronic ADC simulating the back-end digitization. Note that the digitization resulting from this test is the result of integrating many waveforms due to the slow scan rate of the optical spectrum analyzer. A portion of the laser output was split off before entering the sampler system and sent to a 20 GHz photodetector. Bandpass filtering of the electrical photodiode signal then provided synchronous sinusoidal signals for digitization testing. Figure 3 shows the agreement of the eight-channel, 10-GSPS digitization with the averaged 20 dBm, 1.2-GHz input signal measured on a sampling scope. The agreement accuracy for this measurement is estimated to be ~5 bits using deviation from the reference waveform and is limited by a combination of the OSA resolution, sampler resolution and input waveform noise. For this experiment, a bandpass filter with center frequency of 1.2 GHz selected the 30th harmonic of the laser frequency from the photodiode signal and the effective pulse train chirp rate of approximately 0.03 nm/ps was used to reconstruct the sampled signal.

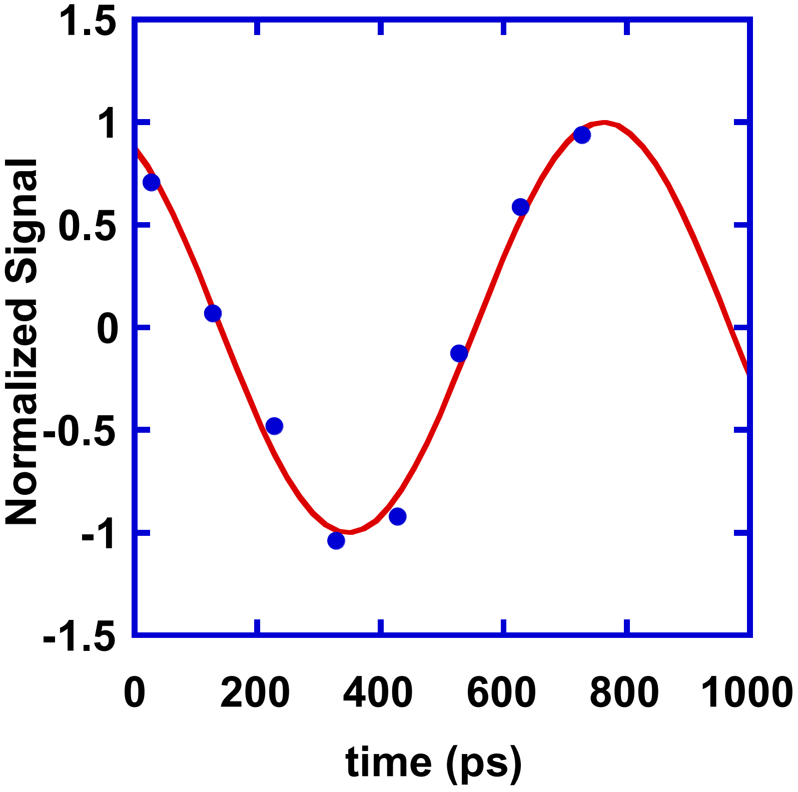

Figure 3—Comparison of input 1.2-GHz sinusoidal signal (solid curve) and eight channel digitization (filled circles).

Single channel testing of the system was performed to quantitatively evaluate the effective number of bits of the photonic sampler at high frequency. Single tone asynchronous microwave signals of varying frequency (2 to 18 GHz) were amplified by a high frequency amplifier (P_{max} = 27 dBm) and applied to the $LiNbO_3$ modulator. The timing jitter of the laser was not included in this test due to the asynchronous nature of the driving signal. A 20 GHz photodetector and a low-noise sampling head were used to measure the maximum signal level at each frequency when the EO modulator was biased at quadrature. The rms noise floor of the detector-sampling head system was measured to be <350μV which with the ~300 mV full scale pulse amplitude set the maximum possible signal to noise ratio measurement at ~58dB. The minimum measurement time for this experiment was set by the sampling scope persistence time of 1 second. The potential effective number of bits of the sampler was deduced from the measured signal to noise ratio for each frequency using the expression $N_{eff} = \log_2(A_{md}/A_n)$, where A_{md} is the modulation voltage range and A_n is the rms noise voltage. Figure 4 shows the measured effective number of bits of the system with increasing frequency for ~25dBm RF input power. The drop in effective number of bits above 12 GHz is due to the increase in the applied V_π of the modulator with frequency resulting in a reduced modulation signal level and the response of the sampling head which had a bandwidth of 12.5 GHz. The measured system noise level of ~0.8mV for an unmodulated pulse amplitude of ~150mV is consistent with the independently measured RIN (<1%) of the mode-locked fiber laser output in its current configuration. This indicates that the RIN is not significantly degraded by the photonic sampling architecture demonstrated here and the effective number of bits can be significantly improved with the use of a lower RIN laser. In addition, the bandwidth can be improved with the use of a lower V_π and higher bandwidth modulator.

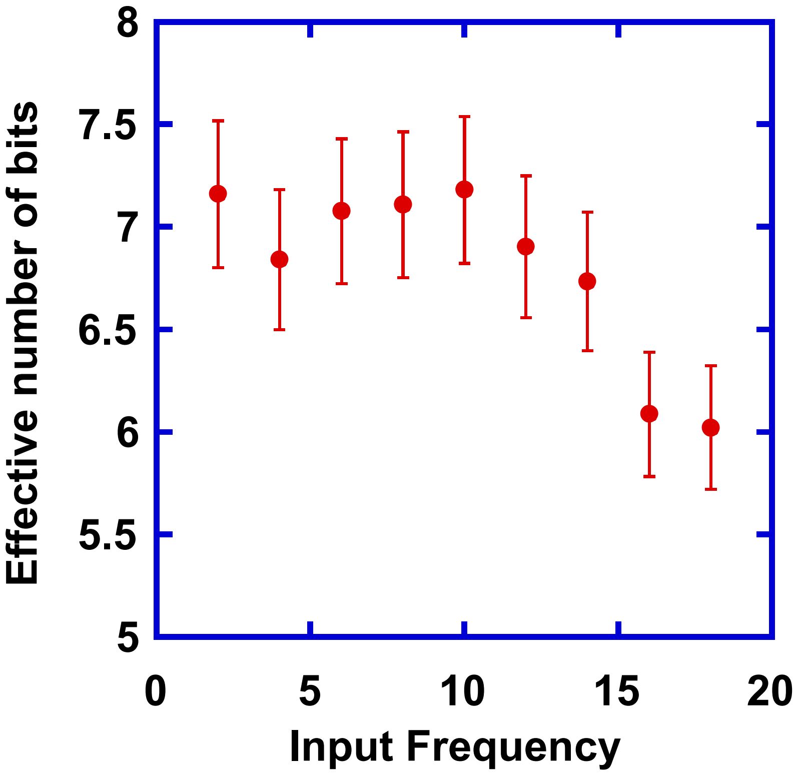

Figure 4—Effective number of bits as a function of modulator input frequency.

C. 2.5-GSPS, 2-channel, 5-bit converter

A real-time two-channel photonic analog-digital converter operating at 2.5 GSPS has been constructed and demonstrated. The two channel parallel ADC architecture with a photonic sampler based on the time interleaving of spectrally distinct pulses is shown in Figure 5. A harmonically mode-locked sigma laser externally driven by a low noise synthesizer produces transform limited 2-ps pulses (sech^2 shape) at a repetition rate of 1.25 GHz with 2-mW average power. The pulse train is amplified with an erbium–doped fiber amplifier (EDFA) to ~15 mW and directed to 1 km of dispersion decreasing fiber (DDF) resulting in supercontinuum generation with a 10 dB width of ~60 nm in a 250 fs duration pulse. Figure 6(a) shows the output spectrum of the DDF. The spectrally broad pulses are sliced by a wavelength division multiplexer (WDM) into 8 discrete wavelength channels separated by 3 nm each with a 3dB width of 1 nm. Two of these channels are used in the current experiments. Connected to each channel is a fiber stretcher (FS), variable in-line optical attenuator (AT), fiber delay line (DL) and Faraday mirror (FM). Dispersion shifted fiber is used to reduce the pulse broadening and relative dispersion between the channels. The Faraday mirror provides polarization compensation for the non-polarization maintaining components of each channel system as well as a second pass through the WDM to multiplex the two channels to the same fiber. The length of the channels' propagation loop is chosen to discretely fill the interpulse period of the original pulse train. The fiber stretcher provides temporal fine-tuning with a total tuning range of ~200 ps and temporal resolution of 0.5 ps. The variable attenuators allow for compensation of the input pulse spectrum, providing equal optical power in each channel. A polarization maintaining EDFA amplifies the two-wavelength pulse train. Figure 6(b) shows the pulse train spectrum after amplification by the EDFA. A $LiNbO_3$ Mach-Zehnder modulator amplitude modulates the pulse train with the signal to be digitized. The modulated time- and wavelength-interleaved pulse train signal is demultiplexed by a second WDM for the parallel digitization of the two channels. The

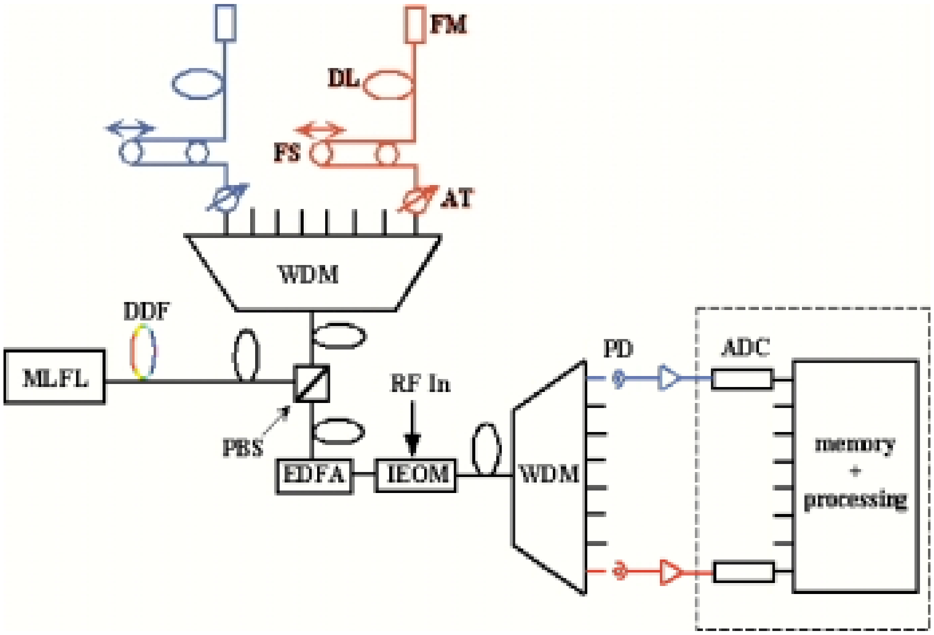

Figure 5—Two-channel photonic ADC

pulse train for each channel was directed to a 1.5 GHz photodetector. The resultant sinusoidal signal representing the channel pulse train was amplified by a low noise RF amplifier and directed to a high speed real-time digitizing oscilloscope employing a single 8-bit 4 GSPS electronic ADC for each channel.

Two major limiting factors in the performance of an analog-digital converter are uncertainty in the sampling time of the input signal and uncertainty in the sampled amplitude. The effect of timing error on the ADC system resolution can be estimated by considering the worst case of digitizing a sinusoidal signal at the zero crossing with a frequency equal to the system bandwidth limit. The maximum effective number of bits can be shown to be

$$N_\tau = \log_2\left\{(\pi f_{\max}\tau)^{-1}\right\}$$

where τ is the timing error. The effect of uncertainty in the sampled amplitude can be estimated from the expression

$$N_A = \log_2\left(\frac{A}{\delta A}\right)$$

where A is the full-scale signal amplitude and δA is the amplitude error.

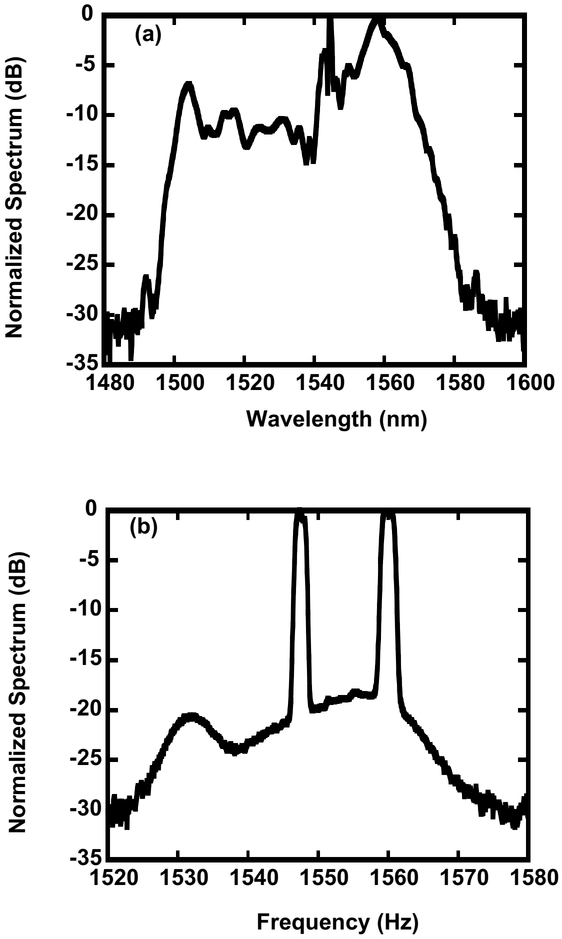

Figure 6—(a) DDF output spectrum (10 dB width of 60 nm) (b) Two-channel output of photonic sampler.

In our system, the amplitude noise and timing jitter of the laser are expected to be important in the ultimate resolution of the system. The timing jitter for the laser source, calculated from the phase noise data, over a frequency range of 100 Hz to 1 MHz (equivalent measurement time of ~1.5 ms) is 95 fs for a 1 GHz repetition rate. For the 2.4 GSPS ADC of this paper, this would correspond to a maximum resolution at the Nyquist frequency of 11.5 bits. The pulse amplitude to rms amplitude noise ratio was measured using a low barrier Schottky diode and DC blocking filter as an amplitude modulation detector over the same measurement time to be 32 dB corresponding to 10.6 bits.

Real-time single tone digitization was performed to test the ADC system. A sinusoidal signal from an RF synthesizer with an output power of 20 dBm was applied to the input of the electro-optic modulator shown in Figure 5. The modulated 1.25-GHz pulse trains of each channel after the second WDM were digitized simultaneously and saved for processing. The input waveform was then reconstructed from peak-amplitudes of the digitized pulses using the known wavelength-time mapping. Figure 7 shows the digitized data points overlaid on the input 900-MHz waveform. Note that a single channel of the photonic ADC does not satisfy the Nyquist requirement of $f_s>2f$ for $f>612.5$ MHz. The accuracy of this measurement is estimated to be ~5% from the measured deviation from the reference waveform. This is consistent with the electronic ADC resolution of ~4 bits as measured by digitizing an input sinusoidal signal of similar amplitude and frequency (~60 mV p-p at 1.25 GHz) to the photodetector signals.

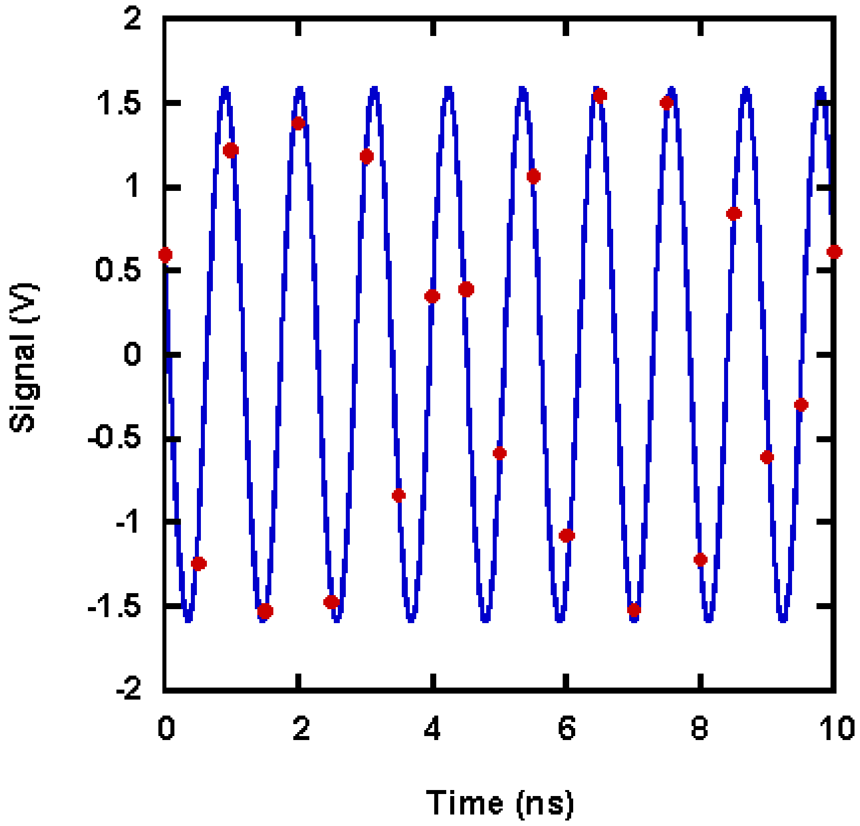

Figure 7—Real-time digitization of 900 MHz input signal.

D. 30-GSPS, 3-channel, ~2-bit converter

Upon realizing future photonic ADCs would be based upon even faster electronic ADCs, a third system was constructed by synchronizing our photonic subsystem with LeCroy Corporation's 10-GSPS electronic converters in their Wavemaster line of oscilloscopes. This allowed us to realize a 30-GSPS system. When digitizing an 11.4-GHz microwave signal we realized 29.25-dB spur-free dynamic range commensurate with greater than 4.5 ENOB, the limit of the electronic ADC.

We constructed a real-time three-channel photonic analog-digital converter operating at 30 GSPS. As before, the three channel photonic ADC architecture was based on the time interleaving of spectrally distinct pulses shown previously. A harmonically mode-locked sigma laser externally driven by a low noise synthesizer produces transform limited 1.2-ps pulses at a repetition rate of 10 GHz with 8-mW average power. The pulse train is amplified with an EDFA and directed to ~1 km of DDF resulting in supercontinuum generation with >20 nm of optical bandwidth. The spectrally broad pulses are sliced by a WDM into 3 discrete wavelength channels. A $LiNbO_3$ Mach-Zehnder modulator amplitude modulates the pulse train with the 11.4-GHz microwave signal to be digitized. The modulated time- and wavelength-interleaved pulse train signal is demultiplexed by a second WDM for the parallel digitization of the three channels. The optical pulse train for each channel was directed to a 20-GHz Discovery Semiconductor photodetector. The resultant signal representing the channel pulse train was amplified by a low noise RF amplifier and directed to a LeCroy Wavemaster 8500, a real-time digitizing oscilloscope with 4 inputs each employing a 10-GSPS ADC with a 5-GHz analog input bandwidth.

The 100-MHz reference oscillator for the LeCroy oscilloscope was synchronized with the 10-GHz Sigma laser through an HP reference oscillator with 100-MHz and 10-MHz synchronized sources. The 100-MHz source was connected to the LeCroy oscilloscope, while the 10-MHz source was connected to a Wiltron source providing the 10-GHz signal to the Sigma laser. This allowed for synchronized sampling and detection of the 11.4-GHz microwave signal. Figure 8 shows the digitized 11.4-GHz output signal from the 3-channel interleaved data of the 30-GSPS photonic ADC. The RF-spectrum of the data is shown in Figure 9. From these two figures we measured a 29.25-dB SFDR, allowing for digitization to more than 4.5 ENOB resolution. Unfortunately, we were limited by noise and distortion due to conflicts between the 10-GHz Sigma and the DDF. This limited the system's resolution to 1.72 ENOB measured by the signal-to-noise and distortion ratio (SINAD). As show in Table I, our 30-GSPS ADC has almost the same SFDR as the LeCroy's ADC, therefore, reducing the noise complications between the Sigma and the DDF would create an electronics limited 30-GSPS ADC.

	f_S (GSPS)	SFDR (dB)	SINAD (dB)	ENOB
LeCroy Wavemaster	**10**	**31.4**	**29.7**	**4.6**
NRL Photonic ADC	**30**	**29.25**	**12.12**	**1.72**

Table I—Comparison of the LeCroy Wavemaster oscilloscope ADC with the NRL photonic ADC using the Wavemaster for back-end digitization.

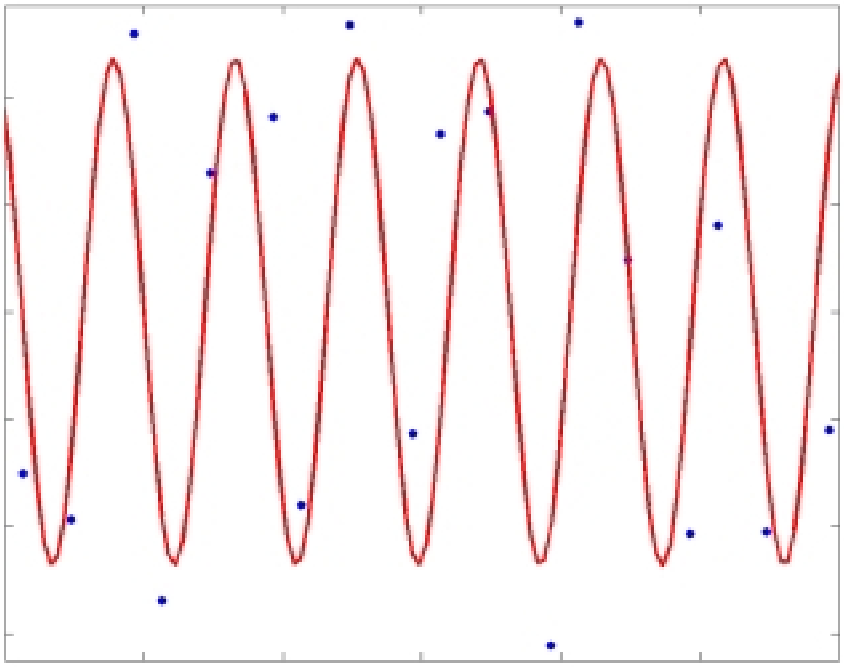

Figure 8—An 11.4-GHz waveform is digitized by a 3-channel, 30-GSPS photonic ADC

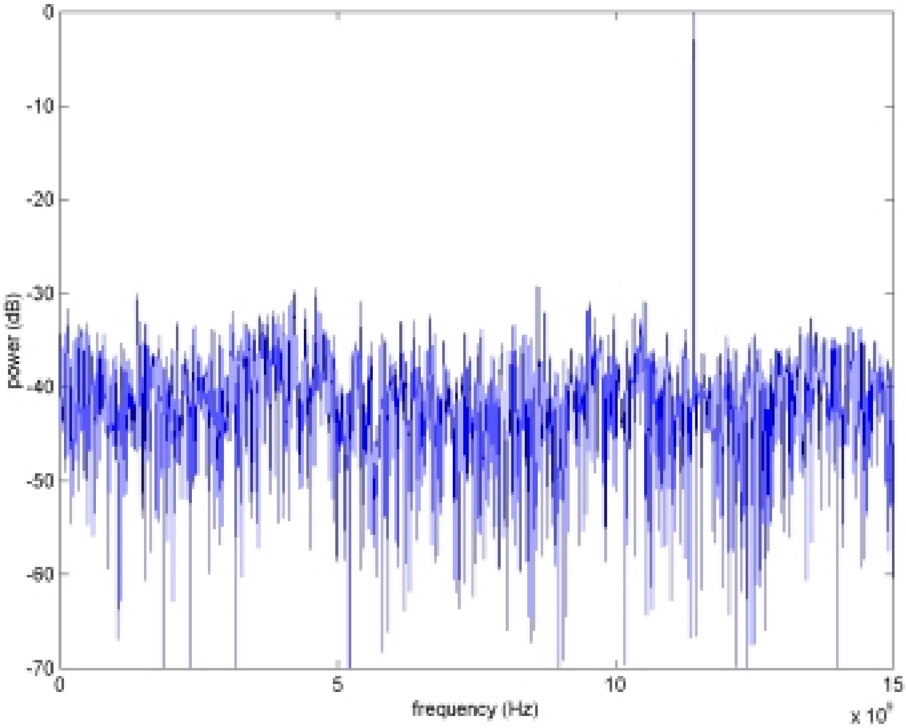

Figure 9—RF spectrum of the photonic ADC's digitized 11.4-GHz waveform.

VIII. Optimization and post-processing

A. Digital Linearization

Externally modulated photonic links employing an electro-optic Mach-Zehnder modulator (MZM) exhibit a limited spur free dynamic range (SFDR) due to the non-linear transfer characteristic of the modulator. Biasing the electro-optic modulator at quadrature typically reduces second-order distortion. Third-order distortion then limits the SFDR, especially for sub-octave bandwidths, thereby limiting the maximum optical modulation depth and signal-to-noise ratio (SNR) of the link. Most attempts to suppress third-order distortion have concentrated on analog techniques to accomplish harmonic canceling [1-3]. Recently, digital linearization of phase-modulated signals utilizing complementary outputs of a Mach-Zehnder modulator digitized at 1 MSPS has been demonstrated [4]. The above techniques have been implemented with varying degrees of success typically achieving maximum distortion suppression of ~10 dB over maximum instantaneous bandwidths of ~10 MHz with operation typically limited to modulation depths of ~0.1.

We demonstrate a 1-GSPS analog-digital photonic link employing digital linearization. The technique allows operation with optical modulation depths approaching unity (up to 0.83 demonstrated) achieving measured third-order distortion suppressions approaching 30 dB with a 500-MHz instantaneous bandwidth. The system utilizes picosecond optical pulses from a low-noise mode-locked fiber laser combined with an electro-optic amplitude modulator for high-resolution sampling operation and a conventional flash analog-digital converter for electronic quantization of the sampled signal. The limitations and benefits of the linearization technique are discussed within the context of a theoretical treatment of distortion in externally modulated links at high modulation depths. Fast Fourier Transform analysis of the digitized data is performed and indicates an electronics-limited performance of 6-bit (38 dB) signal-to-noise resolution and an 8-bit (50 dB) spur free dynamic range over the full 500-MHz instantaneous bandwidth.

The photonic link under consideration employs an optical pulse train/electro-optic modulator sampling front-end and an electronic quantization back-end. The system is shown in Figure 1. A 1-GHz train of 2-ps optical pulses from a low-noise, mode-locked fiber laser is amplified by an erbium-doped fiber amplifier to ~10-mW average power and serves as the system clock. Approximately 5% of the optical power is tapped off to clock the electronic ADC for front-end optical sampling to back-end electronic quantization synchronization. The other 95% of the optical power is used in the optical sampling of the RF signal. The RF signal to be digitized is encoded onto the 1-GHz optical pulse train with a $LiNbO_3$ Mach-Zehnder amplitude modulator (Lucent x2623C 11-GHz 3-dB bandwidth, V_π=4.3V). The output of this photonic sampler for an input 160 MHz RF signal is shown in Figure 2, captured by a real-time digitizing oscilloscope (oscilloscope not shown in Figure 1). Note the optical modulation depth is ~0.8. Optical sampling in this way is ultimately limited in resolution by amplitude and timing fluctuations of the laser. The timing fluctuations over an ~5 ms measurement time indicate a laser jitter-limited timing uncertainty of 68 fs which would correspond to a system resolution of >12 bits. The measured <0.05% amplitude fluctuations over an ~5-msec measurement time indicates >11-bit resolution potential for this sampling system. In principle, therefore, a system based on sampling with this laser can achieve performance superior to currently available technology when integrated with the proper electronics or other quantization system.

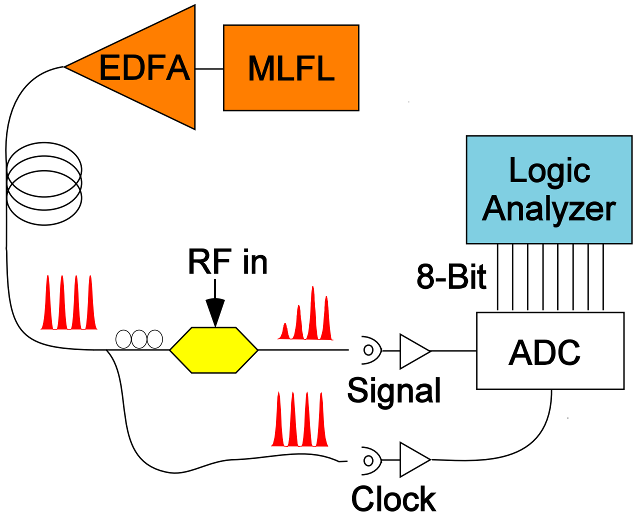

Figure 1—Experimental Layout

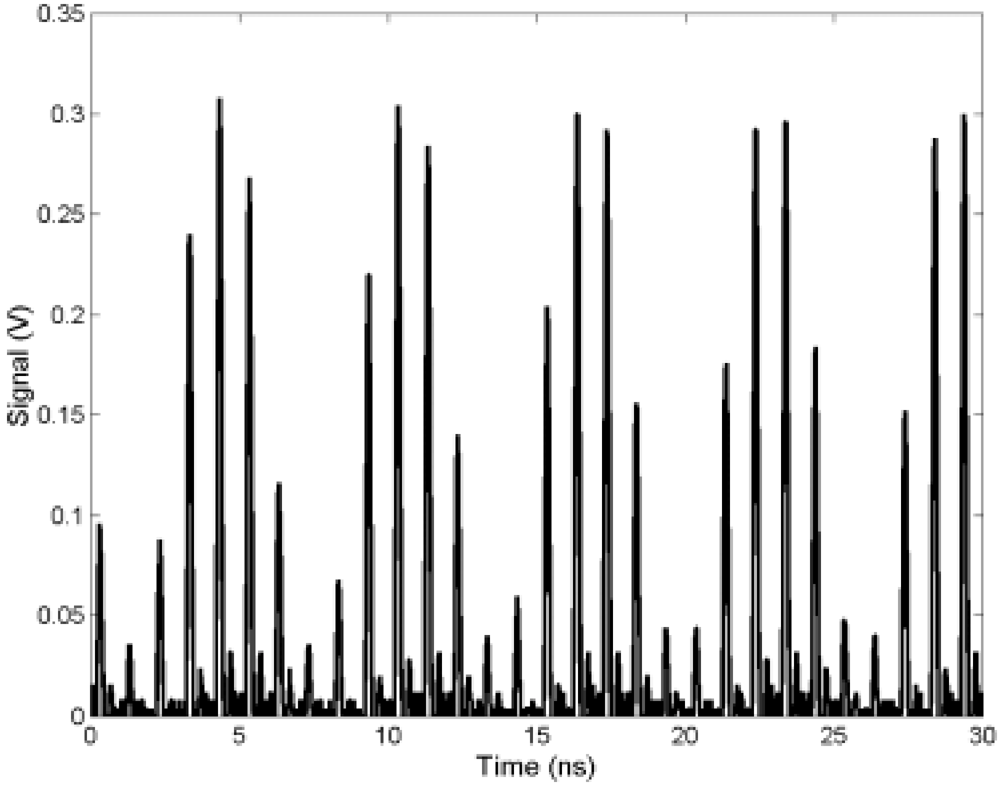

Figure 2—Photonic sampler output for a 160 MHz input RF signal as captured by a real-time digitizing oscilloscope.

The sampled RF signal information is carried on the ~1-mW average optical power modulator output to the back-end quantization system. The electronic system consists of a 10-GHz photoreceiver (Discovery DSC50) and an 8-bit, 1-GSPS electronic analog-digital converter (Maxim MAX104) which has an analog bandwidth of 2.2 GHz. The 5% optical signal tapped off before the electro-optic modulator plus a RF phase shifter ensure the ADC is clocked synchronously with the pulse train and quantizes the peak of each detected sampling pulse voltage. Digitization of the unmodulated pulse train with the above system shows the pulse-to-pulse peak fluctuation falls within the least significant bit (LSB) of the electronic ADC for ~97% of the counts and has a standard deviation of 0.56 LSB for a peak signal input of ~0.8 full scale. Clocking the electronics with a signal synchronized to the pulse train eliminates the need for an integrate-and-dump circuit following the photodiode—which would be difficult to operate reliably at these high speeds. The 1-GSPS 8-bit output data from the electronic ADC were read using a Logic Analyzer with a 1-GHz State Analyzer card (HP 16517A). The memory depth of the analyzer was 64 Kbytes providing a measurement time of 64 ms. The FFT data analysis described below was performed over the full measurement time for all runs resulting in an effective resolution bandwidth of ~15 kHz. The input analog response of the electro-optic modulator-photoreceiver system and the electronic ADC used in these experiments were measured to be independent of frequency over the 500 MHz bandwidth of interest to <0.4 dB. In addition, the electronics (photoreceiver and ADC) were operated well within their linear range.

The output optical power of an ideal Mach-Zehnder modulator is given by

$$P_{out} = \frac{1}{2} P_{in} \left(1 + \cos(\Delta\phi)\right) \qquad (1)$$

where $\Delta\phi = \pi V(t)/V_{\pi}$, $V(t)$ is the applied signal including a DC bias, $P_{in(out)}$ is the input (output) optical power and V_{π} is the modulator full-swing voltage. An externally modulated link is typically limited by third-order distortion, with second order distortion suppressed by applying a DC bias voltage equivalent to a phase difference between the two interferometer arms of $\pi/2$. This quadrature biasing results in a modulation centered on the most linear portion of the sinusoidal modulator transfer function. Here we allow for small deviations around quadrature bias by defining $V(t) = V_q + \delta V_q + V_S(t)$, where δV_q can be positive or negative and $V_s(t)$ is the signal to be digitized. Assuming the photodiode is operated over its linear range and has a flat responsivity, R, over the relevant bandwidth, the photocurrent can be shown to be

$$i(t) = \frac{RP_{in}}{2}\left(1 - \sin\varepsilon \cos\left(KV_S(t)\right) - \cos\varepsilon \sin\left(KV_S(t)\right)\right) \qquad (2)$$

where ε is the phase error associated with δV_q and $K \equiv \pi/V_{\pi}$. For system performance evaluation purposes, we are interested in the power spectral density (PSD) of the photocurrent signal. For an arbitrary input waveform, the PSD could be solved for numerically. Here we treat the instructive case of a single tone input signal $V_S(t) = V_0 \sin(\omega_0 t)$. It should be noted that distortion in Mach-Zehnder modulators has previously been addressed in the small modulation depth limit [5] and allowing for larger modulation depths [6]. Here we investigate large modulation depths, as well as quadrature error, and explore the parameter space relevant to our system. The Fourier transform of equation (2) can be analytically solved for a single tone input making use of the Bessel function identities valid for all values of V_0 and $\omega_0 t$ [7]. The expression for the PSD is given by

$$\left|i(\omega)\right|^2 = \left(\frac{RP_{in}}{2}\right)^2 ((1-\sin\varepsilon J_0(KV_0))^2\delta(\omega)$$

$$+ (4\sin^2\varepsilon)\sum_{n=1}^{\infty} J_{2n}^2(KV_0)\delta(\omega-2n\omega_0)$$

$$+ (4\cos^2\varepsilon)\sum_{n=1}^{\infty} J_{2n-1}^2(KV_0)\delta(\omega-(2n-1)\omega_0))$$

The analytical expressions for the second order distortion and third order distortion power ratios can then be shown to be

$$\frac{P(2\omega_0)}{P(\omega_0)} = \frac{\sin^2\varepsilon J_2^2(KV_0)}{\cos^2\varepsilon J_1^2(KV_0)} \qquad (3)$$

$$\frac{P(3\omega_0)}{P(\omega_0)} = \frac{J_3^2(KV_0)}{J_1^2(KV_0)}. \qquad (4)$$

Figure 3(a) shows the second (solid lines) and third order (dashed lines) distortion for modulation depths, $m = 2V_0/V_\pi$, of (i) 0.1, (ii) 0.4, and (iii) 0.8 and quadrature phase error up to 0.1 radians. Clearly, high modulation depths lead to serious degradation of the spur free dynamic range due to third order distortion. However, even second order distortion can be a significant limitation if the quadrature bias is off or drifts such that the phase change is more than ~0.01 radians. Note that as the modulation depth is increased, the second order distortion, due to quadrature error, becomes more important as well. Many photonic ADC architectures would benefit from increasing the modulation depth. This is illustrated in Figure 3(b) where the detection signal-to-noise ratio is plotted versus incident average optical power for various modulation depths. Thermal and shot noises are included in the calculation [8]. A responsivity of 1 A/W, 50Ω resistance and a bandwidth of 500 MHz are assumed for the calculation. Given that the typical photodiode response becomes nonlinear above a few mW of optical power, large modulation depths, where third order distortion dominates, will be required to achieve signal-to-noise ratios of greater than ~50 dB over the wide-bandwidths discussed here.

The nonlinearity of a Mach-Zehnder modulator is predominantly due to the sinusoidal nature of the optical interference. Compensation of this predictable distortion is therefore possible. The time-dependent signal voltage, $V_s(t)$ can be related to the digitized photoreceiver voltage, $v(t)$, using equation (1) and assuming a DC bias at quadrature, by

$$V(t) = \frac{V_\pi}{\pi}\sin^{-1}\left(1-\frac{v(t)}{v_0}\right) \qquad (5)$$

where v_0 is a measure of the detected optical power without an applied modulation signal, $V_s(t)$. The digital nature of this system, as well as other photonic analog-digital systems, lends itself to the application of this simple time-domain inverse transfer function to remove the odd-order distortion due to the modulator. The photonic system would then be limited by the second order distortion due to the quadrature error in the absence of photodiode or other system nonlinearities.

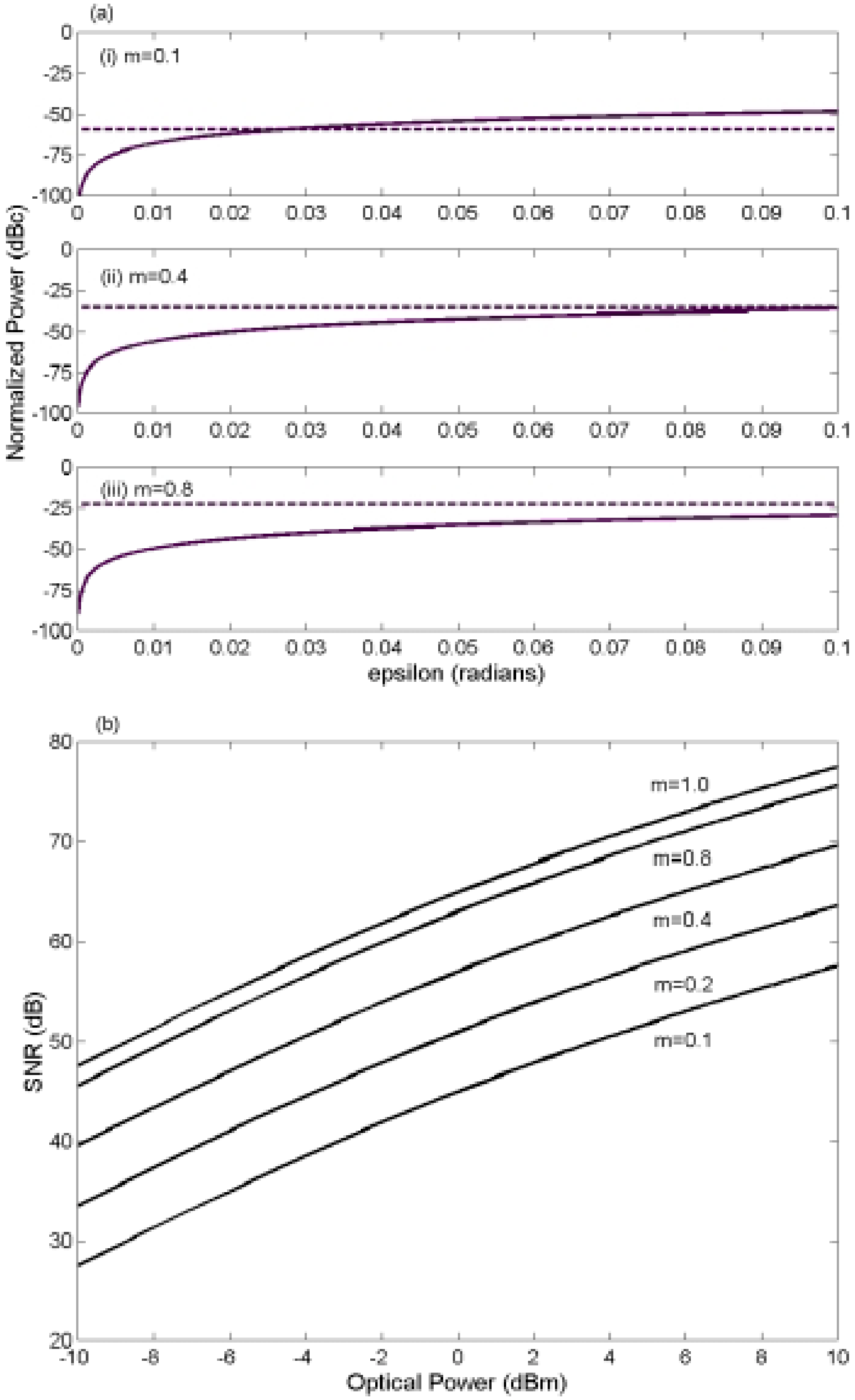

Figure 3—(a) Theoretical second order distortion power (solid lines) and third order distortion power (dashed lines) for modulation depths of (i) 0.1 (ii) 0.4 (iii) 0.8. (b) Theoretical signal to noise ratio for photoreceiver (1 A/W, 50Ω) including thermal and shot noise vs. incident optical power.

Inspection of Equation (5) indicates that this digital linearization scheme returns an undistorted voltage function provided (a) the distortion is due to the sinusoidal transfer function of the modulator, and (b) an accurate measure of the unmodulated optical power output of the modulator, v_0, is available. This second requirement is met when the signal period is small compared to the measurement time so the time averaged $\bar{v}(t) = v_0$, or an unmodulated reference pulse train is digitized. For our experiments, $f_{sig} >> 1/T_{measure}$. The frequency dependence of V_π results in a frequency dependent amplitude difference between the input and output voltage functions. The third order distortion suppression, however, is not affected by the V_π frequency dependence. Note that the detection electronics (photoreceiver and ADC) analog response must be uniform over greater than three times the input bandwidth, in the absence of any frequency domain correction steps, to allow at least third order correction by this method.

Single-tone testing was performed by applying signals from a RF synthesizer (HP 8642A). The ability of the linearization scheme to suppress distortion at large optical modulation depths (up to 0.8) was tested by passing the signal through a bandpass filter (3 dB BW ~30 MHz) prior to the modulator input to eliminate RF amplifier nonlinearities. Modulation depths approaching unity (>0.9) showed significant higher order (even as well as odd) distortion due to the strong compression and the difficulty in setting and maintaining quadrature at these input voltages. Typical single-tone FFT results are shown in Figure 4 for an input 160 MHz signal with peak-to-peak amplitude $\sim 0.73 V_\pi$. The measured data of Figure 4(a), shown normalized to the input signal is dominated by the third harmonic due to modulator transfer function distortion. Application of the time-domain transfer function of Equation (5) suppresses this distortion leaving the fundamental unchanged, see Figure 4(b). The >20 dB suppression of the third harmonic spur results in a third order distortion ~ −52 dBc. The SNR of the link over the 500 MHz bandwidth is measured to be >38 dB (SNR_{bits} = 6 bits). The digitized SNR is limited by the electronic ADC resolution and our ability to match the dynamic range of the analog photoreceiver signal to that of the electronic ADC. This 6-bit resolution is consistent with the SNR of the electronic ADC for input signal levels similar to that of the photoreceiver voltage. The SFDR over the 500 MHz bandwidth is measured to be > 50 dB ($SFDR_{bits}$ = 8 bits) and is limited in this case by non-harmonic spurs at 82 MHz and 163 MHz which are due to environmental noise.

The analog SNR of the pulse train link prior to the electronic ADC has been independently measured using a low-noise high gain RF amplifier (G=54 dB, F=1.3, f=0.01-1000 MHz) to boost the system noise to within the dynamic range of an RF spectrum analyzer (HP 8563A). The results of these measurements are shown as the solid circles of Figure 5(a) vs. modulation depth. Here the modulation depth was estimated using the amplitude of the applied RF power and the known V_π of the modulator. Note that for conditions similar to those of Figure 4 described above, the link analog SNR is ~ 60 dB. The solid curve is the theoretical signal-to-noise ratio calculated (including thermal and shot noise) for a photoreceiver responsivity of 1 A/W, 50Ω resistance and 500-MHz bandwidth and assuming a 1 mW average optical power. The experimental data deviates from the theory only at high modulation depth due to the increased power in the harmonic distortion terms.

The solid circles of Figure 5(b) show the measured third-order distortion power vs. modulation depth. The measurement of the three data points for $m < 0.1$ is limited by the noise floor of the spectrum analyzer. The solid curve is a plot of the analytical expression (equation

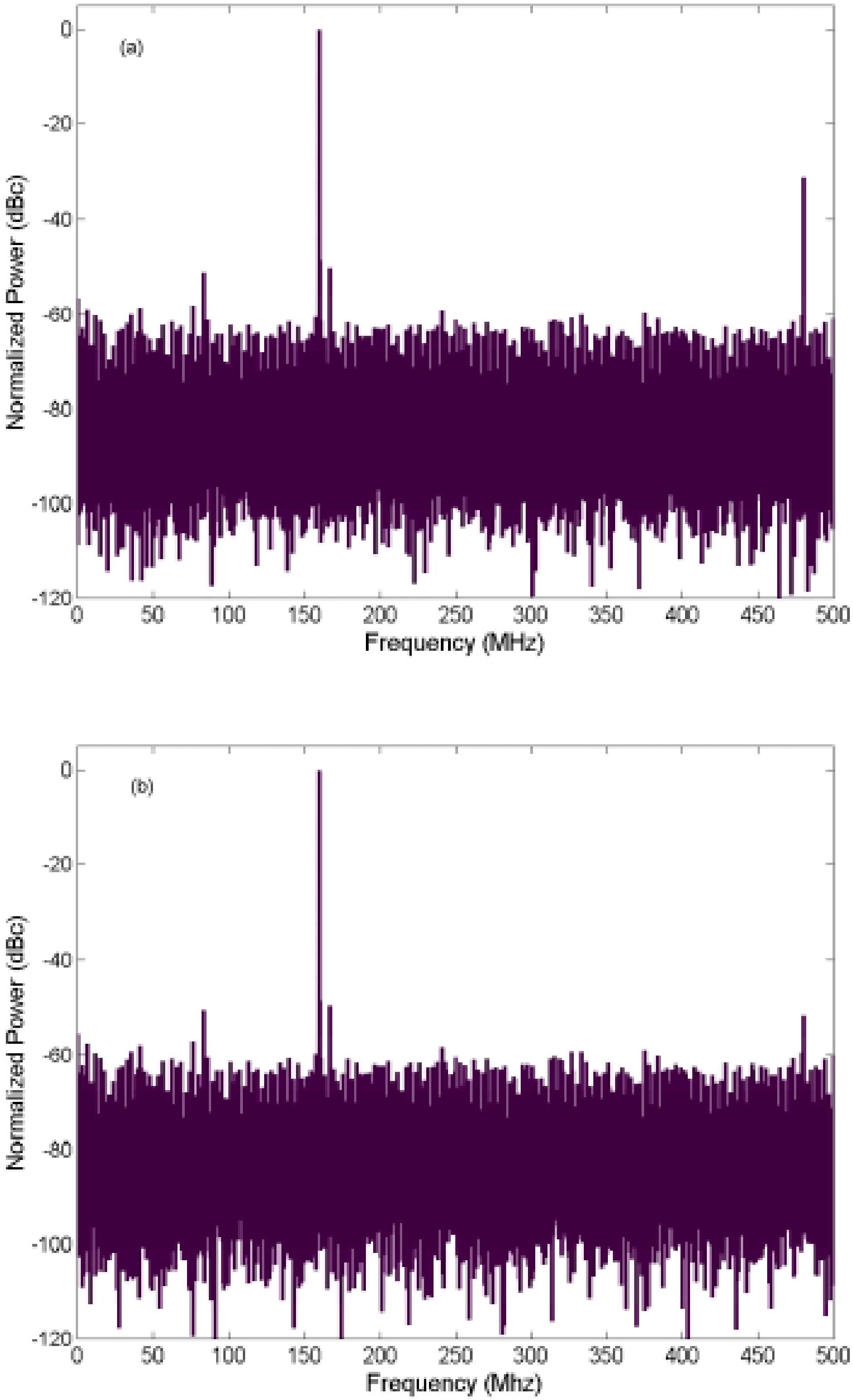

Figure 4—**Single-tone (a) non-linearized (b) linearized FFT data.**

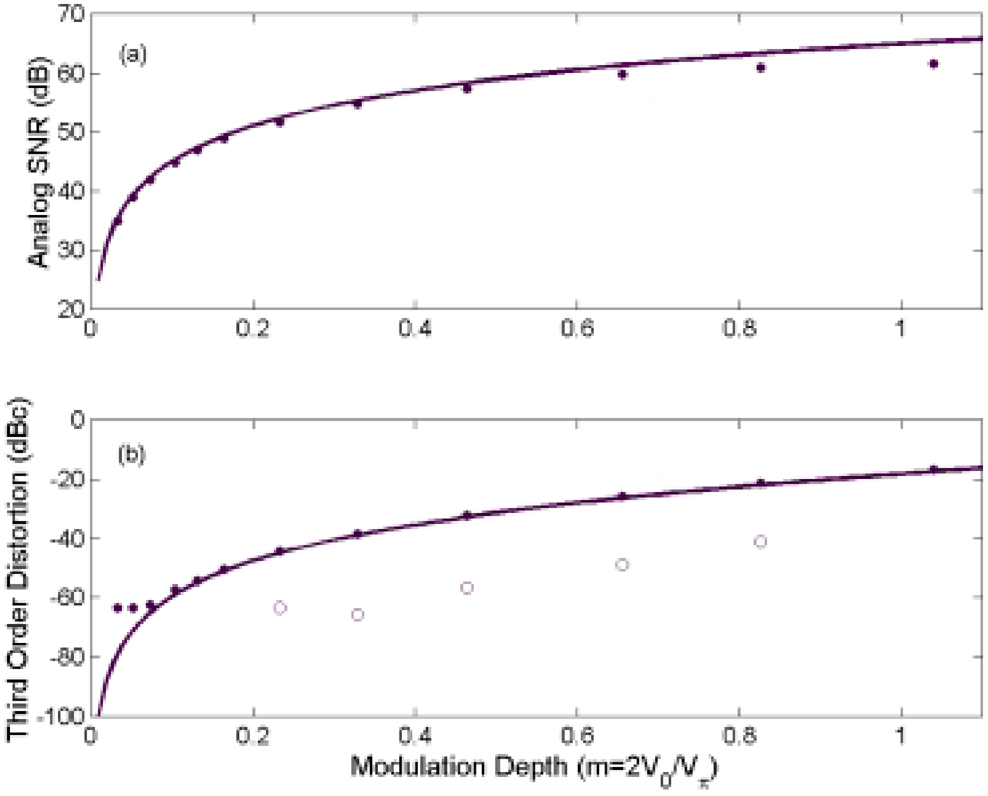

Figure 5—(a) Analog link signal to noise ratio for experimental system (solid circles) and theoretical system (solid line) assuming 1 A/W, 50Ω, 1 mW optical power vs. modulation depth. (b) Link third order distortion for analog experimental link (solid circles), digitally linearized data (open circles) and theoretical prediction for non-linearized link (solid line).

(4)) for the third-order distortion derived above vs. modulation depth. To achieve high-resolution (for example 60 dB) modulation depths above 0.5 are required and result in third-order distortion terms >–30 dBc. The open circles are measured digitized data showing the beneficial results of digital linearization. The first two data points, for $m < 0.4$, are limited by the measurement floor of the ADC due to the limited Logic Analyzer memory depth, which resulted in a resolution bandwidth limited to ~15 kHz. Third-order distortion suppression as high as 28 dB is measured with 21-dB suppression at modulation depths up to 0.83.

The second order distortion was typically below the digitized data noise floor for modulation depths below 0.3. Above 0.3, the measured second order distortion of the digitized data can be used to estimate the quadrature error. The second order distortion power averaged −50.9 dBc. For a modulation depth of 0.8, this results in a quadrature error of 8.5×10^{-3} radians or a voltage error of ~11 mV for the modulator used. This is consistent with the 0.01 V readout of the bias supply used to adjust for drift while monitoring the average optical power. In practice, an electronic quadrature bias unit would monitor the average optical power and provide feedback to continuously control the bias. In order to predict how accurate the quadrature bias must be to retain or improve upon the above results, we modify the previously discussed distortion theory. Equation (2) represents the measured photocurrent including both quadrature error, ε, and the input signal, $V_s(t)$. In the proposed linearization of equation (5), it is assumed that there is no quadrature error. The existence of quadrature error results in an erroneous measured value of both v_0 and $v\ (t)$ in equation (5). To simulate this effect, the photodiode voltage resulting from equation (2) was inserted in the numerator of equation (5) and the denominator, representing the unmodulated reference photodiode voltage, was corrected for quadrature error using $v_0' = v_0(1 - \sin(\varepsilon))$. To achieve a system resolution of 10 bits, the SNR and SFDR must be >62 dB. From Figure 5(a), this means for the ~1 mW average optical power used here, a modulation depth of >0.6 must be used which results in a theoretical third order distortion of –28 dBc. The performance of the linearization technique of equation (5) with quadrature error present is simulated by numerically analyzing FFTs of the resultant expression for the digitized photodiode voltage after the application of equation (5) in the presence of quadrature error for a single tone input, $V_s(t)$. It is found that an ε as small as 0.001 radians could be third order corrected by 46 dB to –74 dBc with a second order distortion of –68 dBc. However, an increase in error to ε=0.005 would result in a linearized SFDR limited by the second order distortion to –54 dBc with the corrected third order improvement of 35 dB to –63 dBc. Recall that $\varepsilon = \pi\,\delta V_q \big/ V_\pi$, so for the modulator in these experiments with V_π~4 V the bias error would be limited to 1.3 mV (ε=0.001) and 6.4 mV (ε=0.005). These are not unreasonable parameters to achieve, although they are outside the capabilities of the equipment used in these experiments. In other work, an in-house developed electronic quadrature bias unit has been demonstrated to maintain the phase error over a measurement time of 35 hours to within 5 mrads or a voltage of 8 mV for that experiment [9]. This unit could be expected to significantly improve future implementations of the system under test here. Other sources of distortion, which should be considered in designing an improved link (or a set of parallel links for photonic ADC architectures), include photodiode nonlinearity, ADC nonlinearity and bandlimiting of the detected photocurrent. Bandlimiting would reduce the detection sensitivity of the odd harmonic powers, resulting in their incomplete correction.

The input signals of in-field digital receivers are complex waveforms containing multiple frequencies. Further evaluation of our system for real system applications included two-tone tests. Single tone signals from two separate RF synthesizers (HP8642A and HP8340A) were amplified, filtered with 30 MHz bandpass filters to both reduce harmonics and prevent coupling between the synthesizers, and combined with a 3 dB coupler. Figure 6 shows typical two-tone FFT results for input signals of 160 MHz and 240 MHz and a peak modulation depth of ~0.7. The 320 MHz third-order intermodulation distortion signal is shown in the non-linearized data of Figure 6(a) to limit the performance of the link to a SFDR of 32 dB. Figure 6(b) shows the result of the application of the linearizing transfer function of equation (5) resulting in a reduction of the third-order distortion by > 28 dB to within the noise floor. The linearized data is limited by non-harmonic spurs to ~50 dB, as in the single-tone data.

This simple time-domain odd-order linearization scheme can be easily implemented without any potentially band-limiting and/or resolution-limiting additional analog components. Digital electronics components could be included on the electronic ADC board for fast real-time implementation in a system. Digital signal processing chips exist operating at greater than 1 GFLOP. The technique can also be seamlessly integrated into the signal processing software with little additional complexity and virtually no latency or loss of system efficiency.

We have demonstrated a 1 GSPS analog-digital photonic link employing a digital linearization scheme that allows operation with optical modulation depths approaching unity

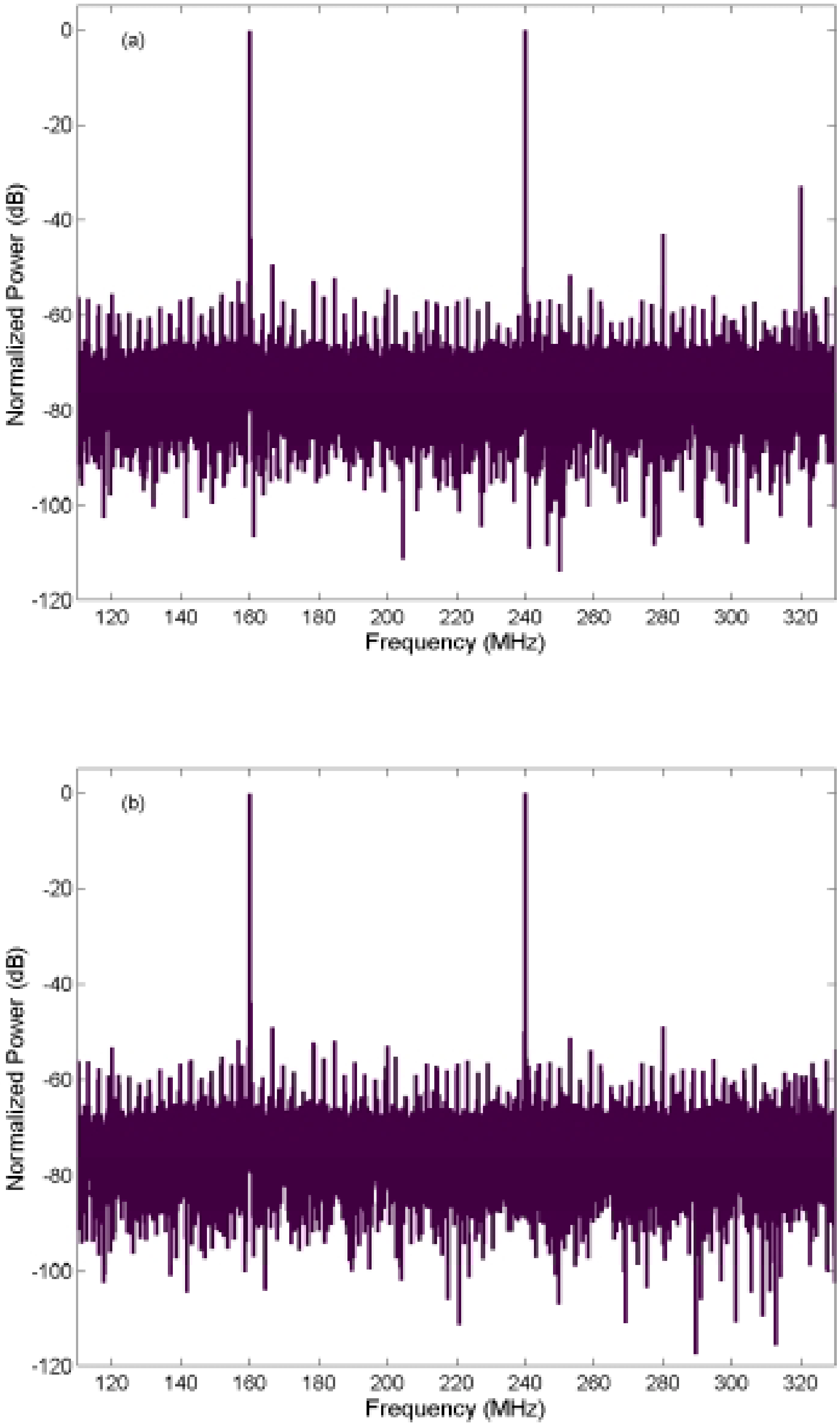

Figure 6—Two-tone (a) non-linearized (b) linearized FFT data.

(up to 0.83 demonstrated) by achieving measured third-order distortion suppression approaching 30 dB. The availability of modulation depths at this level significantly reduces the required optical power on photodetectors in single channel links and the multiple parallel channel links of recently proposed photonic ADC systems. Fast Fourier Transform analysis of the digitized data is performed and indicates an electronics-limited performance of 6-bit (38 dB) signal-to-noise resolution and an 8-bit (50 dB) spur free dynamic range over the full 500-MHz instantaneous bandwidth. Potential experimental improvements, namely matching the analog system and ADC dynamic ranges and modulator bias setting and drift control, in the current system indicate the system should perform with >10-bit (62 dB) resolution and spur accuracy with existing technology.

REFERENCES

1. S. K. Korotky and R. M. deRidder, “Dual parallel modulation schemes for low-distortion analog optical transmission,” *IEEE J. Selected Areas in Communications*, vol. 8, 1990, pp. 1377-1381.
2. M. Farwell, Z. Lin, E. Wooten, and W. Chang, “An electrooptic intensity modulator with improved linearity,” *IEEE Photonics Technology Letters*, vol. 3, 1991, pp. 792-795.
3. E. I. Ackerman, “Linearization of a Broadband Analog Optical Link using Multiple Wavelengths, ” *Microwave Photonics Tech. Dig.*, 1998, pp. 45-48.
4. J. C. Twitchell, “Photonic A/D Converters,” in *Conference on Lasers and Electrooptics Technical Digest*, Optical Society of America, Washington, DC, 1999, paper CtuN1.
5. H. Bulmer and W. K. Burns, “Linear Interferometric Modulators in Ti:$LiNbO_3$,” *J. Lightwave Technology*, vol. LT-2, 1984, pp. 512-521.
6. H. Kolner and D. W. Dolfi, “Intermodulation distortion and compression in an integrated electrooptic modulator,” *Applied Optics*, vol. 26, 1987, pp. 3676-3680.
7. G. Arfken, *Mathematical Methods for Physicists*, Academic Press, San Diego, CA, 1985, pp. 577-580.
8. G. P. Agrawal, *Fiber-Optic Communication Systems*, John Wiley & Sons, Inc., New York, NY, 1997, pp. 163-167.
9. R. Madara and P. Biernacki, Naval Research Laboratory, private communication.

B. Feed-Forward Noise Eater: Suppression of Supermode Oscillations

The microwave frequency spectrum of the Sigma laser used for many of the photonic ADC systems is marred by the presence of peaks from supermode oscillations of the laser. As the free spectral range of the laser cavity is 3 MHz, these oscillations show up in the microwave spectrum as a comb of peaks with approximately even heights spaced 3 MHz apart. This comb extends from DC to well beyond the fundamental repetition rate of the laser. These lines have intensities approximately 60-dB below the fundamental, but they can become significant in applications like the photonic ADC, where linearity concerns can limit modulation depths to ~10%.

In an attempt to reduce the impact of these lines on the photonic ADC experiments, a feed-forward noise eater was constructed, as shown in Figure 1. The amplified output of a Sigma laser operating at a 960-MHz pulse repetition rate is distributed into two different pathways. Along the first pathway, the laser is fed through a length of delay fiber, then through a Mach-Zehnder modulator (MZM). Along the second line, the optical signal is converted into a microwave signal that is then sent along a length of coaxial cable to a lowpass filter and an amplifier, the microwave output of which drives the MZM to influence the optical signal on the first pathway. The bias on this MZM is adjusted to a quadrature point with a negative slope, which introduces a phase shift of π between the microwave input and the optical output. Thus, the second path detects noise fluctuations in the laser and produces a microwave signal that, when fed into the properly biased MZM, serves to cancel out those fluctuations.

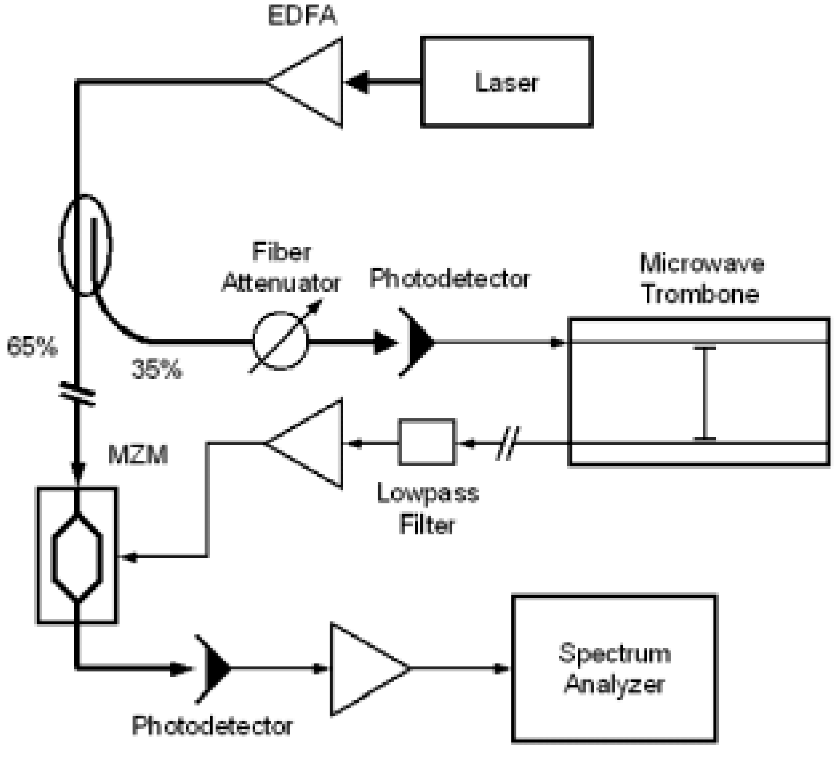

Figure 1—A schematic of the noise eater and test system.

For this to work the two pathways must have the same relative delay and the gain on the second pathway must be controlled to maximize the cancellation. The microwave pathlength along the second path can be adjusted, using cables for coarse adjustment and the microwave trombone for fine adjustment, to exactly match the optical pathlength along the first path. Gain control can be accomplished using the fiber attenuator. In addition, the microwave signal along the second path must be band-limited to below the laser's Nyquist frequency (in this case, 480 MHz), so that the noise eater does not attempt to cancel out the pulse train at the fundamental repetition rate.

A noise eater of the sort shown in Figure 1 was constructed and demonstrated in the laboratory. The test system used microwave amplifiers (Miteq AM-2A-000110) that provide ~ 26 dB of gain between 1 MHz and 1 GHz and a lowpass filter (Mini-Circuits SLP-450) with a nominal cut frequency of 450 MHz. As the band edge of the lowpass filter is neither arbitrarily sharp nor positioned directly at the Nyquist frequency, the ability of this circuit to cancel noise is reduced at frequencies approaching Nyquist. The result of using a noise eater of this sort is shown in Figures 2 and 3. Figure 2 shows the microwave spectrum of the optical pulse train between DC and 480 MHz with the microwave arm of the noise eater turned off; the comb of peaks from the supermode oscillations are clearly visible across the entire band. Figure 3 shows the microwave spectrum of the optical pulse train with the noise eater engaged. Most of the supermode peaks below 350 MHz have been suppressed by more than 10 dB, while the supermode peaks above 450 MHz seem to have been slightly amplified. Neglecting the large and irrelevant DC peak, the noise eater reduced the total power in supermode oscillations below 480 MHz by 3.5 dB. It is apparent from the figures that the noise eater's performance degrades considerably above 350 MHz, most likely due to the aforementioned limitations on the performance of the bandpass filter; at frequencies below 350 MHz, the noise eater reduces the power in supermode oscillations by 10.7 dB. This suggests that a noise eater constructed with a very sharp filter with a band edge right at Nyquist might have significantly improved performance compared to the current system.

The performance of such a feed-forward system has also been effective at reducing noise on a 10-GHz repetition rate Sigma laser with a fundamental cavity resonance of ~1 MHz. Amplitude and phase noise tests demonstrate a 25-dB reduction in total amplitude noise integrated over a bandwidth of 100 Hz to 1 MHz. These tests clearly show a marked reduction in spurious noise in the 10's of kHz range. The cause of this noise is due to the laser relaxation rate as well as noise from switching power supplies, external and internal to the Sigma laser. In these tests the first cavity beat tones (at ~ 1, 2, and 3 MHz) have been reduced by nearly 15 dB.

This feed-forward design is a simple and effective method for suppression of supermode oscillation spurs from a harmonically modelocked laser, such as the Sigma laser. The performance improvement in photonic ADC systems can be quantified by an increase in the total signal to noise and distortion ratio (SINAD), which currently limits many systems using the Sigma laser. With >15-dB suppression of the Sigma laser's supermodes, the resolution of a photonic ADC is increased by almost 3 ENOB.

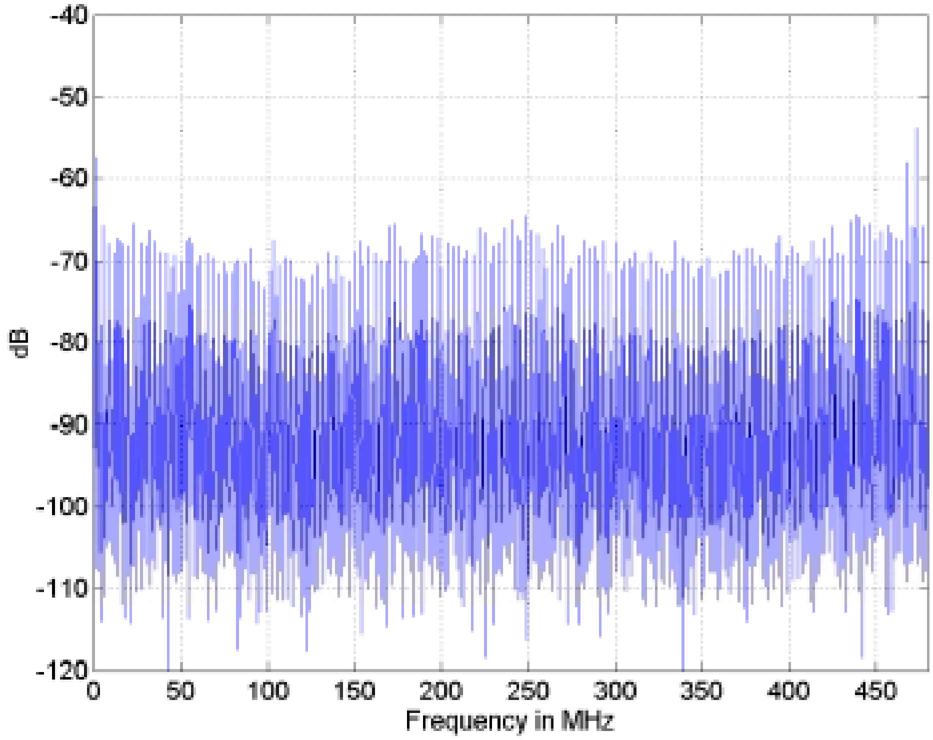

Figure 2—The microwave spectrum of the optical pulse train with the noise eater disengaged.

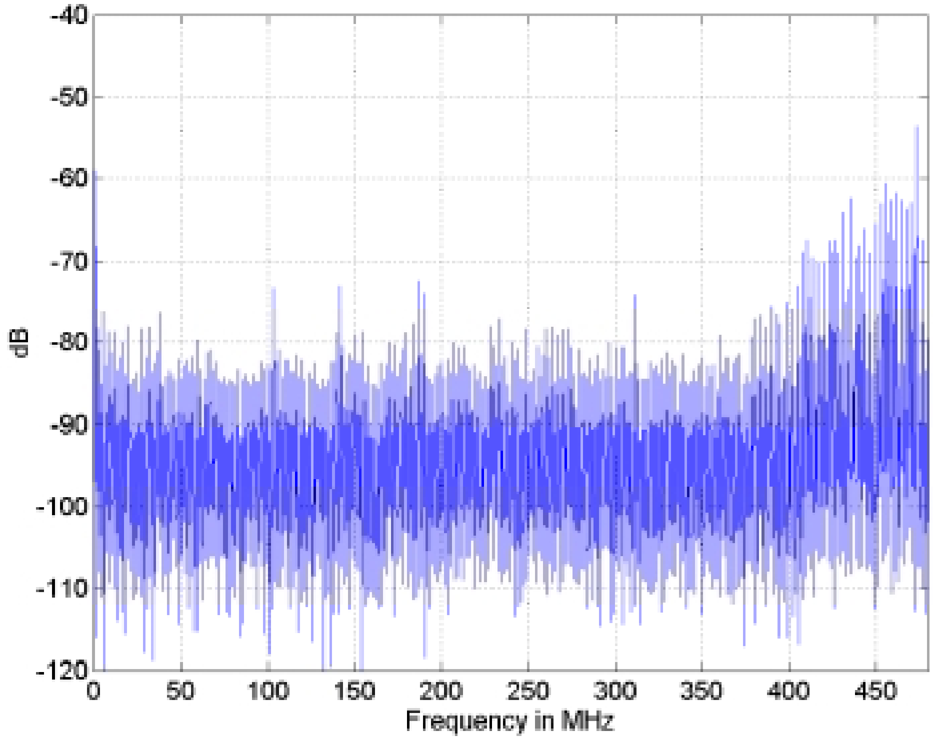

Figure 3—The microwave spectrum of the optical pulse train with the noise eater engaged.

C. Non-uniform optical sampling of microwave signals

Parallel ADC systems exhibit some degree of interleaving error when recombining multiple channels. This error is best minimized in hardware, but is often still evident in the final digitized data. A novel computational method was developed for rapid evaluation of the spectral content of data acquired by nonuniform repetitive sampling. This post-processing method is capable of correcting for established time errors between channels in the ADC. This will reduce errors and maximize the dynamic range of the photonic ADC system.

I. The Algorithm

a. Digital Spectra of Time-Interleaved Signals

Suppose a multichannel sampling system is constructed consisting of M samplers, each of which takes K total samples at a sampling rate of $(MT)^{-1}$, and that the sampling times of the channels are delayed arbitrarily with respect to each other. The samples from the individual channels can then be interleaved in time to give MK samples of an input signal spanning a time period given by MKT. The sampling times t_n, where $0 \le n \le MK-1$, can then be written as:

$$t_n = nT + \Delta_n \qquad (1)$$

Δ_n is thus a periodic sequence with period M. The interleaved nature of the data set can be made explicit by redefining n as a function of m, the channel number, and k, the index into the individual-channel data set:

$$n(k,m) = kM + m \qquad (2)$$

where $0 \le m \le M-1$ and $0 \le k \le K-1$. Substitution of (2) into (1) and rearrangement gives:

$$t_{n(k,m)} = kMT + mT + r_m T \qquad (3)$$

where $r_m = \Delta_m / T$ is the relative sampling offset of the m^{th} channel.

The spectrum of a set of time-series data can be given as its discrete Fourier transform (DFT):

$$X_d(f_a) = \sum_{n=0}^{MK-1} h_n \exp[-2\pi i f_a t_n] \qquad (4)$$

where h_n is the sample of the signal of interest at the n^{th} time, and where f_a is the frequency at which the spectrum is evaluated. Note that the periodic nonuniform sampling used to acquire the data set of interest renders invalid the application of a fast Fourier transform (FFT) algorithm, which relies on an assumption of evenly-spaced data [1]. Typically, the values of f_a will be evenly-spaced between the positive and negative Nyquist frequencies, $\pm f_{ny} = \pm 1/2T$:

$$f_a = \frac{a}{MKT} \qquad (5)$$

$$-\tfrac{MK}{2} \le a \le \tfrac{MK}{2} \qquad (6)$$

Substitution of (2), (3), (5) into (4) and separation of the overall summation into summations over the individual channels gives:

$$X_d(f_a) = \sum_{m=0}^{M-1} \exp\left[\frac{-2\pi i a(m + r_m)}{MK}\right] \sum_{k=0}^{K-1} h_{n(k,m)} \exp\left[\frac{-2\pi i a k}{K}\right] \qquad (7)$$

The first summation in (7) suggests that a channel- and frequency-dependent phase factor may be introduced to simplify notation:

$$\theta(m,a) = \frac{-2\pi a(m+r_m)}{MK} \tag{8}$$

The second summation is just the discrete Fourier transform of the data from the m^{th} channel:

$$X_f^m(f_a) = \sum_{k=0}^{K-1} h_{n(k,m)} \exp\left[\frac{-2\pi iak}{K}\right] \tag{9}$$

Substitution of (8) and (9) into (7) gives:

$$X_d(f_a) = \sum_{m=0}^{M-1} X_f^m(f_a) \exp[i\theta(m,a)] \tag{10}$$

If K is a multiple of 2, then (9) can be evaluated using an FFT, so evaluation of (10) requires a total of M FFTs.

b. Implementation of Jenq's Method

Jenq's method [2] allows the computation of an estimate of the true spectrum of the signal, X_c, from the spectrum of the sampled signal, X_d, using the following matrix equation:

$$[X_c] = [A]^{-1} T[X_d] \tag{11}$$

where $[X_c]$ and $[X_d]$ are $M \times N$ matrices and $[A]$ is an $M \times M$ matrix:

$$[X_c]_{mn} = X_c\left(f_n - \tfrac{1}{2T} + \tfrac{m}{MT}\right) \tag{12}$$

$$[X_d]_{mn} = X_d\left(f_n + \tfrac{m}{MT}\right) \tag{13}$$

$$f_n = \frac{n}{NMT} \tag{14}$$

$$[A]_{mm'} = A\left(\tfrac{M}{2} + m - m'\right) \tag{15}$$

$$A(x) = M^{-1} \sum_{m=0}^{M-1} \exp\left[\frac{-2\pi ix(m+r_m)}{M}\right] \tag{16}$$

where $0 \le m,m' \le M-1$ and $0 \le n \le N-1$. $N = FK$, where F, the oversampling factor, is a positive integer; setting F greater than unity results in an interpolated spectrum with F times as many points as were in the original data set. To allow the use of fast Fourier transforms in the evaluation, F and K should always be powers of two.

For this method to function properly, M must be a multiple of two. However, many potential real-world applications, such as interleaved sampling from three, five, or seven channels, would naturally call for an odd-valued M. To get around this problem, the data from each of the M channels may be decimated by two to give $2M$ effective channels, each with a sampling period of $2MT$. The above method, with appropriate adjustments to M, N, T, K, and r, may then be used to give the desired spectrum.

It is clear from (13) and (14) that X_d will need to be evaluated at NM frequencies evenly spaced between zero and $(NM-1)/(NMT)$. From (10), it can be seen that this will require the evaluation of (9) over the same range of frequencies. As mentioned before, (9) can be evaluated using an FFT. However, a typical algorithm will compute the FFT of a K-point set of data at a total of K specific frequencies. If the sampling rate is $1/MT$, then the FFT will be evaluated at frequencies ranging from $-1/(2MT)$ to $1/(2MT)$ in increments of $1/MKT$. This gives $K + 1$ total points, but the first and last data point in the set are identical, so there are only K independent points. If the data have been zero-padded to a total of N points, then the frequency range will remain the same, but the increment will be $1/NMT$. The zero padding thus achieves the desired frequency increment, but the range is incorrect. To extend the range, the symmetry of the evenly-spaced DFT can be exploited: If q is an integer, then the DFT of an evenly-spaced data set in the range from $(2q - 1)/(+2MT)$ to $(2q + 1)/(+2MT)$ is equal to the DFT of the same data from $-1/(2MT)$ to $1/(2MT)$. Thus, (9) can be evaluated over the entire range of interest using the values returned by a standard FFT algorithm.

II. Examples and Results

a. Noiseless Data and SFDR

To test the effectiveness of this implementation of Jenq's method in removing spurious peaks, several sets of noiseless synthetic data were analyzed. Figure 1 shows the spectra of a test signal constructed in the time domain from a noiseless sinewave tone at a frequency of 1239 MHz, with $K = 4096$, $M = 4$, $F = 4$, $T = 0.25$ ns, $r_1 = 0$, $r_2 = -0.25$, $r_3 = 0.25$, and $r_4 = 0.5$. These conditions simulate nonuniform repetitive sampling by a system composed of four channels, each of which samples at 1 GHz; the effective sampling rate of the complete system is thus 4 GSPS, and the effective overall Nyquist frequency is 2 GHz. Before processing, the synthetic data were passed through a four-point Blackman-Harris filter [3] to reduce spectral leakage.

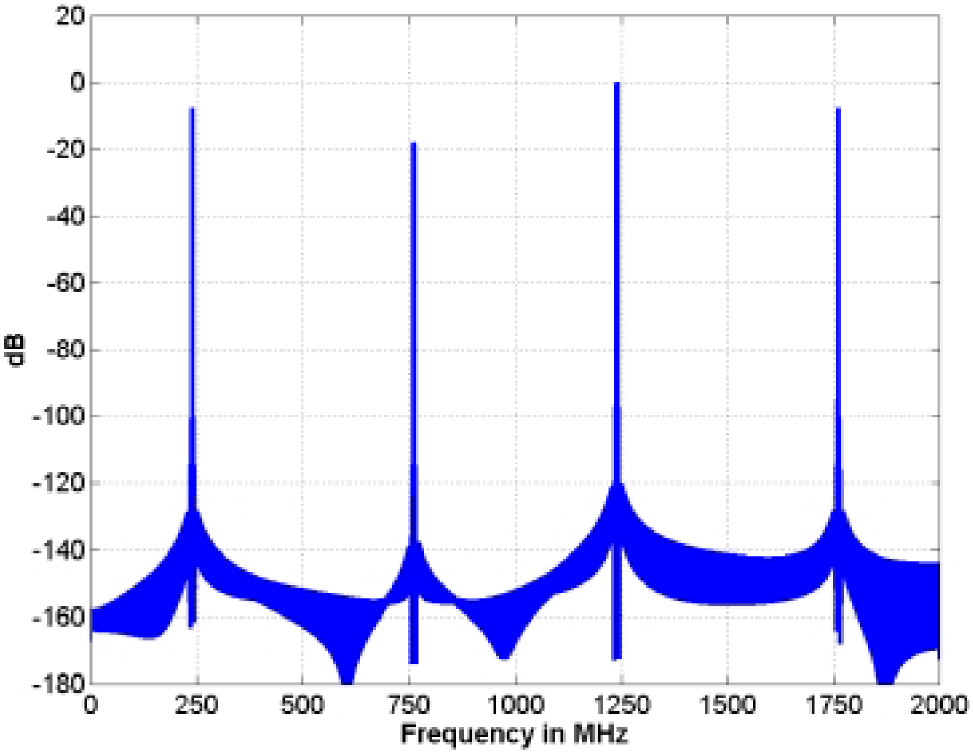

Figure 1--Spectrum of nonuniformly sampled single-tone synthetic data ($f = 1293$ MHz, $K = 4096$, $M = 4$, $F = 4$, $T = 0.25$ ns, $r_1 = 0$, $r_2 = -0.25$, $r_3 = 0.25$, $r_4 = 0.5$) evaluated by an FFT. The signal tone is apparent at 1239 MHz, as are the spurs at 239 MHz, 761 MHz, and 1761 MHz. These spurs limit the SFDR of the spectrum to 7.6 dB.

Figure 1 shows the power spectrum of this data set obtained using a simple FFT. There are three large aliasing spurs present in the spectrum, corresponding to mixing products of the signal tone at 1239 MHz and the single-channel sampling rate of 1 GHz. These spurs limit the spur-free dynamic range (SFDR) to 7.6 dB. Figure 2 shows the power spectrum of the same data evaluated using the implementation of Jenq's method presented here. The SFDR of this spectrum is greater than 92 dB, limited only by the spectral leakage characteristic of the Blackman-Harris window.

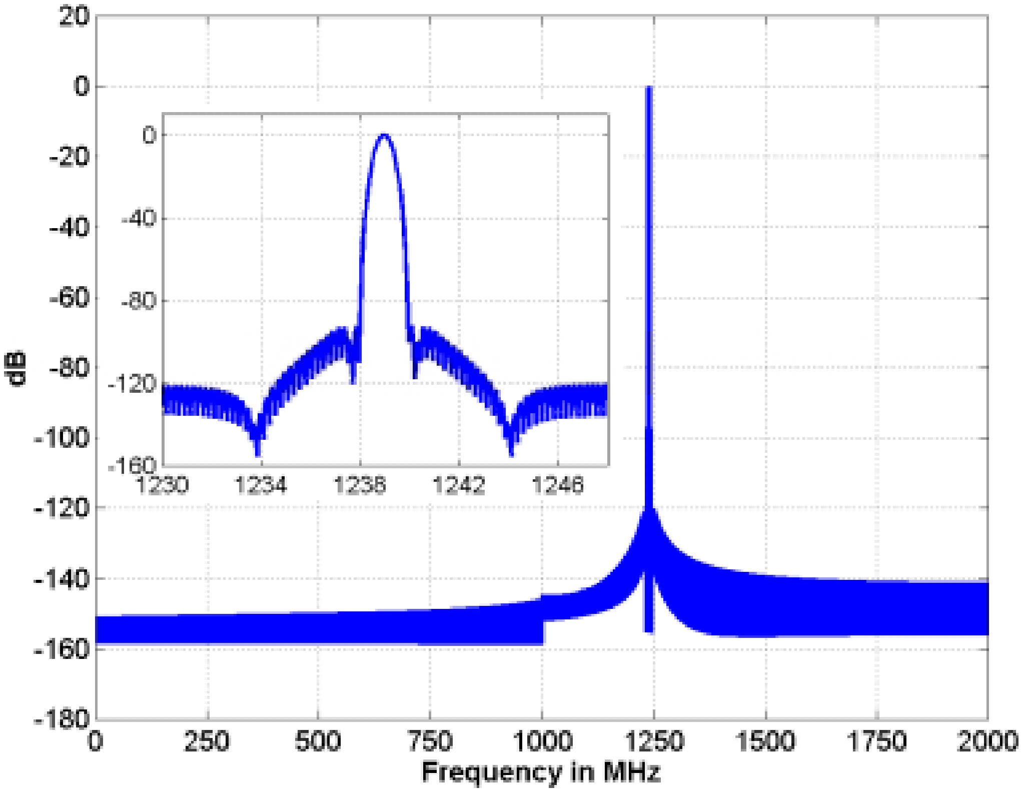

Figure 2—Corrected spectrum of the same data whose spectrum is shown in Figure 1. The correction method has eliminated the three large spurs, leaving only the tone at 1239 MHz. The inset shows the shape of this line, which is characteristic of the Blackman-Harris window. Spectral leakage limits the SFDR to 92 dB.

To test the influence of multiple tones, a synthetic signal was constructed using the sampling parameters described above, but with equal-intensity sine-wave tones every 250 MHz from 35 MHz to 1785 MHz. The spectrum calculated directly from a single FFT is shown in Figure 3; multiple spurs limit the SFDR to no better than 10 dB. In addition, the presence of spurs has drawn power disproportionately out of the high-frequency peaks, depressing their intensities relative to the low-frequency peaks. The spectrum calculated using Jenq's method is shown in Figure 4. As before, the method was entirely successful in removing the spurious peaks, leaving a set of peaks with equal heights at exactly the frequencies of the input tones. Also as before, the SFDR of the spectrum is >90 dB, limited by spectral leakage sidebands characteristic of the Harris-Harris window function.

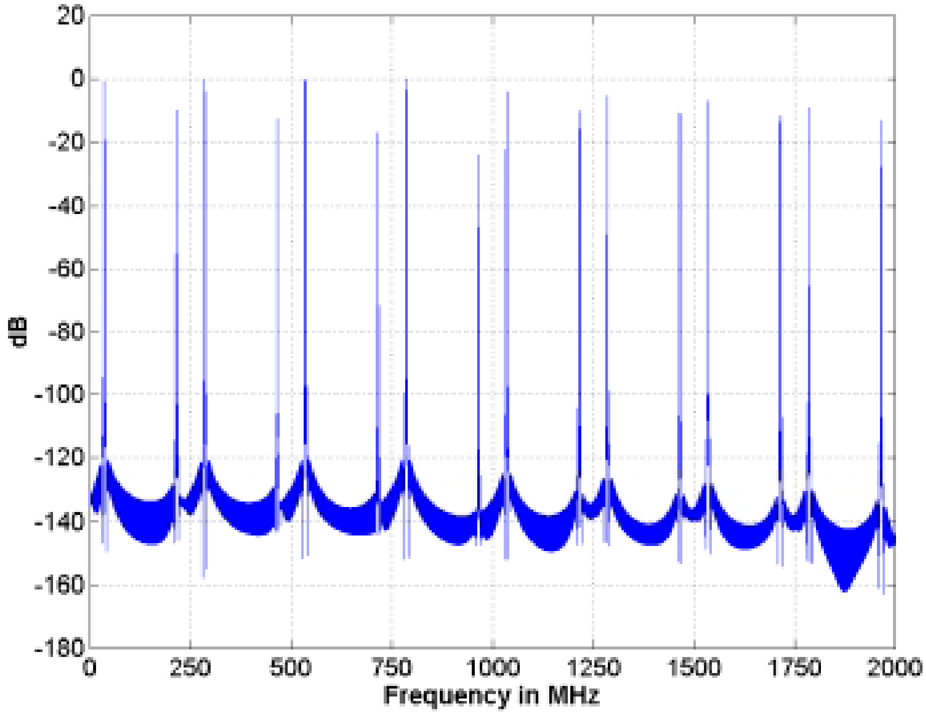

Figure 3—Spectrum of nonuniformly sampled multitone synthetic data (f = 35 MHz through 1785 MHZ in increments of 250 MHz, $K = 4096$, $M = 4$, $F = 4$, $T = 0.25$ ns, $r_1 = 0$, $r_2 = -0.25$, $r_3 = 0.25$, $r_4 = 0.5$) evaluated by an FFT. Mutliple spurs are evident and the heights of the peaks corresponding to the tones are uneven.

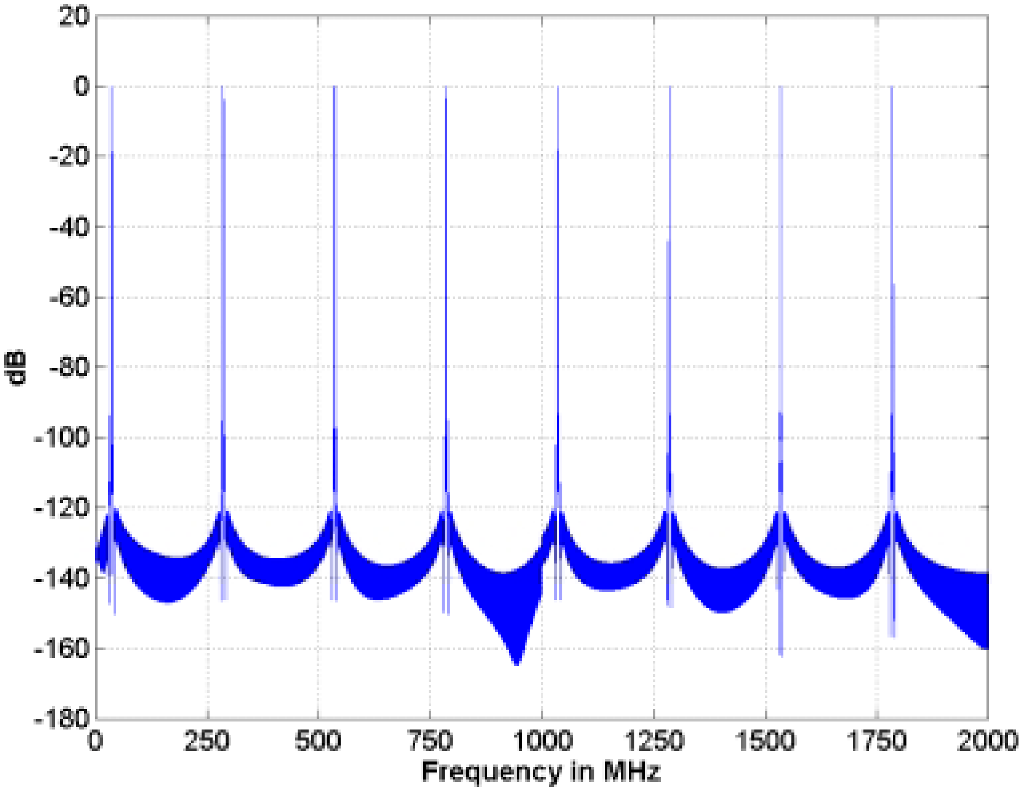

Figure 4—Corrected spectrum of the same data whose spectrum is shown in Figure 3. The correction method has eliminated all of the spurs, and heights of the peaks corresponding to the tones are even.

b. Noisy Data and the Effects of Relative Delay

The SFDR of noiseless data corrected using Jenq's method is limited almost exclusively by the spectral leakage associated with window function employed, and is independent of the relative delay, r for $|r| \leq 0.99$. However, when noise is introduced into the system, the use of a sampler whose r values differ significantly from unity can result in the degradation of the SINAD and SFDR. To demonstrate this effect, simulated sampled data were acquired (with K = 4096, M = 2, F = 4, T = 0.5) from synthetic, noisy signals, $D(t)$, of the following form:

$$D(t) = S\sin(2\pi f t) + \frac{\sqrt{2}}{2} N g(t) \tag{17}$$

where S is the signal amplitude, N is the noise amplitude, and $g(t)$ is Gaussian-distributed random noise with a mean of zero and a standard deviation of unity. The nominal SINAD of such a signal is simply S/N. The spectra of the sampled data were then calculated using the methods presented in Section II and the SINAD and SFDR were then determined from these spectra.

The results of one set of these tests (f = 739 MHz, $-0.99 \leq r \leq 0.99$ in increments of 0.01, S/N = 50 dB) are plotted as open circles in Figure 5 (SINAD) and Figure 6 (SFDR); similar results were found for any choice of f below the effective system Nyquist frequency of 1 GHz.

Both the SINAD and SFDR vary as the cosine of *r*; this is shown by the solid lines in each figure, which are cosine functions of the following form:

$$y = \frac{p}{2}\cos(\pi r) + \frac{p}{2} \tag{18}$$

For Figure 5, $p = 1 \times 10^5 = 50$ dB, while for Figure 6, $p = 2.29 \times 10^7 = 73.6$ dB.

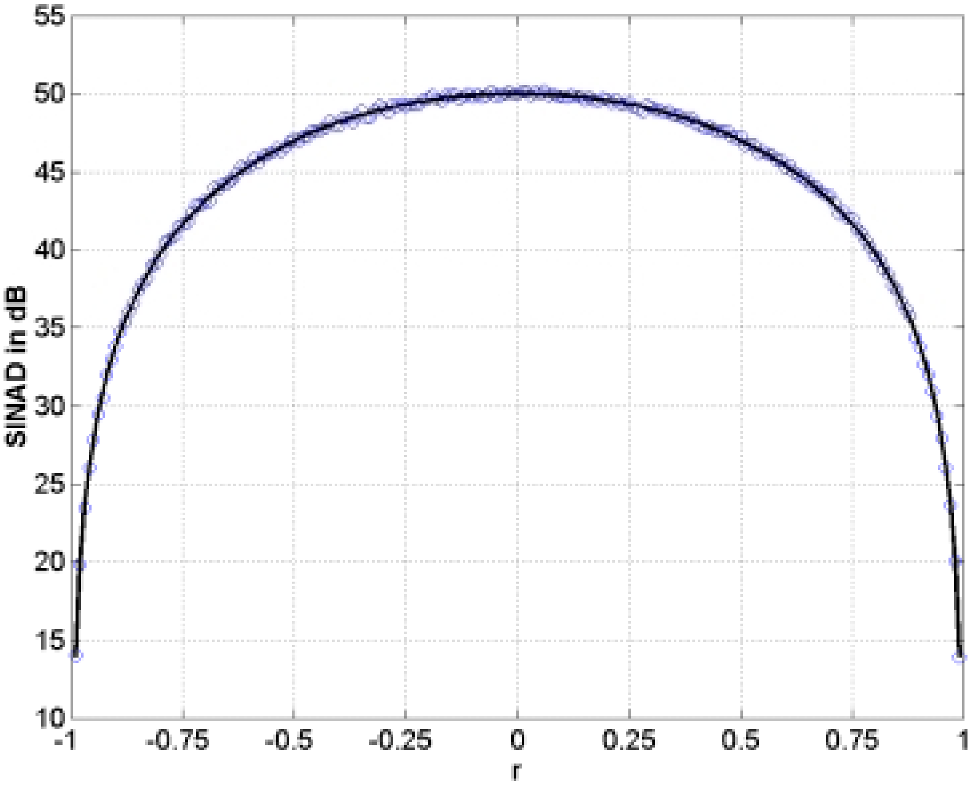

Figure 5—The dependece of SINAD on sampling. The open circles are the measured SINAD of sets of synthetic data with a nominal SINAD of 50 dB (*f* = 789 MHz, *K* = 4096, *M* = 2, *F* = 4, *T* = 0.5 ns, *r* ranges from –0.99 to 0.99 in increments of 0.01) as a function of the relative sampling offset *r*. The data lie on a cosine function (solid line).

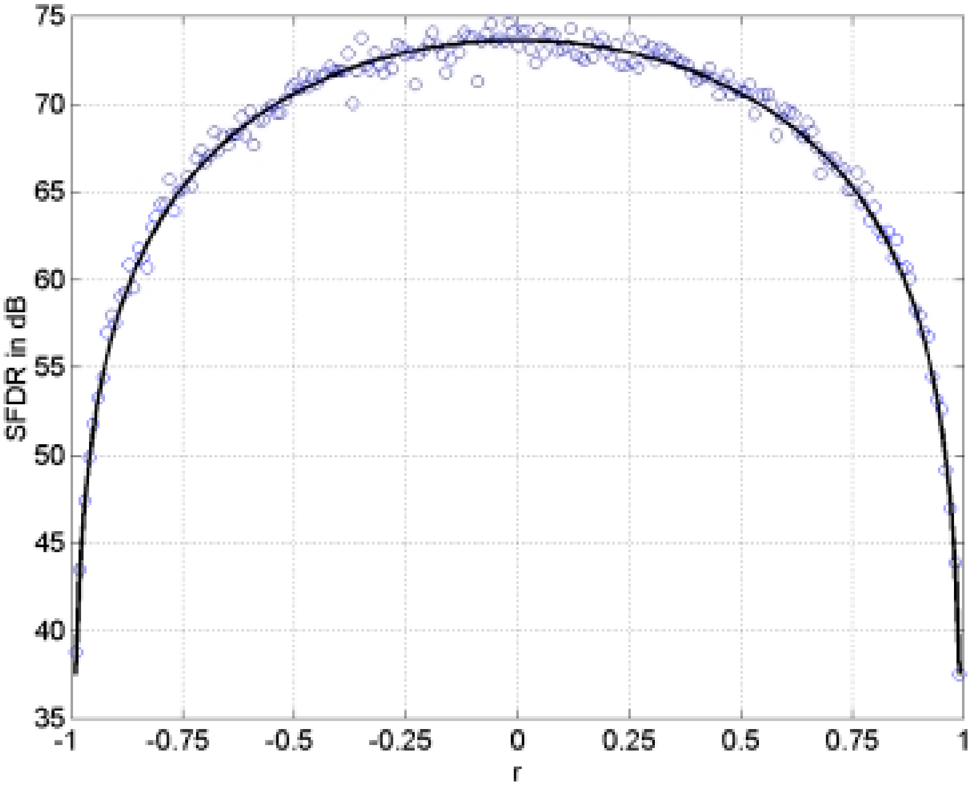

Figure 6—The dependece of SFDR on sampling. The open circles are the measured SFDR of sets of synthetic data with a nominal SINAD of 50 dB ($f = 789$ MHz, $K = 4096$, $M = 2$, $F = 4$, $T = 0.5$ ns, r ranges from –0.99 to 0.99 in increments of 0.01) as a function of the relative sampling offset r. The data lie on a cosine function (solid line).

c. Computational Complexity

To compute $[X_c]$, (11) must be evaluated, which amounts to solving N systems of M simultaneous linear equations. As $[A]$ is an $M \times M$ Toeplitz matrix, solution of any one system will be of order M^2, so complete evaluation of (11) will be of order FKM^2. Computation of $[X_d]$ using (4) is of order M^2FK^2, while computation of it using (10) is of order $MK \log_2 K$; the latter method is thus strongly preferred in practice. Evaluation of $T[X_d]$ from $[X_d]$ requires FKM operations, and computation of $[A]$ requires on the order of M^2 operations. Thus, the complete calculation using this algorithm will be of order ($MK \log_2 K + FKM + FKM^2 + M^2$). Taking the highest order at which each factor appears, the overall order of the computation is thus approximately $M^2FK \log_2 K$. This expression varies with K in a manner analogous to the way an FFT varies with the size of the input data set. Thus, so long as M remains small, this method will remain approximately as computationally tractable as an FFT on a data set of the same size.

III. Conclusions

A novel computational method was developed for rapid evaluation of the spectral content of data acquired by nonuniform repetitive sampling. This method allows for the calculation of the true discrete Fourier transform, X_d, of the complete data set from the fast Fourier transforms of the data sets from each channel taken individually. Jenq's method can then be used to extract the true spectrum, X_c. The effectiveness of this method was demonstrated on noiseless, synthetic data, where it completely eliminated all of the spurs that were present in the FFT spectra of the data. In the analysis of noisy data, it was found that the SINAD and SFDR of the data decreased as the relative sampling interval, r, was adjusted away from the condition of uniform sampling. The dependence of the SINAD on r suggests that care must be taken to keep r small when developing real-world applications of nonuniform sampling. Finally, it was determined that the computational complexity of the correction procedure outlined scales similarly to the FFT with increases in the sizes of data sets.

REFERENCES

[1] N. Kurosawa, H. Kobayashi, K. Maruyama, H. Sugawara, and K. Kobayashi, "Explicit analysis of channel mismatch effects in time-interleaved ADC systems," *IEEE Transactions on Circuits and Systems I: Fundamental Theory and Applications*, vol. 48, pp. 261-71, 2001.

[2] W. H. Press, B. P. Flannery, S. A. Teukolsky, and W. T. Vetterling, *Numerical Recipies: The Art of Scientific Computing (FORTRAN Version)*. New York: Cambridge University Press, 1989.

[3] Y. Jenq, "Perfect reconstruction of digital spectrum from nonuniformly sampled signals," *IEEE Transactions on Instrumentation And Measurement*, vol. 46, pp. 649-652, 1997.

[4] F. Harris, "Use of windows for harmonic-analysis with discrete fourier-transform," *Proceedings of the IEEE*, vol. 66, pp. 51-83, 1978.

IX. Optical Quantization via Distributed Phase Modulation

Optical phase modulators were used to quantize microwave signals using a standard cw laser of frequencies up to 25 GHz. A two and three bit optical quantizer and photonic analog-to-digital converter are demonstrated. The quantizer system is primarily limited in the optical domain by the speed of the phase modulators. Converting the optical binary data into the electrical domain limits the data acquisition to the electronic readout circuitry.

Most photonic ADCs employ electronic ADCs as the final stage in conversion. These use the strengths of the photonic system (high-speed sampling and low-aperture jitter) to extend the performance of the electronic ADC, but ultimately exchange this advantage for greater hardware complexity.

A cascaded phase modulation system for high-speed photonic ADCs is described here, utilizes distributed phase modulation to quantize the signals in the optical domain; thus, the output is in the form of a non-return to zero (NRZ) optical data pattern. This type of optical processing was first discussed by Taylor [1], who used parallel Mach-Zehnder interferometers for this task. The cascaded phase modulation system was implemented at low speeds in a wavelength-division multiplexing scheme to provide wavelength addressable optically quantized data [2]. This cascaded photonic signal processing departs from the current photonic ADC systems by removing the electronic ADC hardware complexity, analog signal channel timing, and synchronization.

The cascaded phase modulation system, as shown in Fig. 1, monitors the change in phase of an optical signal as it passes through multiple electro-optic phase modulators. The figure shows discrete phase modulators, however, a single, long phase modulator could be used in which light is extracted along its length to probe the accumulated optical phase change. This compact monolithic scheme will be shown later, but for now the discrete phase modulators demonstrate the principle of operation with commercially available components.

In this scheme, a cw laser is fed into the cascaded electro-optic phase modulators to produce an optically quantized output from the input microwave signal. The polarization of light into the phase modulators is controlled to send equal amounts of light into the two polarization states of the modulator, and a polarization analyzer is used at the output to convert the phase modulation of the optical signal into amplitude modulation.

This system is similar to Taylor's original system [3]. Contrary to Taylor's system, however, this pipeline scheme accumulates more phase retardation as it travels along a single path; the further the light travels, the larger the phase shift. Then, by exploiting the periodic function of a phase modulator between crossed polarizers, the photonic system provides the analog signal processing necessary to produce a quantized optical output. Fig. 2 shows the optical output for an applied voltage to the electro-optic phase modulator.

The quantization threshold could be set anywhere, but by convention, an optical signal greater than half of full scale is a one, while a signal less than half is a zero. This is shown in Fig. 2 as shaded regions. Nonlinear optical elements such as optically bistable devices [4] can be used to increase the contrast between ones and zeroes.

Errors common to all ADCs occur when the input signal level is near the quantizer's decision point. The magnitude of these errors can be reduced to one least-significant bit error by employing encoding schemes. One such scheme called Gray coding is used to shift each of the

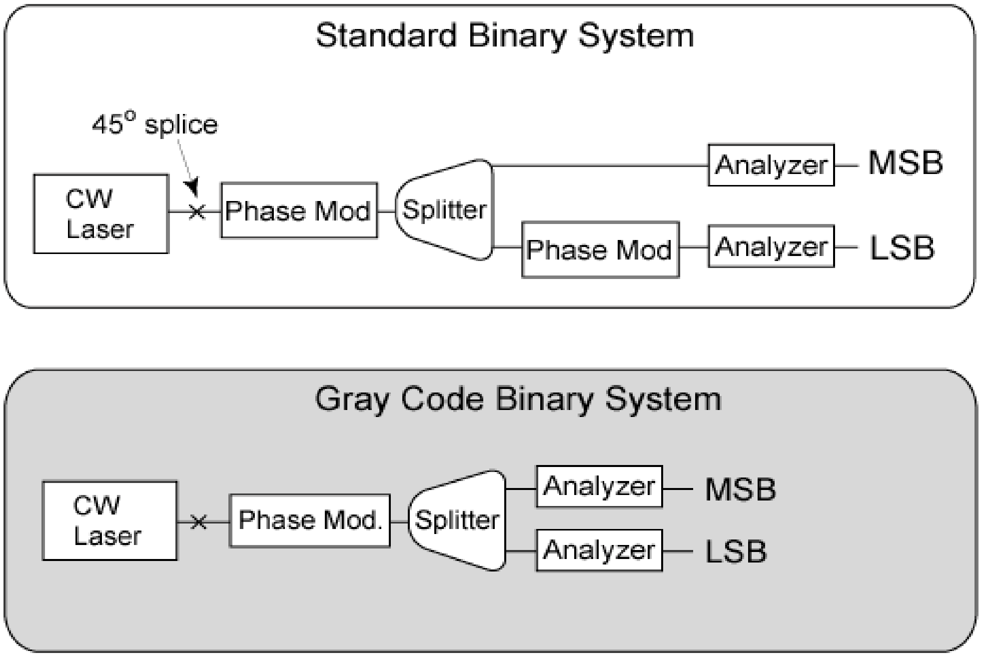

Figure 1—Conceptual drawing of a fiber based 2-bit optical quantizer with a) standard binary outputs, and b) Gray code binary outputs.

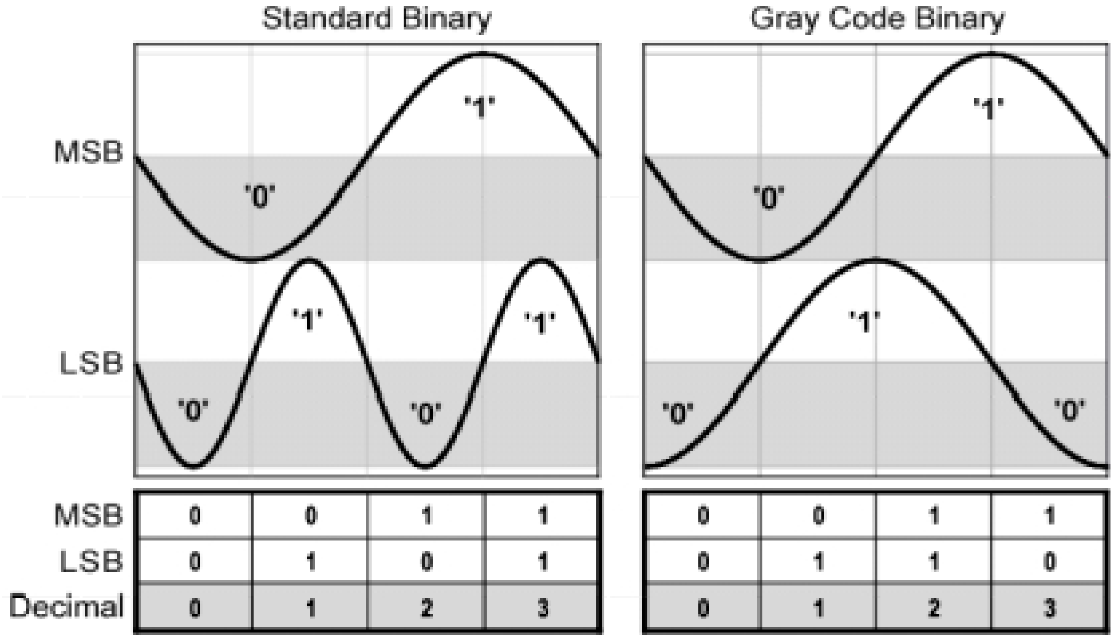

Standard Binary

MSB	0	0	1	1
LSB	0	1	0	1
Decimal	0	1	2	3

Gray Code Binary

MSB	0	0	1	1
LSB	0	1	1	0
Decimal	0	1	2	3

Figure 2—Quantized optical transfer function maps the input signal voltage to digital optical outputs in 2-bit a) standard, and b) Gray code binary systems. Binary values are achieved by thresholding the data at mid-scale.

sinusoidal output functions so that the zero crossings do not overlap [1]. Gray coding is achieved in the optical quantization system shown in Fig. 1 by adding a static phase shift in one of the polarization analyzers. This encoding system also has the benefit of providing two bits of resolution at the output of the first phase modulator, as shown in Fig. 1. The Gray coded output is shown in Fig 2b and, if desired, can be converted back into standard binary using digital signal processing.

The quantized optical output signal is now in the form of a non-return to zero (NRZ) optical data pattern. This data can be left in the optical domain or by using high bit-rate optical telecommunication methods this data can be converted to the electrical domain. In converting the data to the electronic domain, the clocking is performed by the electronic readout system, thereby, relieving any clock or synchronization difficulties between the electrical and optical systems.

I. Experiment

A. 25-GHz, 2-bit Photonic ADC

A two-bit photonic quantization system was implemented as shown in Fig. 3a. The system consists of an Alcatel A1905LMP laser diode operating at 1556 nm and producing 11 mW of optical power followed by a polarization controller and a polarization maintaining fiber (PMF) isolator—to set the polarization state in the PMF system. A PMF 5% tap follows the isolator to provide a diagnostic port. The 95% output of the PMF tap is spliced at a 45 degree angle to a Sumitomo T-PM1.5-20 electro-optic phase modulator with a 3-dB bandwidth of 18.3 GHz and a halfwave voltage (V_π) of ~5.5 V. The output of the modulator is split into two fiber paths for polarization analysis. Each polarization analyzer consisted of a PMF isolator and a polarization controller to adjust the optical bias point of the intensity transfer function. Each of these outputs had an average optical power of 400 μW and was fed into a Tektronix CSA 8000B oscilloscope with an 80C10 65-GHz optical head.

To demonstrate the photonic ADC concept, the phase modulator was driven with a HP 8340B signal source and amplified with a HP 83020A amplifier to drive the modulator to a voltage of $2V_\pi$. The Tektronix oscilloscope was triggered with a HP 8642A signal source that was synchronized with the 10-MHz oscillator of the signal source.

B. 10-GHz, 3-bit Photonic ADC

To increase the resolution of the photonic ADC system, a second phase modulator was added as shown in Fig. 3b following a 10% PMF tap. The former 2-bit polarization analyzer follows the 10% output from the PMF tap and passes through an optical amplifier before the analyzer hardware to provide an average optical power of 500 μW at the detectors. A JDS-Uniphase PM-150-100-1-1-C2L/PDL phase modulator (V_π=9.4 V at 10-GHz) was installed at the 90% output of the PMF tap. A polarization controller and PMF isolator were installed after the JDS modulator to perform the polarization analysis to create the third optical bit of resolution. All of the optical outputs were fed into a Tektronix CSA 8000B oscilloscope with an 80C10 65-GHz optical head.

The phase modulators were driven from a HP 8340B signal source that was split into two microwave signal paths with a HP 11667B microwave power divider. Each microwave signal

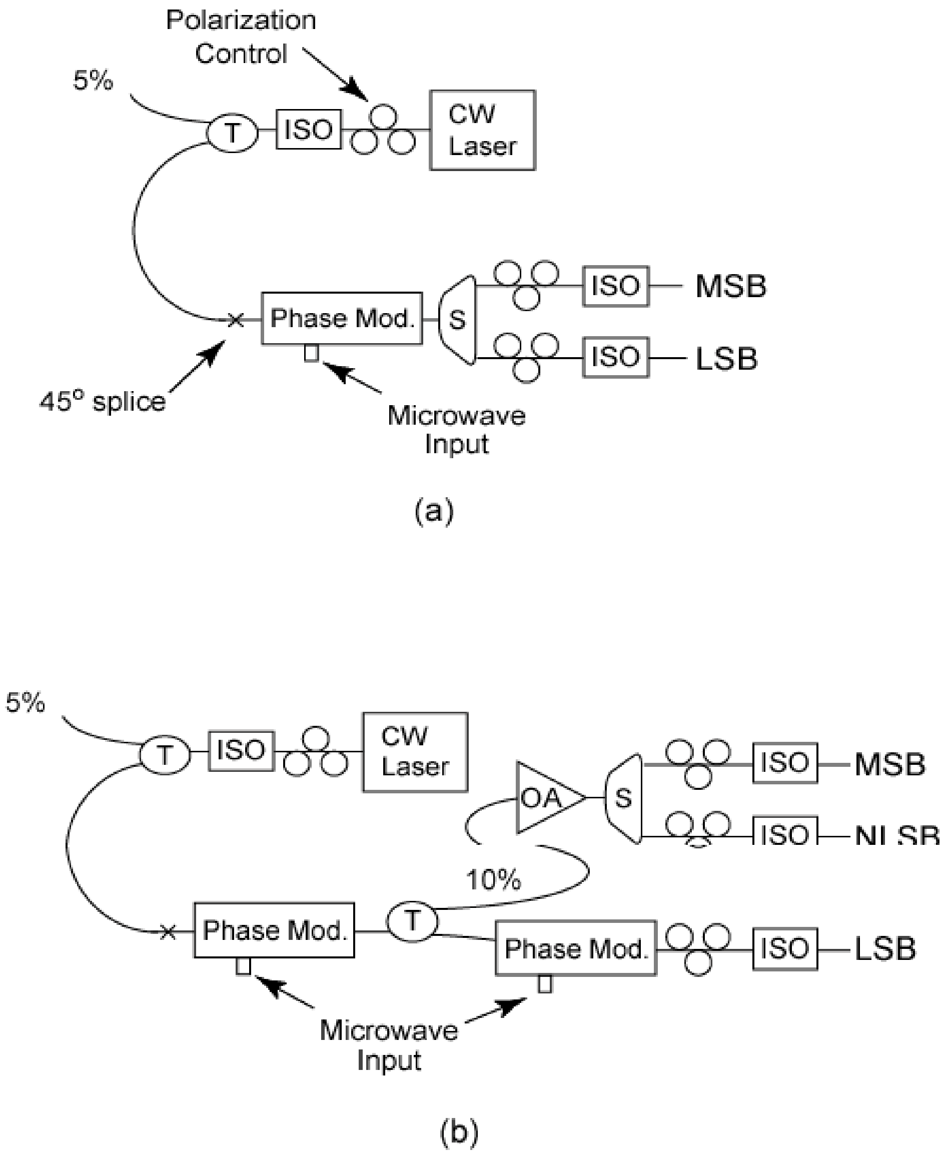

Figure 3—Experimental setup of the photonic ADC for a) 2-bit and b) 3-bit resolution. Iso=Polarization maintaining fiber isolator, T=Polarization maintaining optical tap, OA=optical amplifier, and S=50% optical splitter.

was amplified by a HP 83020A amplifier and supplied the microwave input to the phase modulators. A HP 8642A signal source was used to trigger the Tektronix oscilloscope and was again synchronized with the 10-MHz oscillator of the HP 83020A.

II. Results

A. 25-GHz, 2-bit Photonic ADC

The data in Fig. 4 clearly show the conversion of the input microwave signal at 22-, 24-, and 25-GHz into a quantized optical output. Each figure contains waveforms of the driving signal,

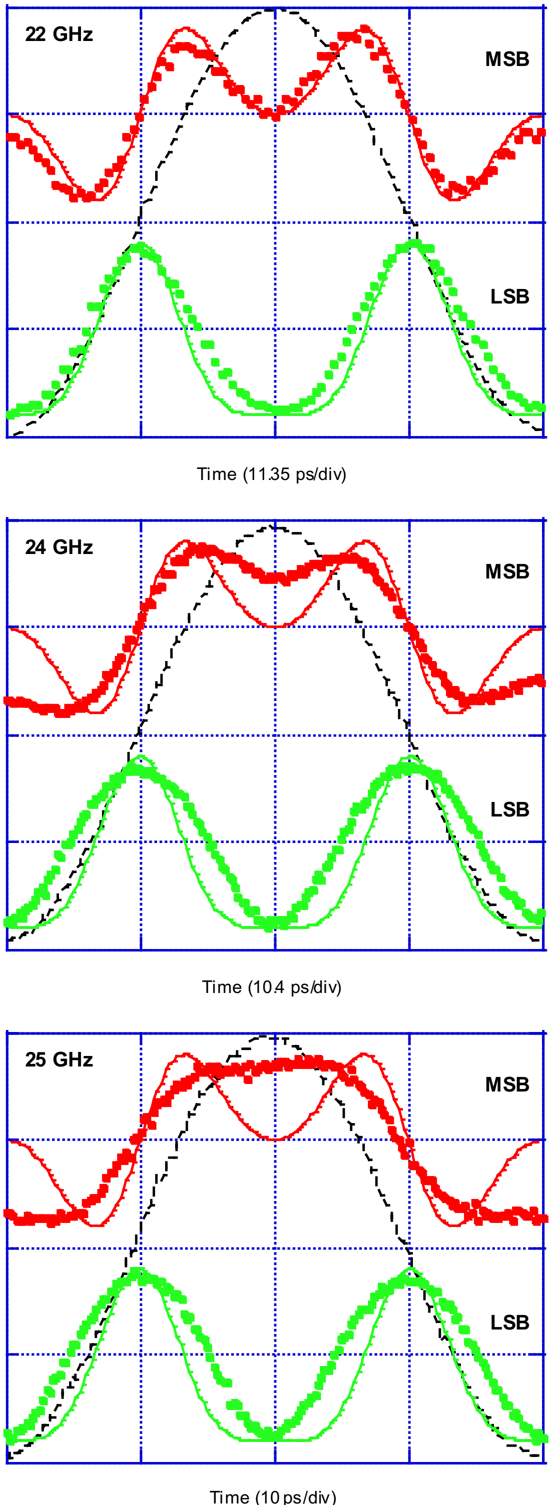

Figure 4—Experimental output from a 2-bit ADC for 22-, 24-, and 25-GHz input microwave signals. The dashed line is the microwave signal driving the phase modulator, the dots are the measured data, and the solid lines are the calculated results.

the least-significant bit (LSB), the most-significant bit (MSB), as well as calculated curves for the LSB and MSB optical output signals.

The two-bit photonic ADC system performs well for input signals as large as 25 GHz. As can be seen from Fig. 4, the bandwidth limitation of the system begins to become apparent at 24 and 25 GHz. At these frequencies the experimental data deviates from the calculated quantization function. The combination of the electro-optic phase modulator and Tektronix oscilloscope are observed to limit the response of the system.

B. 10-GHz, 3-bit Photonic ADC

The 3-bit ADC system driven by a 10-GHz sinusoid is shown in Fig. 5. The figure contains the microwave input signal, optical outputs: LSB, next-LSB (NLSB), and MSB, as well as calculated curves for LSB, NLSB, and MSB. The data closely match the theoretical calculations in response to the 10-GHz input signal.

The largest deviation from the simulation occurs in the least significant bit. It is apparent that the first and third nulls are not completely achieved. This can be attributed to the high-frequency content of the signals. The frequency content of the signals here is >65 GHz and, as such, is beyond the measurement capabilities of the detection system. This will be discussed further in the next section.

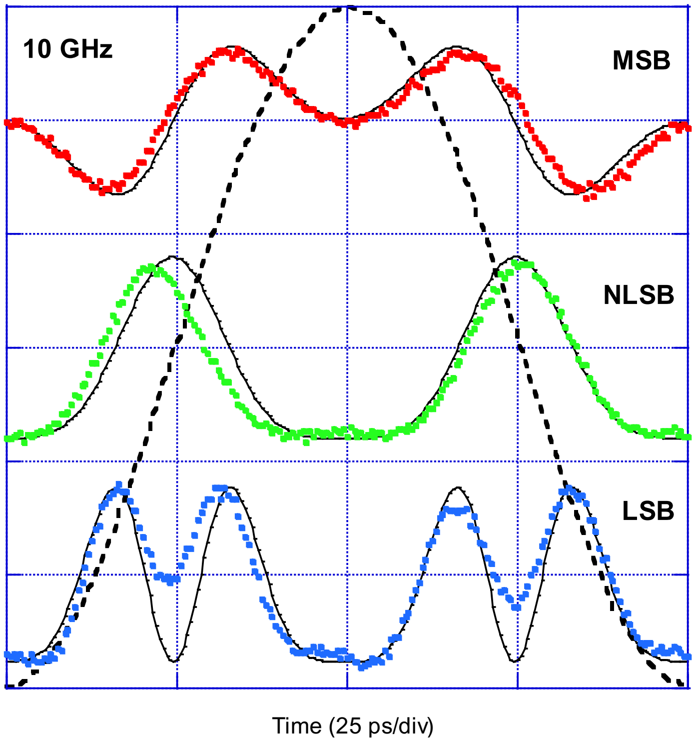

Figure 5—Experimental output from a 3-bit ADC for 10-GHz input microwave signal. The dashed line is the microwave signal driving the phase modulator, the dots are the measured data, and the solid lines are the calculated results.

III. Discussion

A. System speed

The speed of the system is limited by two factors: the electro-optic phase modulator and the readout detection circuit. The electro-optic phase modulator needs to be matched in performance to the microwave signal that is to be measured. For the 3-bit systems, the Sumitomo and JDS electro-optic modulators are sufficient at providing the necessary 10-GHz bandwidth. Upon quantizing the LSB, however, the polarization analyzers turn this 10-GHz signal into a waveform with a 20-dB bandwidth out to 80 GHz. Fig. 6 shows the calculated frequency response of the optical signals (MSB, NLSB, and LSB) for the quantization of a 10-GHz signal. The LSB optical signal still has appreciable power at 60 GHz and is 10-dB lower than this value at 80 GHz. A 65-GHz digital filter applied to the simulated data produces similar responses to those observed in the 10-GHz measured data, thus identifying the Tektronix oscilloscope as the limiting element in the system.

Above 10 GHz, the JDS modulator reaches a limit as the halfwave voltage exceeds our range. The Sumitomo modulator, however, operates to a much higher frequency with reasonable applied voltages such that we can reach 25 GHz, although here the limits of the modulator begin to effect the system as much as the oscilloscope's frequency limit. Due to the nature of the Gray code response, the two-bit resolution photonic ADC correctly quantizes the input signal at 25 GHz even with the band-limiting effects.

To increase the detection speed an optical telecommunications setup can be employed to convert the high-speed data into decimated digital outputs. One such technique utilizes a photonic serial-to-parallel optical time-division demultiplexing architecture to transform a 100-Gb/s optical data stream into eight, 12.5 Gb/s streams [5].

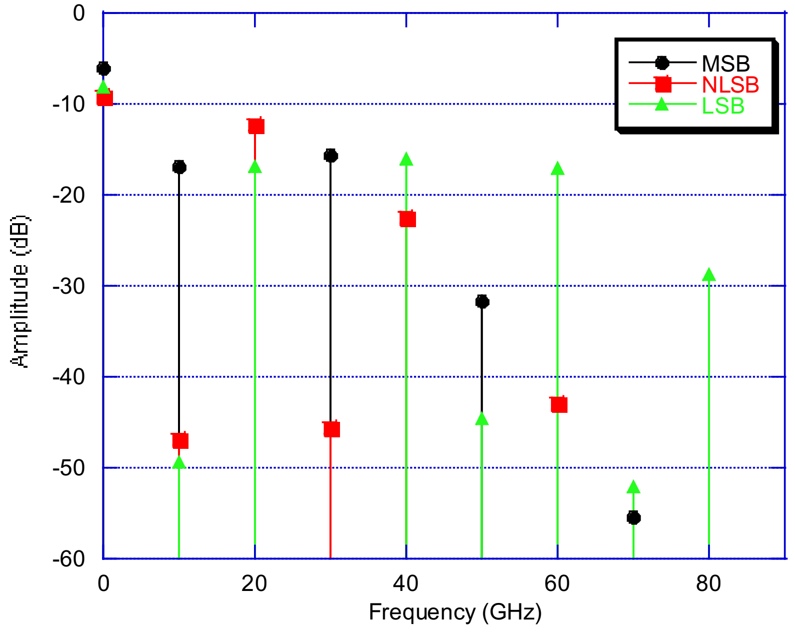

Figure 6—The frequency response of the photonic ADC in response to a 10-GHz microwave input signal.

B. Quantization Error

By its nature, an ideal ADC is limited in resolution to one LSB, i.e. +/-0.5 LSB error when compared to an applied analog ramp voltage. This error represents the difference between the chosen quantized level and the real analog signal. Most ADCs have additional errors (dynamic linearity, gain, offset, and integral linearity) that cause a larger deviation in their quantization [6].

Fig. 7a shows the transfer characteristic and quantization error of the 3-bit ADC in digitizing the 10-GHz input signal. Here we can see a differential linearity error causing a disruption at the third, fourth, and fifth quantization levels. The errors associated with this range from +1.2 LSB to –0.5 LSB. Observing the data in Fig. 5, one can see that these errors arise from the system's bandwidth limitations. These limitations stop the LSB signal from producing deep first and third nulls; this results in quantization errors.

To demonstrate this, the experimental LSB signal is squared in post-processing. This produces deeper nulls while only minimally disturbing the other content of the signal. The results of this operation are shown in Fig. 7b. The quantization error is significantly reduced providing more tolerable quantization errors of +1 LSB to –0.2 LSB. Now, one can observe a static offset error of only ~0.5 LSB. So, by removing the band-limiting effects and correcting the zero-point or static offset error, the quantization error fall within +/-0.6 LSB.

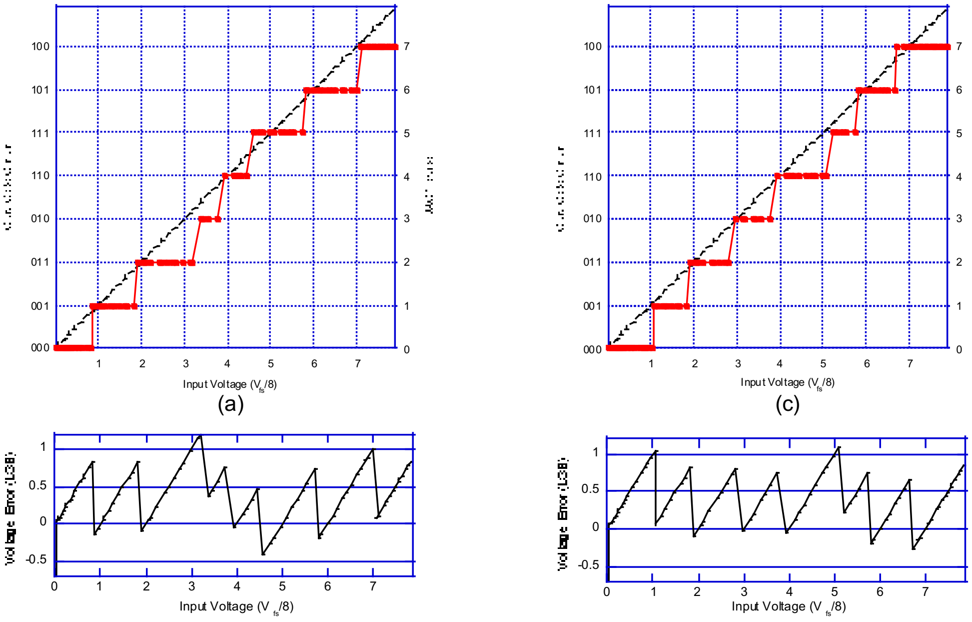

(a) (c)

(b) (d)

Figure 7—(a) The transfer characteristics of the 3-bit photonic ADC. An ideal infinite resolution ADC (dashed line) is subtracted from the experimental results (solid line) producing (b) the quantization error of the ADC. (c) Digital post-processing reduces bandwidth limitations of the LSB producing an improved ADC transfer characteristic: infinite resolution ADC (dashed line), post-processed experimental results (solid line). (d) The post-processing improves the quantization error.

C. Digital Output - Noise and Performance

To characterize the noise performance of this photonic ADC, the Tektronix oscilloscope's optoelectronic receiver is used to examine the ADC's digital optical outputs. The shot noise of the system is calculated by:

$$\sigma_s^2 = 2q(I_p + I_d)\Delta f \quad (1)$$

where q is the charge of an electron, I_p and I_d are the photocurrent and dark current from the detector, and Δf is the effective noise bandwidth of the receiver [7]. For this system the photocurrent dominates the dark current and the noise bandwidth of the receiver is taken as the full 65-GHz bandwidth of the oscilloscope's optical head. Assuming a photodetector responsivity of ~0.4 in (1) yields a shot noise $\sigma_s^2 = 3\times10^{-12} A^2$.

The shot noise should be compared to the system's thermal noise to establish if one noise regime dominates. The thermal noise is calculated using:

$$\sigma_T^2 = (4k_B T / R_L)F_n\Delta f \quad (2)$$

where k_B is Boltzmann's constant, T is the temperature, R_L is the load resistor and F_n is the noise figure of any amplification used in the receiver [7]. Since the noise figure of the Tektronix receiver is unknown, calculating the thermal noise without including the noise figure will provides a lower bound for the thermal noise of $\sigma_T^2 = 2\times10^{-11} A^2$. This shows that the dominant noise source is thermal noise, $(\sigma_T^2 >> \sigma_s^2)$.

In the thermal noise limited regime, the signal to noise ratio (SNR) can be calculated by:

$$SNR = \frac{R_L I_p^2}{4k_B T F_n \Delta f} \quad (3)$$

establishing a 31-dB SNR for the receiver [7]. This neglects the noise figure of the amplifiers in the receiver, and as such needs to be reduced by the actual noise figure of the Tektronix receiver.

In this treatment the noise of the laser has been neglected. This is due to the small intensity noise contribution of the source. With a relative intensity noise (RIN) of the Alcatel laser diode of –150 dB/Hz, over a 100-GHz bandwidth this contributes an intensity noise of –40 dB, or 0.01%, to the signal. The influence of this optical power fluctuation is not a significant source of noise in this system.

D. Monolithic integration

The simple design of this photonic ADC combined with its small number of components makes it a good candidate for monolithic integration. Integrating the phase modulator structures onto a single lithium niobate wafer would allow a cascaded series of electro-optic phase modulators that would increase the resolution of the modulator. Advances in electro-optic modulator technology allow low electrical losses, halfwave voltages approaching a few volts, and low optical/microwave velocity mismatches [8]. New folding modulator structures using 180-degree turns to increase the interaction length of the phase modulators are ideally suited for monolithic integration of this photonic ADC [9].

A schematic diagram of a 4-bit monolithic photonic quantizer is show in Fig. 8. Here four discrete phase modulators have been integrated onto one lithium niobate wafer by bending the optical and electrical waveguides three times. The experimental optical loss at each bend is 0.5 dB and can be fabricated to extract more light if necessary at each bend for the photonic quantizer. The group velocity mismatch has been experimentally characterized for this type of modulator at $\Delta n=0.02$ [8], allowing a 20 mm modulator with only 1.3-ps total delay between microwave and optical signals. The 1.3-ps delay can be reduced further by tailoring the microwave and optical waveguides at the 180-degree bends.

Finally, the monolithic design also improves the optical and microwave power budget by reducing the insertion losses from the discrete components. With the improved electro-optical phase modulator's halfwave voltage and frequency response, this monolithic device could operate at speeds greater than 100 GSPS with 4-bits of resolution.

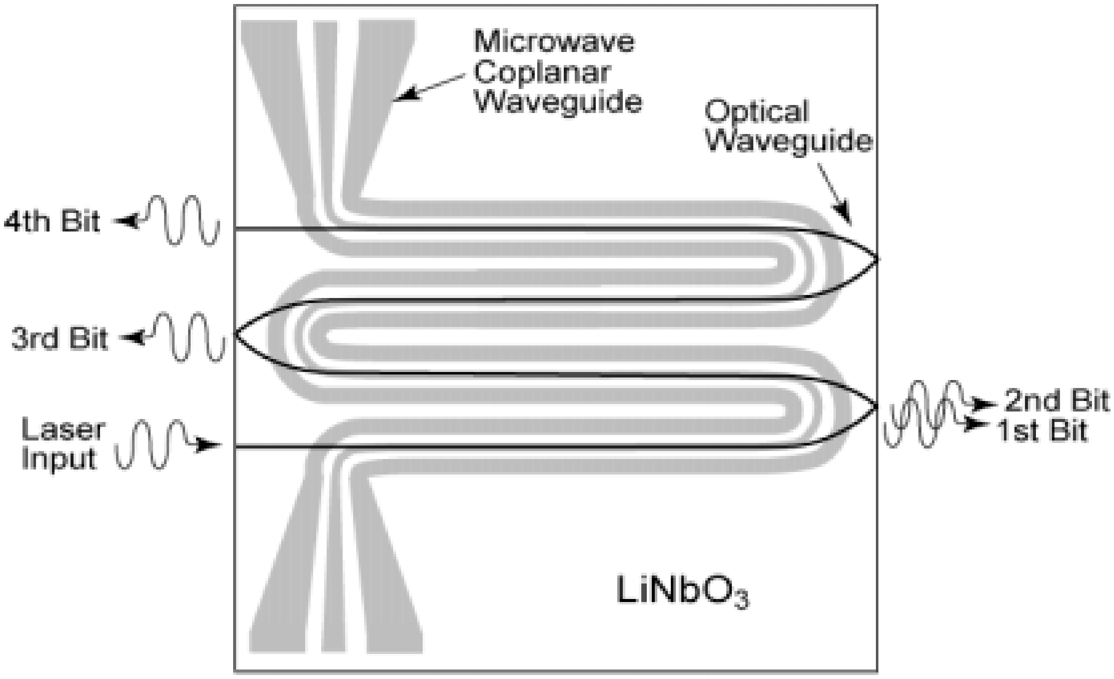

Figure 8—Design of a 4-bit optical quantizer. Monolithic integration of four discrete phase modulators onto one lithium niobate wafer is achieved by bending the optical and electrical waveguides three times.

VI. Conclusion

A high-speed photonic ADC is presented in which a cw laser is fed into the cascaded electro-optic phase modulators to produce an optically quantized output from the input microwave signal. The quantized optical output signal is in the form of a non-return to zero (NRZ) optical data pattern. This data can be left in the optical domain or can be converted to the electrical domain by using high bit-rate optical telecommunication methods.

The system is capable of optically quantizing 25-GHz microwave signals with 2-bit resolution and 10-GHz microwave signals with 3-bits of resolution. The system's speed is limited by two factors: the speed of the optical phase modulator and the measurement bandwidth of the optoelectronic receivers. Utilizing new lithium niobate electro-optic modulator fabrication techniques, a monolithic system is proposed for reaching speeds greater than 100 GSPS with 4-bits of resolution.

REFERENCES

[1] H. F. Taylor, "An optical analog-to-digital converter-design and analysis," *IEEE Journal of Quantum Electronics*, vol. QE-15, pp. 210-16, 1979.

[2] M. Currie, T. R. Clark, and P. J. Matthews, "Photonic analog-to-digital conversion by distributed phase modulation," *IEEE Photonics Technology Letters*, vol. 12, pp. 1689-91, 2000.

[3] H. F. Taylor, "An electrooptic analog-to-digital converter," *Proceedings of the IEEE*, vol. 63, pp. 1524-5, 1975.

[4] D. N. Maywar, G. P. Agrawal, and Y. Nakano, "All-optical hysteresis control by means of cross-phase modulation in semiconductor optical amplifiers," *Journal of the Optical Society of America B-Optical Physics*, vol. 18, pp. 1003-1013, 2001.

[5] M. L. Dennis, W. Kaechele, W. K. Burns, T. F. Carruthers, and I. N. Duling, III, "Photonic serial-parallel conversion of high-speed OTDM data," *IEEE Photonics Technology Letters*, vol. 12, pp. 1561-3, 2000.

[6] M. J. Demler, *High-speed analog-to-digital conversion*. San Diego: Academic Press, 1991.

[7] G. P. Agrawal, *Fiber-Optic Communication Systems*, second ed. New York: John Wiley & Sons, Inc., 1997.

[8] M. M. Howerton, R. P. Moeller, A. S. Greenblatt, and R. Krahenbuhl, "Fully packaged, broad-band LiNbO3 modulator with low drive voltage," *IEEE Photonics Technology Letters*, vol. 12, pp. 792-794, 2000.

[9] M. M. Howerton, R. Krahenbuhl, and R. P. Moeller, "Low loss, compact reflective turns in optical waveguides,"., US Patent Filed June 2002.

X. 100-GSPS TDM ADC via Electro-optic Sagnac interferometery

We have designed and demonstrated a photonic analog-to-digital converter which electro-optically samples high frequency electrical signals and utilizes an electro-optic modulator based time-division demultiplexer [1] allowing parallel electronic digitization at speeds accessible to modern day electronics [2]. The time-division demultiplexing scheme makes use of electro-optic Sagnac interferometer amplitude modulators (SIAMs) [3], which provide highly stable *electronic-bias free* operation. Experiments investigating the performance of all eight demultiplexed channels individually to simulate a photonic ADC are described. Measured digitized signal-to-noise ratios for input signals at −3 dB full-scale powers for each of the 8 channels ranges from 22 dB to 26 dB. Potential system issues and improvements are discussed including a measurement of the demultiplexed channel crosstalk penalty and results indicating a path for resolution improvement of ~4-bits to greater than 5-bits.

Figure 1 illustrates the experimental set up for investigating the 100-GSPS photonic analog-to-digital converter architecture. The 12.5-GHz train of 2.5-ps optical pulses from an actively mode-locked fiber laser [4] is converted to a 100-GHz train by an 8× multiplying polarization maintaining fiber-based multiplexer. The multiplexer consists of three repetition rate doubling stages, each stage constructed with a 3-dB fiber coupler and a delay loop with a fiber stretcher for precise timing. The timing uncertainty of the multiplexed pulses is estimated at <100 fs from autocorrelation measurements. The 100-GHz pulse train is encoded with the signal to be digitized using a $LiNbO_3$ traveling wave Mach-Zehnder amplitude modulator (MZM1: V_π=4.8 V at DC, 3 dB bandwidth=20 GHz, ~2.5 dB/decade rolloff in the 20–50 GHz band). The resolution of the sampling operation is ultimately limited by the noise characteristics of the laser. This laser has previously been shown to have excellent timing and amplitude stability when driven with a low-noise oscillator [5]. The previously measured timing jitter of <10 fs for millisecond measurement times would limit the described photonic sampler to a Nyquist (50 GHz) resolution of ~9-bits (or a SNR of 56 dB), indicating that the sampling operation is not expected to be the limiting factor in a fully-implemented system.

After encoding, the 100 GHz pulse train is divided down to a speed that can be handled by electronic detectors and quantizers using the 1:8 serial-parallel converter shown in Figure 1(b) and described in detail in reference [6]. Each of the electro-optic modulators act as switches to successively divide the modulator input into two output channels at half the input repetition rate. The input clock to the demultiplexer is the same 12.5-GHz master clock driving the laser to ensure a fixed timing relationship between the laser pulses and the switch signals. This binary rate division scheme yields eight 12.5-GHz encoded pulse trains at the output of stage III.

Each of the SIAMs and dual output Mach Zehnder (DOMZ) modulators performs the same function, however the SIAM has a distinct advantage in its operation. The 90° bias phase for the SIAM is accomplished by a highly stable nonreciprocal optical means, which has been shown to be stable with temperature to better than 0.025°/°C. The well-known problem of bias drift in Mach-Zehnder modulators requires the use of electronic bias control circuits and could be difficult to implement for large numbers of modulators in an unattended analog-to-digital conversion system. The outputs of the DOMZs used here were monitored and the biases adjusted for the purpose of ADC demonstration and testing. Ideally, the 1:8 demultiplexer would be constructed with all Sagnac interferometer amplitude modulators. Due to excess loss of the

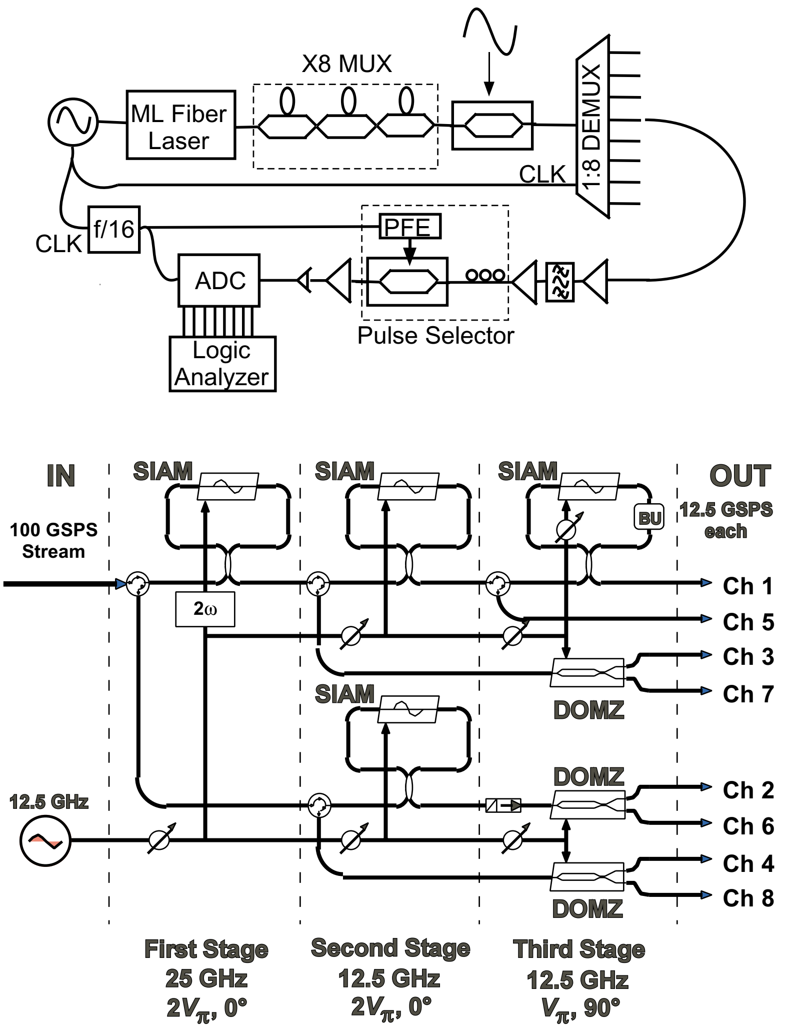

Figure 1—(a) Photonic ADC testing configuration: CLK–master clock 12.5 GHz, X8 MUX–4 3 dB optical couplers and 3 fiber delay lines, Pulse Selector–pulse forming electronics and EO intensity modulator. (b) 1:8 DEMUX (100 GSPS input—8×12.5 GSPS output).

modulators used in this serial-parallel converter (~30 dB/channel), a low-noise ASE filtering optical preamplifier at the channel outputs was necessary prior to detection. This loss could be significantly reduced (by ~10-15 dB) with presently available low-loss modulator technology.

Digitization experiments were performed using an 8-bit electronic ADC (Maxim MAX104) operating at 781 MSPS. The output bit streams of the ADC were read using a logic analyzer with a 1-GHz state analyzer. A pulse selector, consisting of an RF amplifier and step-recovery diode driven by a signal derived from the master clock, and a >25-dB extinction Mach-Zehnder modulator, transmitted every sixteenth pulse. The output of the pulse selector was then boosted with a power regulated optical amplifier to 1 mW and converted to an electrical signal by a photodiode (Discovery DSC50: 8-GHz –3-dB bandwidth, 0.75A/W). Regulating the detector input to 1 mW for all experimental conditions allows the thermal and shot noise limited maximum SNR (for full modulation) to be set at 50 dB for the 10-GHz detector used. As will be seen below, this is much higher than the SNR demonstrated indicating that the detection system noise is not the limiting factor. The ADC was clocked by a sine wave derived from the master clock to ensure the peak of each electrical pulse from the photodiode was digitized.

A 100-GSPS photonic ADC based on the described system would require eight sets of photoreceivers and digitizers operating at a rate of 12.5 GSPS. Photoreceivers faster than 12 GHz are readily available and digitizers that operate at or near this speed with limited resolution currently exist [2]. The known channel order, numbered sequentially in Figure 1(b), would then be used to interleave the digitized data to process the full 50-GHz bandwidth of the 100-GSPS ADC system.

Single-tone testing was performed by applying signals from a microwave synthesizer and a high-power microwave amplifier. The 781-MSPS asynchronous sampling of the high frequency signals results in the aliasing of all signal frequencies to within the Nyquist sampling bandwidth of 390.5 MHz. We performed FFT testing on the digitized signal, determining the signal-to-noise ratio and spur-free dynamic range for each channel. The signal-to-noise ratio is calculated from the digitized data as the ratio of the signal power to the full-bandwidth integrated noise power, including distortion spurs.

The measured signal-to-noise ratio versus input RF power for a 23.5-GHz tone is shown in Figure 2 for each channel. The response of the ADC system is approximately linear up to ~23 dBm (the 1-dB compression point). We note here that quadrature biased modulator distortion can be corrected in a digital system with a time-domain linearization technique [7,8] allowing high modulation depths. The full-scale input range, corresponding to an optical modulation depth of unity, occurs near the maximum of the fitted curves, at 26 dBm. The detected photocurrent at the fundamental frequency for a single-tone input has a $J_1(KV_0)$ dependence, $K \equiv \pi/V_\pi$. This dependence was used in the fits shown in Figure 2 for channels 4 and 2, offering the best and worst performance. The offset between the channel data sets is a measure of their noise power difference. The noise difference from the eight channel average ranges from +1.4 dB for

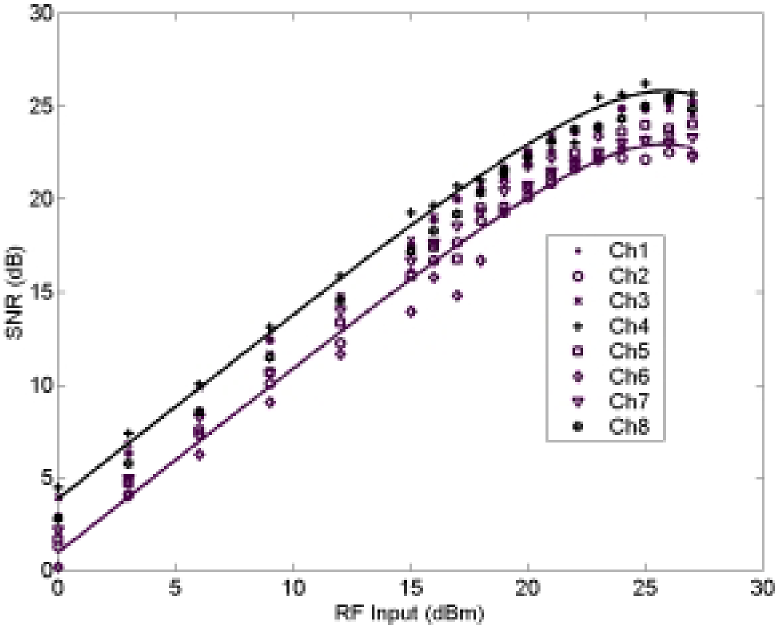

Figure 2—SNR data is shown for an 8-channel system with fit to best and worst channels. Noise difference average ranges from +1.4 dB (Ch4) to −1.5 dB (Ch2).

channel 4 to –1.5 dB for channel 2. This is directly correlated to the channel power out of the demultiplexer, which ranges from 3.1 µW (-25.1 dBm) to 1.4 µW (-28.5 dBm), with the lower power channels having increased noise due to the higher ASE content out of the power boosting optical amplifier of Figure 1a. Near the –3 dB full-scale input, at 23 dBm, the SNR of the eight channels ranges from ~22 dB to ~26 dB or a system resolution of 3.5–4 bits. The spur-free dynamic range at this input power varies from 24 dB to 27 dB for the correctable third harmonic spur [8] and 32 dB to 41 dB for the next limiting non-harmonically related spur. Note that these measurements, due to their single channel nature, ignore some of the issues important for a fully-implemented system such as interleaving errors due to the timing uncertainty between channels (measured to be <100 fs) and receiver uniformity between channels. Both of these errors will introduce spurs and could potentially limit the spur-free dynamic range [9].

To investigate the system's potential performance with a lower loss demultiplexer, we bypassed the multiplexer resulting in an encoded 12.5-GHz pulse incident on the demultiplexer. This allowed a higher energy per pulse output from the demultiplexer, effectively decreasing the ASE noise level from the optical amplifiers, for the same average power input to the first modulator (to avoid damage.) The results of this experiment versus input power are shown in Figure 3 for channel 3. Also shown on the plot is the SNR plot for the full 100 GSPS demultiplexed to 12.5 GSPS of Figure 2 for channel 3. A comparison of the multiplexed curve, where all eight channels have signal, and the bypassed curve, where all DEMUX input is directed to the single channel of interest, with the same optical power demonstrates inter-channel crosstalk penalty of 1.4 dB due to leakage in the demultiplexer. Leakage would present an even greater problem in a time-division demultiplexing scheme requiring active control of electrical

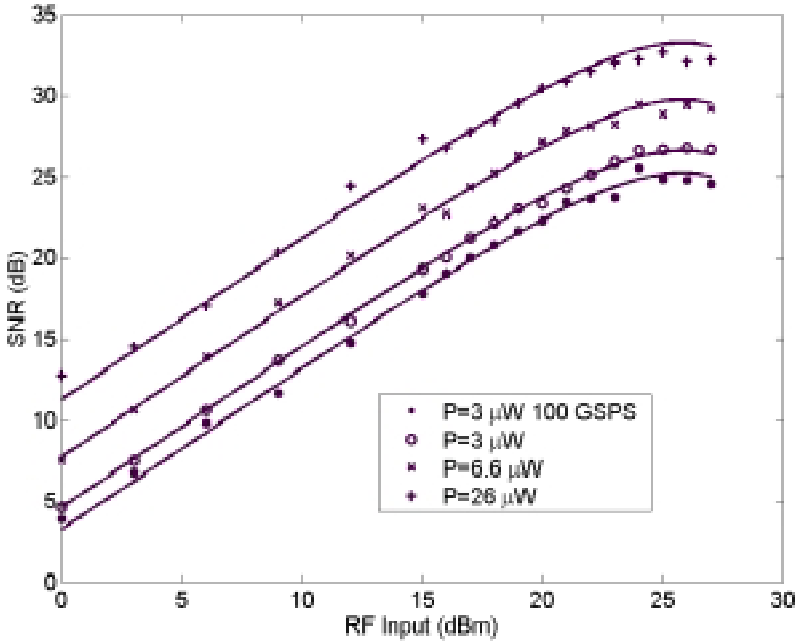

Figure 3—Single channel SNR data with fit to each set of data for changing optical power out of demultiplexer. Note that the detector input power was regulated to 1 mW. Increase in received optical power by 9 dB results in SNR increase to 32 dB at the –3 dB full scale input. Note the crosstalk penalty (difference between two 3.1µW curves) of 1.4 dB noise power.

bias, where bias drift will introduce significant channel-to-channel crosstalk, due to insufficient nulls in the DEMUX transmission function at the time slots of the other eight channels. A fully bias-free system based on Sagnac interferometers would avoid this problem. Figure 3 shows that an increase to a power of 26 μW (-15.9 dBm), or a 9 dB decrease in the excess insertion loss through the demultiplexer, would allow an increase in SNR to 32 dB (~5 bits) at the –3 dB full scale input. It should be noted that 5 bits is not a fundamental limit and is a result of experimental factors including photodetector signal to digitizer dynamic range matching and excess amplitude noise on the laser.

We have designed a 100-GSPS photonic analog-to-digital converter. The measured individual channel signal-to-noise ratios was 4 effective bits, with better than 5 effective bits of resolution demonstrated for a lower loss system. The technique makes use of a 1:8 serial-parallel converter with electronic-bias free electro-optic Sagnac interferometers.

REFERENCES

[1] M.L. Dennis, W.K. Burns, T.F. Carruthers, and I.N. Duling., "Eight-to-one demultiplexing of 100-Gbit/s TDM data using LiNbO3 Sagnac interferometer modulators", in Optical Fiber Communications Conference, OSA Technical Digest Series, Vol. 2, 1998, pp. 110-112.

[2] R. H. Walden, "Analog-to-digital converter survey and analysis", IEEE J. Selected Areas in Comm., 1999, pp. 539-550.

[3] M.L. Dennis, I.N. Duling and W.K. Burns, "Inherently bias drift free amplitude modulator", Electron. Lett., vol. 32, pp. 547–548 (1996).

[4] T. F. Carruthers and I. N. Duling III, "10-GHz, 1.3-ps Erbium Fiber Laser Employing Soliton Pulse Shortening," Opt. Lett., 1996, vol. 21, pp. 1927-1929.

[5] T. R. Clark, T. F. Carruthers, P. J. Matthews and I. N. Duling III, "Phase Noise Measurements of an Ultrastable 10-GHz Harmonically Mode-Locked Fiber Laser," Electron. Lett., vol. 35, 1999, pp. 720-721.

[6] M. L. Dennis, W. Kaechele, W. K. Burns, T. F. Carruthers, and I. N. Duling, III, "Photonic serial-parallel conversion of high-speed OTDM data," *IEEE Photonics Technology Letters*, vol. 12, pp. 1561-3, 2000.

[7] J. C. Twitchell, "Photonic A/D Converters," in *Conference on Lasers and Electrooptics Technical Digest*, Optical Society of America, Washington, DC, 1999, paper CtuN1.

[8] T. R. Clark, M. Currie, and P. J. Matthews, "Digitally linearized wide-band photonic link," *Journal of Lightwave Technology*, vol. 19, pp. 172-9, 2001.

[9] A. Petraglia and S. K. Mitra, "Analysis of mismatch effects among A/D converters in a time-interleaved waveform digitizer," IEEE Trans. on Instrumentation and Measurement, vol. 40, 1991, pp. 831.